FEDERAL UNIVERSITY OF SÃO CARLOS

Center for Exact Sciences and Technology

Graduate Program in Chemical Engineering

Rauber Daniel Pereira

FINE BUBBLES GENERATED BY A NEW PULSED GAS FLOW RATE SYSTEM AND THEIR ROLE IN MASS TRANSFER PROCESSES

SÃO CARLOS - SP

2023

UNIVERSIDADE FEDERAL DE SÃO CARLOS

Centro de Ciências Exatas e de Tecnologia

Programa de Pós-graduação em Engenharia Química

BOLHAS FINAS GERADAS POR NOVO SISTEMA DE VAZÃO PULSADA DE GÁS E O SEU PAPEL EM PROCESSOS DE TRANSFERÊNCIA DE MASSA

Rauber Daniel Pereira

Tese de Doutorado apresentada ao Programa de Pós-Graduação em Engenharia Química como parte dos requisitos necessários para a obtenção do título de Doutor em Engenharia Química, área de concentração em Pesquisa e Desenvolvimento de Processos Químicos

Orientador: Dr. Alberto Colli Badino Junior
Coorientador: Dr. Antonio José Gonçalves da Cruz

SÃO CARLOS - SP

2023

FEDERAL UNIVERSITY OF SÃO CARLOS

Center for Exact Sciences and Technology

Graduate Program in Chemical Engineering

FINE BUBBLES GENERATED BY A NEW PULSED GAS FLOW RATE SYSTEM AND THEIR ROLE IN MASS TRANSFER PROCESSES

Rauber Daniel Pereira

Thesis presented as part requirements to obtain PhD degree in Chemical Engineering, concentration area: Research and Development of Chemical Processes.

Supervisor: Dr. Alberto Colli Badino Junior

Co-supervisor: Dr. Antonio José Gonçalves da Cruz

SÃO CARLOS - SP

2023

UNIVERSIDADE FEDERAL DE SÃO CARLOS

Centro de Ciências Exatas e de Tecnologia
Programa de Pós-Graduação em Engenharia Química

Folha de Aprovação

Defesa de Tese de Doutorado do candidato Rauber Daniel Pereira, realizada em 28/08/2023.

Comissão Julgadora:

Prof. Dr. Alberto Colli Badino Junior (UFSCar)

Prof. Dr. Mateus Nordi Esperança (IFSP)

Prof. Dr. Gilson Campani Júnior (UFLA)

Prof. Dr. Kaio César da Silva Rodrigues (UFOB)

Prof. Dr. Rodrigo Béttega (UFSCar)

O Relatório de Defesa assinado pelos membros da Comissão Julgadora encontra-se arquivado junto ao Programa de Pós-Graduação em Engenharia Química.

"Ad majorem Dei gloriam."

Ignatius of Loyola

APOIO FINANCEIRO

O presente trabalho foi financiado pela Fundação de Amparo à Pesquisa do Estado de São Paulo (FAPESP), processos: n. 2018/24460-4 (Bolsa de Doutorado no País) e n. 2021/06659-0 (BEPE).

O presente trabalho foi realizado com apoio da Coordenação de Aperfeiçoamento de Pessoal de Nível Superior – Brasil (CAPES) – Códigos de Financiamento: 309728/2021-5 e 305919/2021-0.

AGRADECIMENTOS

Em primeiro a Deus pela vida que me deu, pelos caminhos que me faz percorrer e pela constante intercessão de Nossa Senhora.

Aos meus pais, por terem me dado muito mais do que receberam. Pelo amor e apoio constantes, mas principalmente pelo caráter e pela criação que me deram.

À minha noiva e companheira Marina. Pelo seu amor, apoio e confiança. Por escolher permanecer e trilhar esse caminho comigo.

Ao professor Alberto Colli Badino pela orientação, paciência, aconselhamentos e confiança que foram constantes desde o primeiro dia de trabalho. Muito mais que um orientador, Prof. Alberto se tornou um grande amigo e exemplo de profissional e de pessoa que levarei por todos os meus dias.

Ao professor Antonio José Gonçalves da Cruz, por ter acreditado em mim e apoiado prontamente meu retorno à universidade. Professor Antonio se tornou um grande amigo e mentor.

Ao professor Adel M. Al-Taweel, por ter aceitado me receber na Dalhousie University e por ter me dado todo o suporte para que eu pudesse realizar o projeto e conhecer uma das realidades mais enriquecedoras que eu poderia ter.

Aos colegas e amigos do Departamento de Engenharia Química, pela amizade e apoio, pelos cafés e bons momentos que compartilhamos, em especial aqueles do laboratório do professor Alberto: Letícia, Kaio, Ivan, Mariane, Mateus, Éric, Emanoela.

À Universidade Federal de São Carlos e ao Programa de Pós-Graduação em Engenharia Química pela oportunidade e estrutura para realização do trabalho.

RESUMO

A utilização de bolhas de tamanho reduzido (bolhas finas ou microbolhas) em operações de transferência de massa tem sido amplamente discutida, e diversos métodos de geração dessas bolhas têm sido desenvolvidos e aplicados. Porém, métodos que envolvam a geração de bolhas de tamanho reduzido em escala piloto ou industrial continuam inexplorados, bem como o papel que essas bolhas desempenham nas operações de transferência de massa. Esse trabalho teve por objetivo desenvolver um novo sistema de geração de bolhas finas (*Fine Bubble Generator*, "FBG") em reator tipo coluna de bolhas. Esse sistema é composto por válvula solenoide operada em alta frequência (>70 Hz) para geração de vazão pulsada de gás e por aspersores usinados com furações convencionais, ou seja, furações que podem ser realizadas de maneira comercial (diâmetros de orifícios acima de 0,3 mm). O sistema foi desenvolvido e caracterizado em reator tipo coluna de bolhas em escala piloto (173 L), a partir da determinação dos diâmetros das bolhas geradas sob diferentes condições operacionais de vazão de gás, frequência operacional e composição do meio líquido. Observou-se uma região ótima de operação na faixa de 100 a 150 Hz em meios não-coalescentes, na qual reduções de diâmetro de bolha na ordem de 33% em relação à aeração convencional foram alcançados. O sistema foi então empregado em reator tipo coluna de bolhas de 10,0 L para avaliação do coeficiente volumétrico de transferência de oxigênio ($k_L a$) em meio líquido coalescente e não-coalescente. Utilizou-se nessas operações aspersores com furações convencionais (R8H) e do tipo sinterizado (SSD), o qual naturalmente gera microbolhas ($d_b <$ 1000 μm). O sistema de vazão pulsada em conjunto com o aspersor R8H gerou aumentos no valor de $k_L a$ da ordem de 50 e 80% em comparação com a operação de aeração convencional (vazão contínua), para os meios não-coalescente e coalescente, respectivamente. Já para o aspersor SSD não foi observada alteração significativa no $k_L a$, o que corrobora a hipótese de haver uma frequência natural mínima de formação das bolhas a ser superada para que ocorra o seu desprendimento prematuro. Por fim, o sistema FBG foi aplicado na operação de esgotamento (*stripping)* de etanol, em reatores tipo coluna de bolhas de 10,0 (aspersores R8H e SSD) e 50,0 L (aspersor PS3 – furações convencionais de 0,3 mm, em maior quantidade para reator de 50,0 L). Nesse ponto do trabalho foi possível comprovar a saturação das bolhas em diversas condições operacionais de vazão e diâmetro de bolha, e desenvolver uma modelagem matemática que quantificou a parcela de etanol removida por arraste termodinâmico (ou vaporização) e mecânico. Esse último mostrou-se como sendo capaz de enriquecer a fase gasosa em etanol em valores acima da seletividade promovida equilíbrio termodinâmico, chegando a alcançar 15 vezes a concentração da fase líquida. Esse fato evidencia a complexidade do arraste mecânico, que depende do diâmetro das bolhas, nas operações de remoção de solventes voláteis e demonstra que, sob as corretas condições operacionais, esse fenômeno pode favorecer a eficiência do processo de *stripping*. A última etapa do estudo consistiu na aplicação do sistema FBG na fermentação alcoólica extrativa em reatores de 10,0 e 50,0L, nas quais foi possível alcançar um aumento de produtividade na ordem de 15% em relação à fermentação batelada convencional utilizando uma vazão específica de CO_2 de 0,4 vvm.

Palvras-chave: Processos de transferência de massa, transferência de oxigênio, arraste gasoso, geração de bolhas finas, arraste por vaporização, arraste mecânico.

ABSTRACT

The use of small-sized bubbles, known as fine bubbles or microbubbles, in mass transfer operations has been extensively discussed, and various bubble generation methods have been developed and applied. However, methods involving the generation of small-sized bubbles at pilot or industrial scale remain unexplored, as well as the role these bubbles play in mass transfer operations. This study aimed to develop a new system for generating fine bubbles, referred to as the Fine Bubble Generator (FBG), within a bubble column reactor. This system comprises a high-frequency (>70 Hz) solenoid valve for generating pulsed gas flow and machined spargers with conventional perforations, i.e., perforations that can be commercially produced (orifices diameters above 0.3 mm). The system was developed and characterized in a pilot-scale bubble column reactor (173 L) by determining the bubble diameters generated under different operational conditions of gas flow, operational frequency, and liquid medium composition. An optimal operating region was observed in the range of 100 to 150 Hz in non-coalescent media, where reductions in bubble diameter of around 33% compared to conventional aeration were achieved. Subsequently, the system was applied to a 10.0 L bubble column reactor to evaluate the volumetric oxygen transfer coefficient ($k_L a$) in coalescent and non-coalescent liquid media. In those operations, spargers with conventional perforations (R8H) and sintered-type spargers (SSD), which naturally generate microbubbles (d_b < 1000 μm), were used. The pulsed flow system combined with the R8H sparger led to increases in $k_L a$ values of approximately 50% and 80% compared to conventional aeration (continuous flow), for non-coalescent and coalescent media, respectively. However, for the SSD sparger, no significant change in $k_L a$ was observed, supporting the hypothesis of a minimum natural frequency of bubble formation that needs to be surpassed for premature detachment to occur. Furthermore, the FBG system was employed in ethanol stripping operations within 10.0 L bubble column reactors (using both R8H and SSD spargers) and a 50.0 L bubble column reactor (using a PS3 sparger - conventional perforations of 0.3 mm, scaled in number of orifices for a 50.0 L volume). At this stage of the study, bubble saturation was confirmed under various operational conditions of gas flow rate and bubble diameter. A mathematical model was developed to quantify the fraction of ethanol removed through thermodynamic-driven entrainment (or vaporization) and mechanical entrainment. The latter was found to enrich the gas phase with ethanol concentrations surpassing those achieved through thermodynamic equilibrium selectivity, reaching up to 15 times the liquid phase concentration. This demonstrates the complexity of mechanical entrainment, which depends on bubble diameter, in operations involving the removal of volatile solvents. It also illustrates that, under the right operational conditions, this phenomenon can enhance the efficiency of the stripping process. The final phase of the study involved applying the FBG system to extractive alcoholic fermentation in 10.0 L and 50.0 L bubble column reactors, achieving a productivity increase of around 15% compared to conventional batch fermentation using a specific CO_2 flow rate of 0.4 vvm.

Keywords: Mass transfer processes, oxygen transfer, gas stripping, fine bubble generation, vaporization entrainment, mechanical entrainment.

LIST OF FIGURES

LIST OF TABLES

SUMMARY

Chapter 1

Introduction and Literature Review

1.1 Introduction

The recovery of volatile compounds from fermentation broths has been extensively investigated, particularly for processes yielding high-value products. Within the Brazilian bioethanol industry, the utilization of the stripping process to recover ethanol from fermentation broths presents numerous advantages (Almeida et al., 2021). In chemical operations, stripping is a separation process used to remove volatile components (gases or vapors) from a liquid mixture. It typically involves passing a gas, such as steam or an inert gas, through the liquid, causing the volatile compounds to evaporate out of the liquid phase and be carried away by the gas stream. Beyond the mere retrieval of ethanol, the stripping process plays a pivotal role in alleviating the inhibitory effects exerted by ethanol on the yeast responsible for fermentation (Sonego et al., 2014b). This inhibition challenge stands as a significant hurdle in the Brazilian bioethanol sector. The yeast experiences inhibition due to the accumulating ethanol levels during fermentation, thereby diminishing the productivity of the industrial operation. Consequently, the stripping process not only facilitates ethanol recovery but also mitigates the inhibitory by-product's impact and reduces the broth temperature through the vaporization of ethanol and water. The issues of ethanol inhibition and temperature control have remained substantial challenges in the context of ethanol production in Brazil (Almeida et al., 2021).

Sonego et al. (2014, 2016) conducted a comprehensive study encompassing both modeling and experimental assessment of ethanol production through the application of stripping with CO_2. The authors determined an optimal specific flow rate of 2.5 vvm for bioreactor operation, resulting in an ethanol production increase of approximately 33.0% compared to conventional processes. While CO_2 generated by yeasts served as the stripping gas for ethanol fermentation, the cooling effects induced by the stripping process yielded a favorable energy balance for the fermentation unit. Beyond its applicability to sugarcane-derived ethanol, stripping has also proven effective in the production of ethanol at elevated temperatures by thermophilic bacteria, as evidenced by Calverley et al. (2020). In preliminary trials using hydroalcoholic solutions, the authors achieved ethanol recovery values exceeding those predicted by thermodynamic equilibrium, a finding congruent with Abdulrazzaq et al. (2016), who utilized microbubbles. In a similar vein, inert gas was harnessed by Ezeji et al. (2005) to recover butanol from a fermentation broth. Notably, the authors observed that the gas phase reached the saturation concentration of butanol during the experimental runs.

Thus, having underscored the significance of stripping processes in industrial operations, the primary objective shifts towards rendering these processes operationally and economically viable. As highlighted by Sonego et al. (2014, 2016), the specific flow rate of 2.5 vvm is feasible at the bench scale but not at an industrial scale. In a parallel to oxygen transfer, a movement to explore methods and equipment that generate smaller bubbles compared to conventional ones has captured the attention of numerous researchers (Desai et al., 2021; J. Hanotu et al., 2016b; Song et al., 2021; Zimmerman et al., 2008a). The augmentation of interfacial area for mass transfer between phases, facilitated by smaller yet more numerous bubbles, has already demonstrated effectiveness in gas transfer to the liquid phase (Tesař, 2017). Therefore, it appears natural that the logical progression towards the development of sustainable and efficient procedures for the removal of volatile compounds from fermentation media would involve the establishment of methods for generating fine and microbubbles. Theoretically, this advancement would enhance the efficiency of well-established processes.

Various methods for generating small-sized bubbles have been proposed in the literature (Tesař et al., 2006; Zimmerman et al., 2008), with gas pulsation feeding for premature bubble detachment being one of the most efficient (Zimmerman et al., 2009). Zimmerman et al. (2008) developed a fluidic oscillator capable of producing gas pulses that, when supplied to a sparger, lead to the early release of small-sized bubbles. While effective, research groups have primarily focused on generating microbubbles, which have diameters (d_b) smaller than 100 μm (according to the ISO 20480). To achieve this, they employ pulsed gas flow and also sintered spargers, which on their own generate fine bubbles (d_b < 3.00 mm) or even microbubbles under conventional gas feeding conditions. Furthermore, most experiments are conducted at the bench scale (Calverley et al., 2020b; Song et al., 2021), using reactors with limited volume capacity. In addition to not being applicable at the pilot and industrial scale due to various drawbacks such as clogging of sparger pores, maintenance and construction difficulties of spargers, and limited versatility for changing operational conditions (Tesař et al., 2006), the studies conducted so far have not thoroughly addressed the role that bubbles of different diameters play in the removal of volatile components, particularly in terms of vaporization (thermodynamic entrainment) and mechanical entrainment caused by the momentum carried by the bubbles.

The objective of this study is to develop a novel system for generating fine bubbles, composed of the following components: a high-frequency solenoid valve-based pulsed gas flow

generator and a sparger built with conventional perforations (non-sintered material). The combination of a pulsed gas flow generator and a conventional sparger has not been utilized in any previously reported literature. This system aims to be suitable for pilot and industrial scale applications, generating bubbles of reduced size that align with the operational scales they are intended for. After developing and characterizing the system, the main focus of the study was to apply different bubble diameters in the stripping process. This application was initially conducted under controlled operating conditions to assess the level of bubble saturation, with the only entrainment phenomenon being vaporization. Subsequently, stripping experiments were carried out at various gas flow rates, closer to industrial conditions, and a modeling approach was introduced to isolate and quantify the removal of ethanol and water in terms of molar quantities, for both thermodynamic and mechanical entrainment. This study sheds light on the two involved phenomena and paves the way for the development of new and improved strategies for volatile component removal.

1.2 Literature Review

1.2.1 Role of Bubbles in Mass Transfer Process

The increasing demand for energy, resources, manufactured products, and chemicals has led the industry worldwide between a rock and a hard place. The high demand for production faces on the other side the pressure for more sustainable industrial operations. Regarding the chemical process industry, reaction and separation engineering can play a crucial role in the development of more sustainable biochemical processes (Adel M Al Taweel, 2019). Although there is room for improvement in many industrial operations, the ones regarding mass transport between phases stand out. The use of small-sized bubbles can increase drastically the efficiency of the mass transfer between phases due to the higher contact surface area between the gas and liquid phases and the longer residence time of these small bubbles in the bioreactor (Parmar and Majumder, 2013). Two major unit operations involving mass transfer phenomena can be cited, as follows:

- Bioreactor aeration, which is responsible for the oxygen supply to the microorganisms to generate industrial inputs for medicines, vaccines, food, and biofuels (Seidel et al., 2020), and also for wastewater treatment (Herrmann-Heber et al., 2019);

- Stripping processes, which have been an alternative to remove/separate valuable volatile compounds from a liquid broth by passing gas through it (Abdulrazzaq, et al., 2016; Sonego et al., 2016; Sonego et al., 2014).

The transfer of oxygen from the gas phase to the liquid phase is crucial in bioprocesses involving microorganisms with high respiration rates. Similarly, gas-liquid transfer of carbon dioxide in carbonation processes for the production of various carbonates and bicarbonates is essential. Operations such as liquid medium sterilization using ozone also seek to enhance gas-liquid transfer efficiency to reduce the consumption of ozone gas. Additionally, the extraction of volatile compounds from fermentation media by passing a gas phase through the liquid medium aims to mitigate microbial inhibition caused by the toxicity of these components generated during the process, such as methanol, ethanol, and butanol (Calverley et al., 2020, 2021). Beyond chemical and biochemical reactions, flotation operations also benefit from the use of fine bubbles, which enhances the separation efficiency of fine solid particles from liquid media, as demonstrated in various literature studies. These factors have driven research efforts toward the development of techniques and systems capable of reducing the diameter of bubbles generated in reactors, bioreactors, and separation equipment.

For both aeration and stripping processes whose efficiencies are strongly dependent on mean bubble diameter, there is a significant advantage of using fine (bubble diameter between 1 and 3.0 mm) and microbubbles (diameter less than 1.0 mm) in the process instead of using large bubbles. Particularly considering the presence of electrolytes, which represents most the industrial wastewater, the values of the convective mass transfer coefficient (k_L) and the interfacial area of bubbles (a) are important to establish strategies of scaling-up and to increase the efficiency of gas-liquid operations (Al Taweel et al., 2013).

1.2.2 Generation of Fine and Microbubbles

Various mechanisms for generating microbubbles have been developed to date (Terasaka et al., 2011) based on three main techniques: compression, ultrasound, and intermittent gas flow (W. Zimmerman et al., 2008).The first method involves compressing the gas-liquid system followed by rapid decompression, leading to the nucleation of small bubbles at the point of solution supersaturation. Microbubble generation by ultrasound involves exposing the gas-liquid system to intense ultrasound, which fragments the bubbles present in the biphasic solution. However, this

method is not suitable for bioreactors as the ultrasound source can damage microbial cell walls. Both of these approaches suffer from high power consumption, rapid bubble coalescence, and reliance on equipment with relatively high installation and maintenance costs.

However, a third mechanism to generate smaller bubbles has stood out, which is based on the pulsed injection of gas through the sparger located at the base of the reactor, limiting bubble growth by the volume of gas injected with each pulse. Tesař et al. (2006) and Zimmerman et al. (2008) developed a pulsed gas injection mechanism called a fluidic oscillator, which appears to be the most promising technology reported so far for microbubble generation. This is due to its simple installation, equipment robustness, lack of need for liquid recirculation, as well as its low construction, operation, and maintenance costs. Essentially, a fluidic oscillator is a gas or liquid-fed structure with inlet and outlet ducts, devoid of moving parts, and feedback ducts (Ghanami and Farhadi 2019; Tesař et al. 2006). Tesař et al. (2006) proposed the use of a fluidic oscillator for microbubble generation. As mentioned, the device lacks moving parts and features two alternating gas outlets controlled by oscillation frequency. The frequency control is achieved by the length of the tube used to connect the terminals related to the gas outlet ducts, a phenomenon made possible by the so-called Coandă effect (Panitz and Wasan, 1972) as shown in Fig. 1.1.

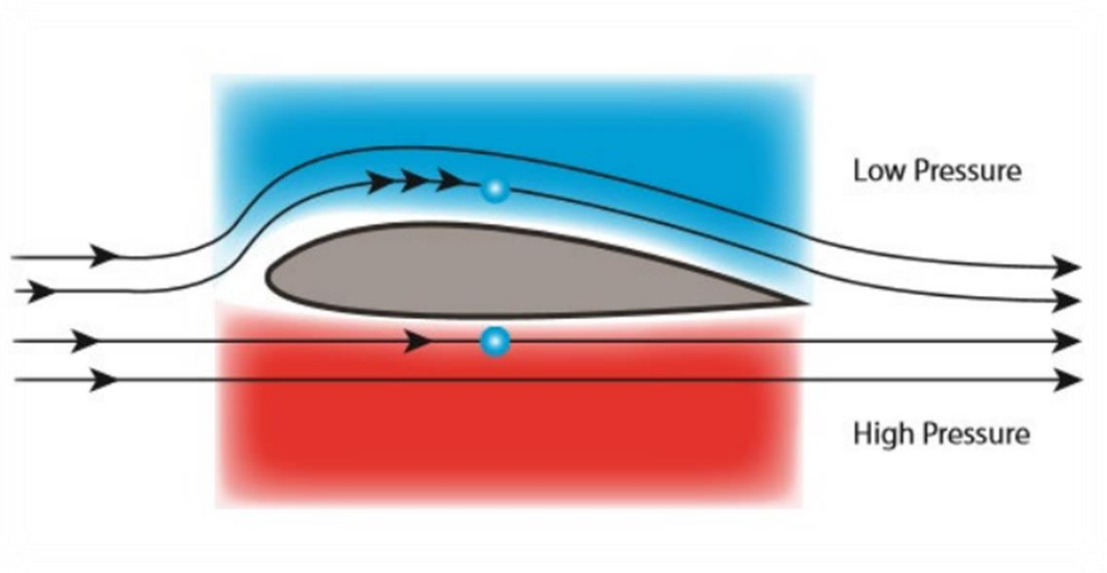

Figure 1.1. Illustration of the Coandă Effect. National Museum of the United States Air Force, nationalmuseum.af.mil

The Coandă effect is the phenomenon in which a fluid stream tends to stay attached to an adjacent surface. It is responsible for the lift of airplanes and is based on a relatively simple yet highly important mechanism, as depicted in Fig 1.1. Due to the shape of an airplane's wings, the upper surface offers a longer path for air to travel compared to the lower surface. As a result, the air flowing over the upper surface must necessarily have a higher velocity than the air flow beneath the wing. This principle is governed by the continuity equation. Consequently, due to the higher air velocity on the upper wing surface, the pressure in that region tends to be lower (principle of conservation of energy). As a result, the lower pressure exerted on the lower wing surface causes the airplane to lift.

The Coandă effect applied to the fluidic oscillator developed by Zimmerman et al. (2008) can be seen in the scheme in Fig. 1.2.

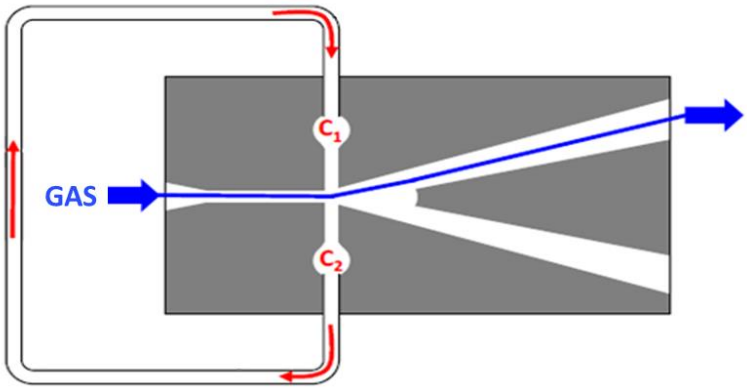

Figure 1.2. Fluidic oscillator scheme. Personal collection.

As depicted in Fig. 1.2, gas enters the fluidic oscillator and establishes its exit solely through one of the ends due to the Coandă effect. Terminals C1 and C2, interconnected by a feedback tube, serve to communicate between the two outlet ducts of the sparger. The flow direction of gas within the feedback tube is reversed when pressure at one end is higher (C2), owing to the decrease in velocity in the outlet duct that it signifies (Bernoulli's principle). This process causes the gas flow from the duct to be directed towards the other exit end (C1), which possesses higher velocity and lower pressure. This sequence of events then repeats continuously, resulting in the pulsating gas flow generated by the alternating airflow between the exit ends of the fluidic oscillator (Tesař et al., 2006).

However, the fluidic oscillator needs to be customized for different process conditions, as the oscillation frequency of the gas pulses is determined by the equipment's construction dimensions. Hence, it's not possible to alter the oscillation frequency for microbubble generation (Brittle et al., 2015a) online, according to varying reactor operational conditions. Based on the studies published so far regarding the fluidic oscillator, there is no data demonstrating its behavior in processes where there are changing reactor operational conditions over time, such as liquid level, temperature, viscosity of the culture medium, and so forth.

An alternative way to generate gas pulses, yet with the flexibility to be adjusted for different operational conditions in real-time, is the utilization of high-frequency solenoid valves. It must be noted that the flow pulses must occur at frequencies above 20 Hz, making the use of solenoid valves for this purpose only possible with the evolving of the technology regarding this equipment, which occurred only in the last years. These high-frequency solenoid valves present low energy consumption and are highly versatile since their operation can be handled by pulse width modulators (PWMs) in online mode. This feature allows the user to switch the frequency and the flow rate of gas depending on the conditions and the specifications of each process.

The key point of the process of disengagement of the bubbles from an orifice regards the force balance as demonstrated by Song et al. (2020). The authors also demonstrated the impact of the duty cycle in the momentum force, indicating the lower duty cycles increase substantially the earlier detachment of the bubbles. The surface tension force is the factor that makes the diameter of bubbles formed tens of times greater than the diameter of the holes, and it is responsible for counteracting the buoyancy force during the bubble formation process. In addition, the chemical structure of the sparger determines whether the sparger is hydrophilic or hydrophobic, which also affects the tension force. Another factor that generates an increase in the diameter of the bubbles generated by spargers is the preferential path formed by the gas inside them. In this case, the geometry of the sparger plays a big role, since it determines the increase in the surface velocity of the gas exit in certain regions to the detriment of others.

The Young-Laplace law (1806) of surface tension (σ) (Zimmerman et al., 2009) describes the process of microbubble formation, as shown in Eq. (1.1). In this equation, the pressure difference (Δp) between the gas and the liquid medium at the orifice outlet of the sparger is inversely proportional to the radius of curvature (R) generated by the gas during the bubble formation process.

$$\Delta p = \frac{2\sigma}{R} \tag{1.1}$$

At the beginning of the bubble formation process through the sparger orifice, the radius of curvature starts with a high value, decreasing rapidly, resulting in an increase in Δp between the gas and the liquid medium. If the bubble were to detach at this point, its diameter would closely match the orifice diameter of the sparger. However, from this point onward, the bubble becomes "anchored" to the orifice wall, causing the radius of curvature to increase again, reducing the pressure difference, facilitating the ingress of air, and leading to the generation of a bubble with a much larger diameter compared to the initial stage of the process (Zimmerman et al., 2009).

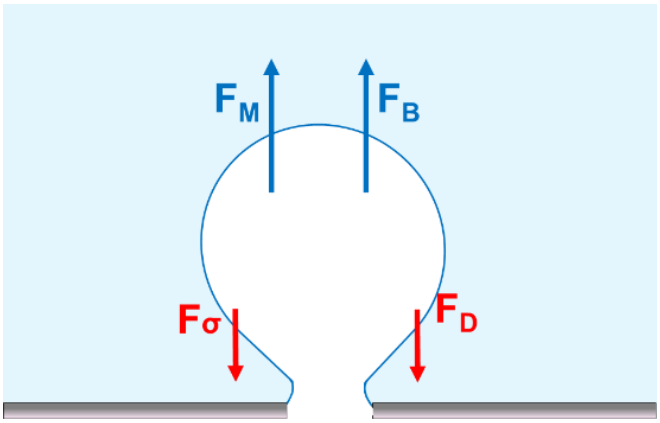

Figure 1.3. Balance of forces during the process of bubble generation. Personal collection.

Fig. 1.3 shows the scheme of the forces acting during the process of the bubble detachment from the orifice. The continuous gas flow rate causes the detachment of the bubble from the orifice of the sparger when its volume is enough to equalize the buoyancy (F_B) and the moment (F_M) forces to the surface tension (F_σ) and drag (F_D) forces. On the other hand, the pulsed gas flow rate generated by the actuation of the high-frequency solenoid valve causes two effects that contribute to the premature detachment of the bubbles from the orifices of the sparger. The first effect is the increase at the moment force (F_M) generated at the end of each pulse, and the second is the even distribution of the gas flow through the interior of the sparger, which prevents the formation of preferential paths of the gas inside the sparger and distributes the volume of gas among all the

orifices. In terms of fluctuations in the gas supply pressure, those are switched between the states of high (on) and low (off) pressures, generating intermittent flow. The scheme of the bubble detachment under continuous and pulsed gas flow rates is shown in Fig. 1.4.

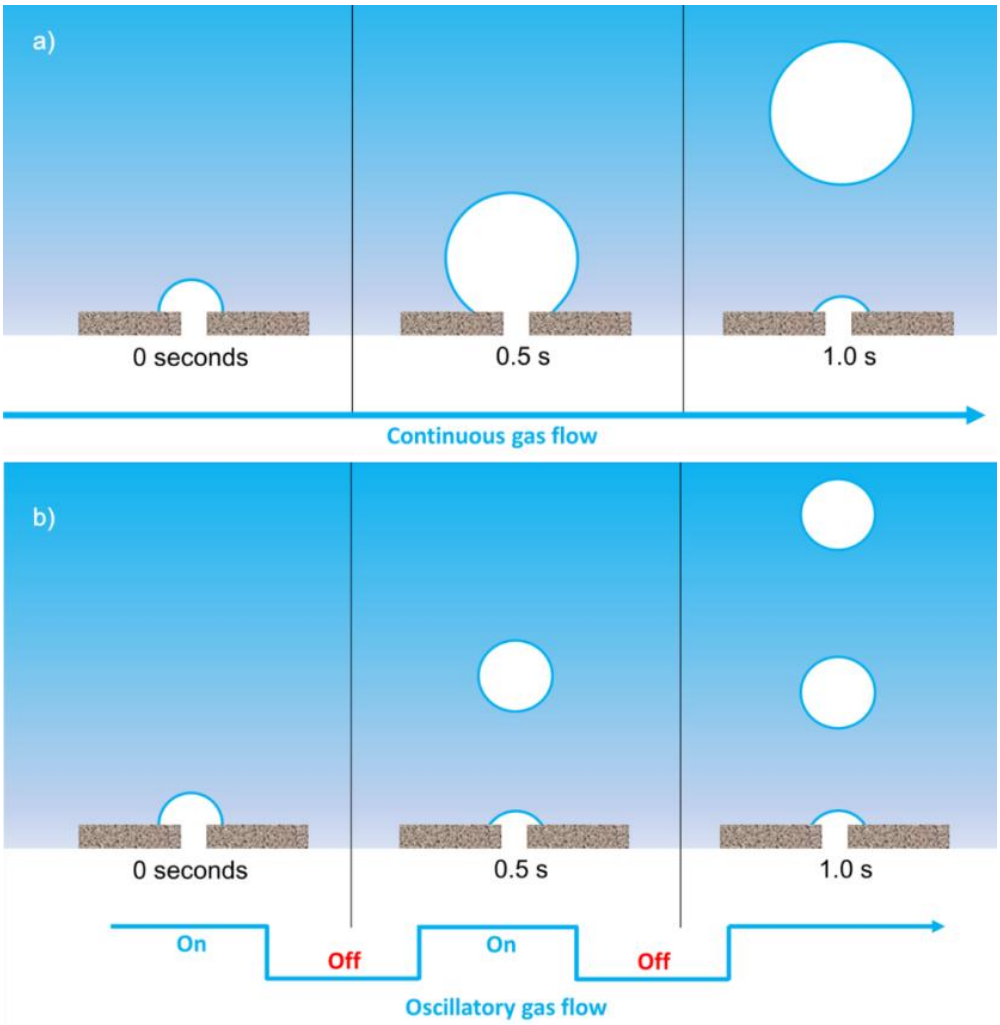

Figure 1.4. Illustration of bubble release under (a) continuous and (b) pulsed gas flow. Personal collection.

The pulsatile flow can be an alternative to release small-sized bubbles through conventional spargers by the effect of the momentum force (Desai et al., 2018; Song et al., 2020). However, one must consider for this type of fine-microbubbles generation there is a natural frequency of bubbles formation through sparges, even for continuous gas flow across it. Das et al. (2011) developed an analytical model to estimate the frequency of bubble formation through submerged orifices of

different diameters and discussed the effect of orifice diameter and the height of liquid above it. The authors also considered many other variables like the gas flow rate, solid-liquid superficial tension, gas pressure, and densities of liquid and gas in the model. Fig. 1.4 also illustrates qualitatively the formation of bubbles with (a) continuous (natural frequency) and (b) oscillatory (frequency above natural frequency) gas flow for the same total volume of gas, resulting in frequencies of 1 and 2 Hz, respectively.

Alkhalidi et al., (2016) carried out experiments of aeration using a pulsatile flow system (< 2 Hz) operated at 42 L min^{-1} in a tank of 750 L. The frequency of aeration of 0.67 Hz increased the oxygen mass transfer efficiency by 57%. However, this gain was due to the establishment of a new path in which bubbles travel, since the oxygen mass transfer is lower when a bubble travels on an oxygenated path by the bubble released before it, as to conclude in the study reported by Dani et al. (2007). In this way, the pulsatile flow of gas using high frequencies not only can cause the premature release of bubbles from the orifices due to the momentum force but also may increase the gas-liquid mass transfer by the effect reported by Dani et al. (2007).

Hanotu et al. (2013) achieved microbubbles with an average diameter of 100 μm using sintered stainless-steel plates with pore diameters around 50 μm. Employing an inlet air pressure of 0.8 bar relative pressure and a reactor measuring 40 x 80 x 25 cm in width, length, and height respectively, bubble diameter was determined through high-speed, high-resolution imaging during a pre-flotation operation carried out with pure water. The frequency used was 267 Hz (defined by the length of the tube in the oscillator – 0.5 m), and an increase in bubble diameter was observed with escalating gas flow rates (from 61 to 65 L min^{-1}).

Brittle et al. (2015) explored various mechanisms for microbubble generation and varied the operating frequency for each to examine its influence on the resulting bubble diameters. They found that the frequency minimizing bubble diameter is contingent on gas flow rate, type of sparger, and the mechanism employed for generating gas pulses. One of the mechanisms examined involved the fluidic oscillator and a commercially available porous ceramic sparger with an average pore diameter of 20 μm. Though the dimensions of the porous sparger were not specified, gas flow rates of 0.1 to 0.35 L min^{-1} were employed in its operation. For the single-orifice sparger device, the superficial gas velocity did not exceed 3.0 mL min^{-1}, indicating that generating microbubbles with pulsed flow requires low superficial gas exit velocities.

Despite not utilizing a fluidic oscillator, Mohseni et al. (2019) investigated the impact of flow rate and micro-orifice sparger types on microbubble formation. They reported maximum air flow rates per orifice ranging from 5 to 50 mL min^{-1}, indicative of the flow rates necessary to achieve satisfactory effects in generating small-sized bubbles.

Al-Mashhadani et al. (2012) delved into the saturation and stripping operations of CO_2 in water using bubbles of approximately 1.3 mm and 500 μm in diameter, the latter obtained using the fluidic oscillator. A boost of approximately 30% in the mass transfer coefficient for CO_2 was attained with the microbubbles compared to larger bubbles. Experiments involved a ceramic sparger with 20 μm pores, operating at a superficial velocity per pore of around 0.02 m s^{-1}. The 8.3 L useful volume reactor employed an air flow rate into the sparger on the order of 300 ml min^{-1}. The superficial velocity closely resembled that used by Zimmerman et al. (2011),for pilot-scale tests – a 2200 L reactor – to study enhanced cellular production of the Dunaliella salina algae, supplied with CO_2 gas from an industrial medium. The air flow rate employed was 80 L min^{-1}, with a pulse gas frequency of 90 Hz. The sparger used was a porous ceramic type with a surface area of 576 cm^2 and approximately 20 μm pores. Beyond the oxygen stripping operation from the liquid medium, which facilitated algae growth rate, the microbubbles physically aided in suspending organic matter on the reactor surface and preventing biofilm formation on the walls. Hanotu et al. (2012) conducted bench-scale studies on the same algae flotation system, noting a reduction of about 28 times in bubble diameter for pulsed flow compared to direct flow.

Zimmerman et al., (2009) utilized a superficial velocity of 0.015 m s^{-1} on a 38-hole sparger with 0.6 mm diameter orifices to achieve microbubbles of approximately 0.8 mm in diameter. Experiments employed a water/air system in a 12 L reactor. The mass transfer coefficient for the system operated at a 90 Hz frequency and direct gas flow was determined. Due to operational limitations associated with low flow rates, the air flow rate for the pulsed system was 2.5 times higher than that of the continuous flow system. Despite this discrepancy, oxygen transfer efficiency for the pulsed gas system was about five times greater than the standard aeration system.

Numerous other processes have been explored to enhance mass transfer efficiency and flotation processes. Hanotu et al. (2016) employed microbubbles to increase oxygen transfer rates during yeast production's propagation and cultivation stages. They also studied the intensified mixing effect caused by microbubble presence. Even at low gas flows, using microbubbles (0.3 mm in diameter), yeast cell production could be increased by 18% compared to conventional

bubbles (3 mm in diameter). Aeration conditions closely matched those used by Zimmerman et al. (2011).

Herrmann-Heber et al. (2019) simulated the scale-up of wastewater treatment to investigate the influence of variables – air pulse oscillation, bubble diameter, and volumetric flow rate – on oxygen transfer. They used simulated air pulse frequencies ranging from 0.1 to 4.0 Hz and achieved a 24% increase in oxygen transfer compared to continuous gas flow. Simulated superficial velocities were less than 0.00148 m s^{-1}. Results indicating an increased volumetric oxygen transfer coefficient were also obtained by Alkhalidi et al. (2016), who employed different conventional solenoid valve opening frequencies, capped at a maximum frequency of 2 Hz. Aeration of a 750 L useful capacity reactor was conducted at flow rates of 14 to 56 L min^{-1}. The increase in volumetric oxygen transfer coefficient compared to non-pulsed flow reached 57%.

Although Alkhalidi et al. (2016) achieved promising results, it is essential for the pulsing device to offer wider oscillation frequency ranges (0 to 100 Hz) to minimize bubble diameters (Tesař et al., 2006). Desai et al. (2018) demonstrated the reduction in microbubble diameter through operation at the bubble detachment resonance frequency. As a result, they achieved a reduction of approximately 60% in microbubble diameter compared to those obtained with pulsed gas flow. However, it's important to note that adjusting the fluidic oscillator frequency necessitates modification of the length of the feedback tube. This can only be performed before the equipment starts operation, rendering it impossible to adjust the pulse frequency for the varying operational conditions that may occur during cultivation.

Numerous authors have proposed equations for calculating the mass transfer coefficient, a parameter commonly used to assess the benefits of microbubble utilization. Tanaka et al. (2019) tested the microbubble mass transfer coefficient model proposed by Ranz and Marshall (1952), which is based on the rate of microbubble diameter decrease during its ascension path. Bredwell and Worden (1998) modeled microbubble mass transfer under steady-state conditions, while Worden and Bredwell (1998) considered transient state conditions. A more practical approach was presented by Cerri et al. (2016) for determining the volumetric oxygen transfer coefficient. They proposed a nonlinear model to adjust the coefficient value, considering the electrode sensitivity as a parameter to be pre-determined and input into the model, and a second approach that eliminates the need for determining this sensitivity parameter.

One important aspect of generating the smaller or even microbubbles through pulsed gas flow or other method is the presence of contaminats in the liquid solution – non-coalescent solutions. Al Taweel et al. (2013) demonstrated the importance of adding the electrolytes in the solution to improve the oxygen mass transfer. The authors carried out experiments in a 173 L pilot-scale airlift reactor, varied the concentration of electrolytes, and aerated the reactor using the two-phase transonic sparger. It was suggested that for a coalescent air-water system the minimum diameter of bubbles reached was 920 μm, while 320 μm for a 1.0 M salt solution, in the same conditions of operation using the transonic sparger. High values of the volumetric oxygen transfer coefficient ($k_L a$) were obtained for salt solutions, reaching a value of 108 h^{-1} for a specific aeration rate of 0.4 vvm. Moreover, the generation of microbubbles by dynamic sparger was more evident when compared to the conventional spargers using the low-coalescent system. The use of a coalescent system may explain the lower $k_L a$ increase compared to the conventional system of aeration, obtained by Al-Mashhadani et al. (2012), using the fluidic oscillator to generate microbubbles. Thus, one can conclude the use of low-coalescent systems is essential to characterize and assess new procedures of fine and microbubbles generation.

Pallapothu and Al-Taweel, (2012) explored the gas hold-up behavior under different concentrations of a cationic surfactant using the same experimental set-up reported by Al-Taweel et al., (2013). The authors showed the excellent performance of the dynamic sparger varying the pressure drop across it to tune different Sauter mean bubble diameters. The results pointed out the benefits of using the new apparatus to generate fine and microbubbles, which resulted in higher gas hold-ups in the riser compared to the conventional sparger systems. It is worth mentioning the fact reported by the authors regarding the presence of small-sized bubbles in the downcomer region, which hindered the full achievement of recirculation velocity due to the lower pressure difference between the riser and downcomer regions. This corroborates the fact that as microbubbles rise and transfer mass, they start behaving like solid spheres as reported by (Hafeez et al., 2020).

1.2.3 Oxygen Mass Transfer Process

Whitman's theory of two stagnant films, introduced in 1962, finds extensive application in illustrating how solute mass transfers from the gas phase to the liquid phase. This theory posits the existence of a thin stagnant fluid film on both sides of the gas-liquid interface, serving as the

conduit for mass transfer solely through molecular diffusion. Fig. 1.5 elucidates the concentration profiles of component A within each phase. Within the gas phase, the partial pressure of "A" (P_{AG}) diminishes until it aligns with the partial pressure at the interface (P_{Ai}). Conversely, in the liquid phase, the concentration of "A" at the interface (C_{Ai}) diminishes to match the concentration within the bulk liquid (C_{AL}). The theory also asserts that the primary resistance to mass transfer occurs within these films. Notably, at the interface, resistance is minimal, thereby enabling the consideration of P_{Ai} and C_{Ai} as equilibrium compositions.

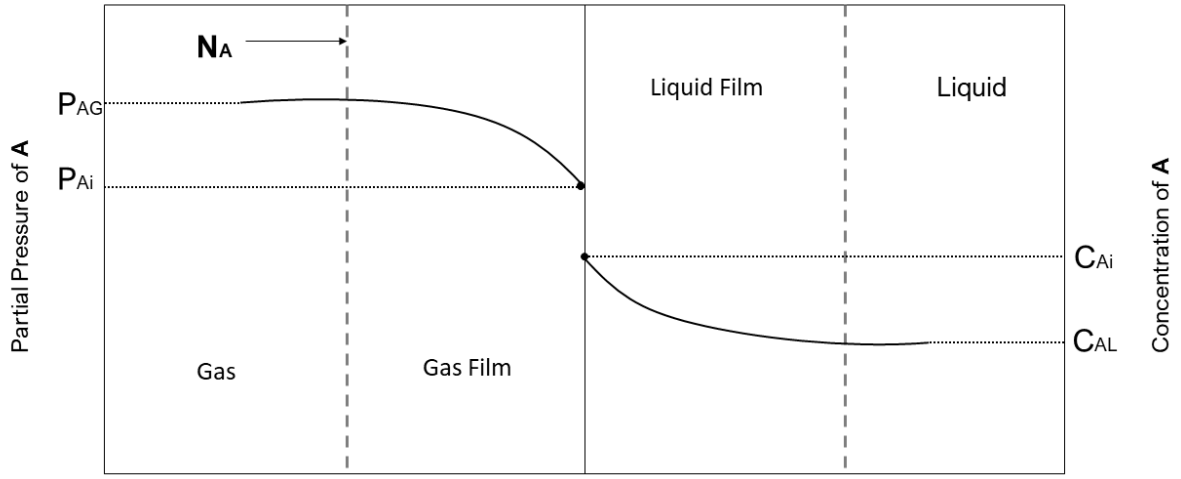

Figure 1.5. Concentration profiles of component A in the gas and liquid phases according to the theory of two stagnant films. Adapted from Treybal (1980).

Under the assumption of steady state, the rate at which solute A reaches the interface from the gas phase must be equal to the rate at which it diffuses into the liquid bulk. The molar flux of A (N_A) in each phase can be written in terms of appropriate mass transfer coefficients and concentration variations, as described by Eqs. (1.2) and (1.3).

$$N_A = k_G(P_{AG} - P_{Ai}) \tag{1.2}$$

$$N_A = k_L(C_{Ai} - C_{AL}) \tag{1.3}$$

Where k_G and k_L are the local gas and liquid coefficients of mass transfer.

Experimentally, it's feasible to obtain samples and determine the solute concentration in the fluid bulk (P_{AG} and C_{AL}). However, there are no sampling methodologies that enable the collection of composition data at the interface (P_{Ai} and C_{Ai}). Therefore, the molar flux of A can be conveniently expressed in terms of overall mass transfer coefficients, as shown in Equations 1.4 and 1.5.

$$N_A = K_G(P_{AG} - P_A^*) \tag{1.4}$$

$$N_A = K_L(C_A^* - C_{AL}) \tag{1.5}$$

Where K_G and K_L are the overall gas and liquid coefficients of mass transfer, P_A^* is the partial pressure of A in the gas in equilibrium with the C_{AL} concentration, and C_A^* is the concentration of A in the liquid in equilibrium with the P_{AG}.

In most industrial applications involving gas-liquid mass transfer, the interfacial area is irregular and unknown. In such situations, it is convenient to define a volumetric mass transfer coefficient, incorporating the interfacial area (a) per unit volume. Consequently, the rate at which solute A is transferred to each phase ($\dot{r}_A$) can be defined by Eqs. (1.6) and (1.7). The interfacial area (a) in the cases presented in this study corresponds to the area of bubbles generated per unit volume of bubbles.

$$\dot{r}_A = K_G a(P_{AG} - P_A^*) \tag{1.6}$$

$$\dot{r}_A = K_L a(C_A^* - C_{AL}) \tag{1.7}$$

Where $K_G a$ and $K_L a$ are the overall volumetric coefficients based on the gas and liquid phases.

For oxygen transfer processes from the gas phase to the liquid phase, the resistance of the gas phase is disregarded, and only the liquid phase is considered as the limiting step for mass transfer. This is because the solubility of oxygen in the liquid phase is much lower than in the gas phase (air). Thus, $K_L a$ in Eq. (1.7) can be approximated by $k_L a$ and Eq. (1.8) can be used to describe the oxygen transfer on aeration processes.

$$\dot{r}_A = k_L a(C_A^* - C_{AL}) \quad (1.8)$$

Where $\dot{r}_A$ is the rate of oxygen transfer (g L h^{-1}), $k_L a$ is the oxygen volumetric transfer coefficient (h^{-1}), C_A^* is the oxygen saturation concentration in liquid phase (g L^{-1}), and C_{AL} is the oxygen concentration in liquid phase (g L^{-1}).

The solubility of oxygen from air in water (C_A^*) at 25°C and 1.0 atm of pressure is around 8.6 10^{-3} g L^{-1} (Xing et al., 2014) and the convective oxygen transfer coefficient (k_L) can be considered 3.5 10^{-4} m s^{-1} in distilled water for conventional operating conditions in a bubble column reactor (Cerri et al., 2010).

1.2.4 Stripping Process

The stripping process emerges as a separation technique characterized by the introduction of a gas into a liquid solution. This dynamic triggers the migration of one or more compounds from the solution into the gas phase. The driving force behind this process hinges on the fundamental thermodynamic equilibrium of vaporization, enabling the targeted removal of volatile organic compounds (Hamer, 1965; Kujawska et al., 2015). In a comparative analysis with alternative separation methods, gas stripping boasts notable advantages. Its operational simplicity and economic viability are rooted in the potential utilization of CO_2 generated for the case of ethanol fermentation process—yielding around 425 liters of CO_2 per liter of ethanol produced. This inherent potential makes gas entrainment particularly attractive for large-scale ethanol fermentation applications. Furthermore, its non-disruptive impact on nutrient content within the fermentation medium and its benign interaction with cells during the fermentation process underscore its appeal (Ezeji et al., 2005; Sonego et al., 2014b).

The process of extracting solvents from aqueous solutions via gas entrainment aligns with a first-order kinetic model initially proposed by Truong and Blackburn (1984), elucidated in Equation 1.9. This model's adaptability has facilitated its widespread adoption in assessing gas entrainment across diverse fermentation scenarios (Chen et al., 2014; De Vrije et al., 2013; Sonego et al., 2016a).

$$\dot{r} = \frac{dC}{dt} = k_s a \cdot C \tag{1.9}$$

Where $\dot{r}$ is the velocity of solvent removal from the liquid phase (g L h^{-1}), C is the solvent concentration in the liquid phase (g L^{-1}), and $k_s a$ is the constant of solvent removal (h^{-1}).

The process of stripping occurs in the reverse manner to the absorption process outlined in Fig. 1.5, which is based on the theory of double films. In the case of stripping, the species "A", which is present in higher concentration in the liquid phase, migrates to the gas-liquid interface ($C_{Ai} < C_{AL}$) and moves into the gas phase, where its partial pressure at the gas-liquid interface (P_{Ai}) is higher than in the gas bulk (P_{AG}). Considering the high solubility of the species “A” in the liquid phase and the main resistance for the mass transfer lies on the gas phase, one can consider Eq. (1.10) as the ruling the removing of species “A” from liquid phase due to the vaporization phenomena.

$$\dot{r}_A = k_G a(P_A^* - P_{AG}) \tag{1.10}$$

The difference between the coefficients k_s and k_G shown in Eqs. (1.9) and (1.10), respectively, the first one is a kinetic coefficient and regards both effects of vaporization and mechanical entrainments, while the second is due to the transport phenomena process solely.

The value of P_A^* corresponds to the maximum partial pressure of component “A” can reach in the gas phase, and it is determined by the thermodynamic equilibrium, which can be determined using Raoult’s Law modified for the liquid-vapor equilibrium, as shown in Eq. (1.11).

$$P_i^* = y_i P = \gamma_i x_i P_i^{sat} \tag{1.11}$$

Where y_i is the molar fraction of specie “i” in the gas phase in equilibrium to the liquid phase (-), P is the operating pressure (Pa), γ_i is the activity coefficient of specie “i” estimated by the NRTL model, x_i is molar fraction of specie “i” in the liquid phase, and P_i^{sat} is vapor pressure of specie “i” calculated by Antoine’s Equation (Pa).

Ezeji et al. (2005) conducted an estimation of the time required for a bubble to reach saturation in butanol as it passes through a liquid solution containing the binary water-buthanol system. The author's calculations were based on methodologies for determining mass transfer coefficients and on parameters already established in the literature (Cussler, 2009). The authors estimated a time of 0.14 seconds for a bubble with a diameter of 5.00 mm to reach the saturation point established by thermodynamic equilibrium under the given conditions of pressure, temperature, and liquid phase concentration carried out in the experiments. Utilizing the identical methodology adopted by the authors and employing the parameters pertinent to the ethanol-water-air system, it is viable to derive the estimated value of $(k_G \cdot P^*)$ for ethanol in air, which results in $1.45.10^{-2}$ m s^{-1}. Roughly comparing the process of stripping and aeration, the removal of ethanol by air is around 50 times faster than the oxygen transfer to water. Considering the molar fraction of ethanol in the gas phase at the thermodynamical equilibrium and converting it to concentration considering the molar gas phase, $C_G^{EtOH} = 3.1\ 10^{-2}$ g L^{-1}.

Martins et al., (2020) evaluated the hydrodynamics and mass transfer characteristics of ethanol removal by CO_2 stripping in bubble columns and airlift reactors operating at scales of 2.0, 5.0, and 10.0 L. It is noteworthy that the kinetic removal coefficient for ethanol remains consistent regardless of the operating scale, being solely dependent on the CO_2 gas flow rate, which means may the main phenomena governing the stripping process was the vaporization entrainment. However, the difference in the concentration factor reached for the scale of 10 L may indicate that there is another phenomenon related to the height of liquid occurring which is not the vaporization entrainment and may be the mechanical entrainment.

As previously mentioned, apart from their application in industrial aeration processes, stripping operations can also reap benefits from the utilization of small-sized bubbles, particularly in the context of the bioethanol industry, which is the focus of our interest. The adoption of carbon dioxide (CO_2) as a stripping agent has emerged as a viable strategy for facilitating extractive fermentation in bioethanol production in Brazil, aimed at mitigating the inhibitory impact of accumulated ethanol within the fermentation broth. Notably, the CO_2 gas generated during the fermentation process does not compromise cell viability and contributes to a significant upsurge in ethanol productivity (Ponce et al., 2016; Rodrigues et al., 2018; Sonego et al., 2016b)

However, achieving the effective rates of ethanol removal as reported in the literature requires the operation to be conducted at high specific flow rates (2.5 vvm) (Ponce et al., 2016;

Rodrigues et al., 2018; Sonego et al., 2016b). While this value can be readily attained in bench-scale fermentation setups, it becomes unfeasible for industrial bioreactors with working volumes approaching approximately 1,000 m^3. Consequently, microbubbles, and even fine bubbles, emerge as a promising alternative for conducting stripping operations. This potential has been demonstrated by Calverley et al., (2020) who successfully conducted ethanol stripping using heated microbubbles derived from an aqueous solution. However, it's important to acknowledge that the scale of the reactor and the gas flow rate employed in their study are not viable on a larger industrial scale.

Calverley et al., (2020) demonstrated the effectiveness of ethanol removal from a liquid medium using hot microbubbles. However, it should be emphasized that in the study conducted by the authors, the gas at 120°C enters the liquid phase maintained at 60°C, which leads to several simultaneous heat exchange phenomena, hindering a proper assessment of the effects of ethanol and water removal separately. A correct analysis of the removal effects separately could clarify the reasons why the gas leaves the reactor with an ethanol concentration above thermodynamic equilibrium values, which are base in the quantification of the removal of the solvent due to vaporization and mechanical entrainments.

1.3 Objective

The project's initial objectives were to develop a new system for generating fine bubbles using pulsed gas flow in conjunction with spargers that could be adapted for pilot-scale or industrial-scale applications. Following the validation of this innovative system's efficiency, the focus shifted to its application in mass transfer operations, as oxygen transfer processes, and specially in stripping operations. Specifically, within the stripping process, the goal was to gain insights into the phenomenon of ethanol removal through thermodynamic (vaporization-induced) and mechanical entrainments. Additionally, the study aimed to understand the role and effects of different bubble diameters in the ethanol removal process, considering their influence on both thermodynamic and mechanical entrainment mechanisms.

This thesis is divided into 6 chapters, which can be summarized in the following description.

- Chapter 1: Introduction, literature review and objectives of the project. In this chapter we sought to introduce the topic of small bubbles generation, the challenges of producing them and their suitable applications regarding mass transfer operations, especially the oxygen transfer and stripping processes.

- Chapter 2: Characterization and assessment of a new system to generate fine bubbles comprised by the pulsed gas flow mechanism and spargers which could be applied at pilot and industrial scales. In this chapter the Fine Bubbles Generator (FBG) system was applied at pilot scale – bubble column reactor of 173 L, and the bubbles generated by the system were assessed regarding their diameters under different operation conditions (frequency of solenoid valve operation, gas flow rate, liquid solution), using the Dynamic Gas Disengagement (DGD) and the image analysis acquisition methodologies.

- Chapter 3: Fine and microbubbles applied to oxygen mass transfer operations. In this chapter the system validated at pilot scale was applied at bench scale bubble column reactor (10 L) to assess the volumetric mass transfer coefficient ($k_L a$) for different operating conditions (frequency of solenoid valve operation, gas flow rate, and liquid composition). The results of diameter of bubbles were compared to the diameter of bubbles generated at pilot scale, discussed in Chapter 2.

- Chapter 4: Together with Chapter 2, this chapter comprises the main contributions of this thesis. The stripping process is performed, and the efficiency of the ethanol removal is assessed under different process operating conditions (height of liquid column, flow rate, and diameter of bubbles). The saturation of the bubbles in ethanol is validated and a methodology is proposed to evaluate and quantify the removal of ethanol from the liquid phase due to thermodynamic and mechanical entrainments separately. Those results are quantified and analyzed in order to determine the influence of each diameter of bubble in the process of stripping.

- Chapter 5: Ethanol fermentations are carried out in the scales of 2.0, 10.0 and 50.0 L, to evaluate the influence of the stripping process using the FBG system (10.0 and 50.0 L scales).

- Chapter 6: Summary of the main conclusions regarding the results obtained in the previous chapters and the perspective for the future studies regarding the application of fine bubbles and the FBG system.

Chapter 2

Characterization of a New System to Generate Fine Bubbles

2.1 Introduction

The mass transfer phenomena between phases in gas-liquid systems are of paramount importance and can, in certain cases, restrict the productivity of various bioprocesses. Introducing gas via spargers into a liquid medium creates a two-phase system comprising gas bubbles dispersed within the liquid phase. These bubbles are responsible for the inter-phase mass transfer. Bubbles with diameters below 100 μm are termed microbubbles, while those ranging from 100 to 3.0 mm are referred to as fine bubbles. Both types exhibit a larger interfacial area (total bubble area per unit gas volume) compared to bubbles with diameters exceeding 3.0 mm, thereby enhancing the mass transfer between phases. Regarding momentum transfer, the cluster of fine bubbles has a lower displacement velocity within the liquid phase, leading to reduced shear stress, longer residence time, and increased gas retention (Song et al., 2021).

There are many methods to generate small bubbles (Tesař, 2017; Zimmerman et al., 2009). However, the use of pulsed gas flow has demonstrated versatility, cost-effectiveness, and reliable, substantial outcomes for producing small-sized bubbles suitable for industrial operations such as distillation, flotation, and oxygen transfer in bioreactors. Pulsed flow involves transitioning the continuous gas inflow into the sparger to an intermittent one using mechanical devices that control the release and cessation of gas supply (Brittle et al., 2015b). This process results in gas flow pulses. The mechanical devices employed to generate gas flow pulses include fluidic oscillators grounded in the Coandã effect or high-frequency solenoid valves (Abdulrazzaq et al., 2016a; Song et al., 2021; Zimmerman, et al., 2009). Notably, these flow pulses must occur at frequencies exceeding 20 Hz, rendering the use of solenoid valves for this purpose feasible only with advancements in relevant technology, which have occurred in recent years. Those high-frequency solenoid valves exhibit minimal energy consumption and exceptional versatility since their operation can be managed by pulse width modulators (PWMs) in real-time mode. This capability enables users to adjust both the frequency and gas flow rate according to process conditions and specifications.

The system proposed in this research project, termed the Fine Bubbles Generator (FBG), employs pulsed gas flow generated by a high-frequency solenoid valve to produce fine bubbles. This apparatus also incorporates spargers equipped with conventional orifices (300 and 500 μm in diameter), distinguishing it from other studies in the literature (Desai et al., 2021) that combine pulsed flow with sintered or porous spargers. Due to the application of this new technology in the

Brazilian ethanol industry being the research project's aim, it was imperative to evaluate the new system on a pilot/industrial scale. Additionally, an alternative methodology for measuring and assessing bubble diameters, distinct from image analysis, was employed. While image analysis is the most prevalent technique for measuring bubble diameter (Tesař, 2014; Tesař et al., 2006; Zimmerman et al., 2008), its applicability depends on the reactor's scale and the liquid medium composition, posing challenges regarding the requisite light conditions and equipment (high-speed cameras) for reliable image acquisition.

Therefore, the primary objective of this chapter is to characterize and assess the FBG system using an alternative methodology for measuring bubble diameters. The research group led by Prof. Adel M. Al-Taweel at Dalhousie University (Halifax, Canada) provided the necessary facilities for characterizing the FBG system. This marked the first instance of operating a pulsed gas flow system with a solenoid valve at a reactor scale of 180 L (6.0 m height and 0.2 m diameter), facilitated by the Canadian research group. Determining the pressure beneath the sparger and the operating volume was a pivotal milestone in qualifying the system for pilot/industrial-scale applications. Furthermore, the Dynamic Gas Disengagement (DGD) methodology firstly proposed by Sriram and Mann (1977) was implemented as an algorithm by Al Taweel et al. (2013) to ascertain and evaluate bubble diameter generated by their bubble generation system. The DGD methodology leverages the hold-up profile, calculated using pressure measurements at the reactor's bottom and top, to determine bubble diameter. This methodology was subsequently applied to the FBG system under diverse operating conditions, including solenoid valve frequency, liquid medium composition (coalescent and non-coalescent), and gas flow rate. The outcomes validated the FBG system's application as a device for reducing bubble diameter in pilot-scale operations.

The FBG system resulted in a patent application to Instituto Nacional de Propriedade Industrial (INPI), Brazil, under the process number BR 10 2023 016822 1, submitted on August 22, 2023. Patent title: “Sistema de geração de bolhas finas, processo de geração de bolhas utilizando o sistema e uso do sistema em processos químicos e bioquímicos” (“Bubble generation system and process, and its use in chemical and biochemical processes”).

2.2 Objective

Characterize the FBG system regarding the generated diameter of bubbles using the Dynamic Gas Disengagement technique for different gas flow rates of gas, frequency of operation of the solenoid valve, and composition of the liquid phase.

2.3 Materials and Methods

2.3.1. The Setup

The scheme of generating fine bubbles by the FBG system for the experiments carried out during the internship period is depicted in Fig. 2.1. First, pressurized air was supplied by a compressor at pressure P1 (8.0 bars) and controlled at pressure P2 (3.5 bars) by a pressure regulator equipped with a gas filter to retain solid particles and oil. A gas flowmeter was used just before the solenoid valve which was supplied by the gas at a pressure of 3.5 bar. The valve was energized with a 24 V power source and was operated by the signals generated by a Pulse Width Modulation (PWM) board. After passing through the valve, the gas pulse passed through a unidirectional check valve, which prevented the backflow of liquid from the reactor to the FBG system, and then was injected into the sparger. The pulsed gas flow rate was then distributed through the orifices of the sparger where the bubbles were formed in the reactor.

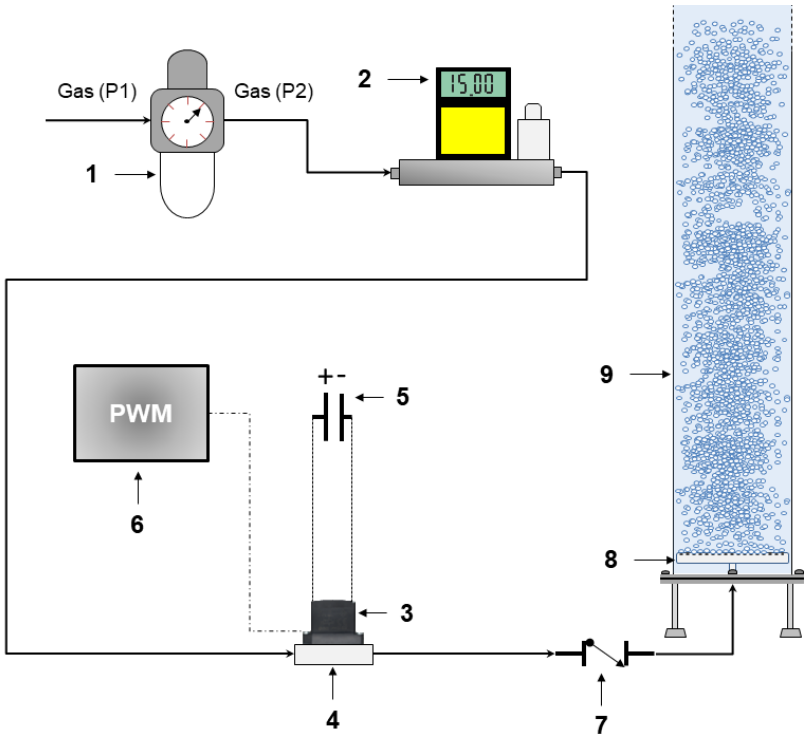

Figure 2.1. Scheme of the system used to carry out the experiments. (1) Pressure regulator with filter, (2) gas mass flowmeter, (3) high-frequency solenoid valve, (4) base of fixation of the solenoid valve, (5) 24 V power supply, (6) Pulse Width Modulation (PWM) board, (7) check valve, (8) sparger, and (9) reactor.

The 180 L reactor or gas/liquid contactor is made up of four flanged acrylic cylindrical sections comprising a total height of 6,000 mm and 197 mm ID (6.35 mm wall thickness, 12 mm flange thickness) stacked on top of each other and equipped with four 51 mm thick solid inter-flange spacers made from high-density polyethylene (HDPE). The spacers between the sections are used to provide means for introducing various instruments (e.g. probes to measure liquid velocity, pressure transducers, thermocouples, conductivity probes, and DO meter sensors as well as ports for observation/photographing) to monitor the hydrodynamic, mixing, and mass transfer performance of the G/L contactor at different locations along with the column. There were two pressure transducers installed in the column, each one used to measure the pressures of the bottom and the top of the reactor during the experiments. The pressure transducers installed at the top and the bottom of the reactor were the Honeywell FPG 0-5 psig (Columbus, Ohio, USA) and Cole-Parmer RK-68075-42 0-10 psig, respectively. The picture of part of the reactor is shown in Fig 2.2.

Figure 2.2. Reactor or gas/liquid contactor of 180 L used in the experiments. (1) the reactor, (2) a flat black plate used as a background for image acquisition, and (3) the sparger of FBG system brought from Brazil.

2.3.2. Generation of the Pulsed Gas Flow

The high-frequency solenoid valve SMC, model SX11F-AG, 80 W, 50 L.min^{-1}, 1200 Hz (max. operating frequency) was used to generate the pulsed gas flow, as shown in Fig. 2.3. The two operating variables of the high-frequency valve were the frequency of operation and the duty cycle. The frequency of operation is determined as the number of times the opening and closing cycle is performed every 1 s. The duty cycle is the ratio of opening time to the total time in each cycle. This last one can vary from 0% (close all the time) to 100% (open all the time) which is the continuous flow rate. To preserve the solenoid valve the manufacturer advises not to exceed the duty of 25% in order to prevent overheating the device.

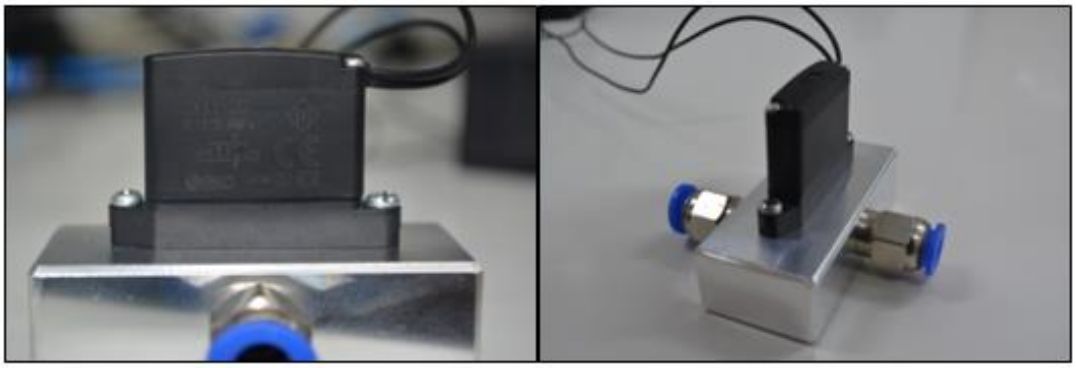

Figure 2.3. High-frequency solenoid valve.

The frequency and duty cycle signals sent to operate the solenoid valve were generated by a 150 KHz PWM signal generator module Model HW-753, as shown in Fig. 2.4, which can be easily replaced by any other model that meets the valve operating specifications or signal generation software such as LabView. The operating frequency of the solenoid valve varied from 20 to 160 Hz during the experiments, while the duty cycle ranged up to 12%. The gas flow rate was adjusted by changing the value of the duty cycle signal while operating through the pulsed gas flow conditions. However, the experiments using the continuous gas flow rate were performed without using the solenoid valve or the PWM module. In this case, the gas flow rate was manually adjusted using the software which controlled the gas flow set point of the mass flowmeter.

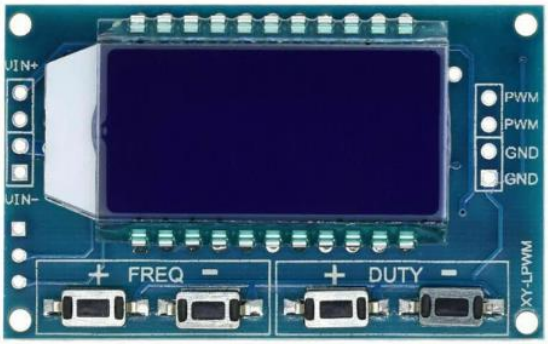

Figure 2.4. PWM module to control the solenoid valve.

2.3.3. Sparger

The sparger was built in Brazil and sent to the gas/liquid facilities at Dalhousie University to be used in the experiments. The sparger called H3 had orifices of 300 nm in diameter drilled in polyacetal material, in a cylindrical shape as shown in Fig. 2.5. The external diameter of the sparger

was 190 mm with a central opening on their bottom to the gas entrance. Internally, 16 ducts evenly spaced in 4 mm with a depth of 3 mm were drilled to distribute the flow rate of gas in the 1503 orifices. Each orifice was evenly spaced from each other by 3.3 mm (center to center) with a length of 3 mm. The length of 3 mm of the orifice ducts was an attempt of preventing the backflow of liquid to the internal parts of the spargers during the pulsed gas flow in the process. The longer the length, the fewer the chances of backing flow, but the higher the chances of preferential paths being formed. In order to fit the sparger in the setup, there was a need of rebuilding the bottom part of the column, which happened to be a very meticulous procedure.

Figure 2.5. Sparger H3.

2.3.4. Liquid Solutions

All experimental runs were conducted using Halifax city water which is relatively low in dissolved solid concentration and total organic carbon. The coalescence-retarding tendency of such water was altered by adding minute amounts of Sodium Dodecyl Sulfate (SDS) ($C_{12}H_{25}SO_4Na$, 288.38 g/mol, Product No. L-5750 Lot # BCBS411V, made by Sigma Chemical Co., 92-100.5 % based on alkyl sulfate basis content), which is well known to alter the gas/liquid interface and retard bubble coalescence. Two types of liquid solutions were performed. The first one was only tap water (coalescent solution) and the other was comprised of a solution of 20 ppm of SDS.

The liquid solution was prepared by filling one of the two polyethylene storage tanks (500-L each) with tap water up to the 490-L level. Based on the volume of the water added, the necessary amount of the additive SDS was weighed and mixed into the water using an off-center portable mixer (Model No: NS-1VM, TPR, 1/3 HP, 1725 RPM, GREEY Mixing Equipment Limited, LIGHTNIN, Toronto, Canada). A high-capacity centrifugal pump (Rockingham Hardware

Limited; 85 GPM; 85 Psi) was used to fill the column. The flow rate of the aqueous solution was manually controlled and monitored using an inline liquid flow meter (GPI US Model No: 01N31GM, 0-95 L min^{-1}, ±3% FS). At the end of each series of experimental runs, the whole system (column, storage tanks, interconnecting piping) was drained, and the setup was thoroughly washed at least five times using tap water to eliminate the presence of contaminants in the system in a fashion that may affect future runs.

2.3.5. Data Acquisition

The experimental setup was connected to a data acquisition and control system that enabled the carrying on of the experiments at the required pre-set experimental conditions. It also recorded the values of several manually adjusted operating parameters, and the temporal variation of the various parameters during the steady-state operation as well as during the DGD run. This was accomplished using three National Instruments data acquisition boards.

The first board was NI PCIE-6321, with 16 analog input channels and 2 analog output channels, with a sampling rate of up to 250,000 samples/s and a resolution of 16-Bit, 24 DIO. The second one was a NI USB-6001 with 8 analog input channels and 2 analog output channels, with a sampling rate of up to 20,000 samples/s and a resolution of 14-Bit,13 DIO. The differential pressure signals (DP) obtained from DP1 and DP2 were samples using the National Instruments board NI-9237, 4 AI, operating at the rate of 50,000 samples/s. These were used to acquire the signals from the pressure transducers and interface with the PC.

The output signals from 11 points in the setup were continuously monitored at an adjustable rate. Their corresponding values were stored on the hard drive in Excel files. The output signals were connected to a computer to record and analyze the data. The data acquisition/control system monitored several experimental parameters such as pressure, temperature, oxygen concentration, and conductivity and controlled the main operating parameters like gas flow rate. The experimental parameters control, data acquisition, and analysis of the results were managed by an interface built using LabVIEW version 17 as can be seen in Fig. 2.6.

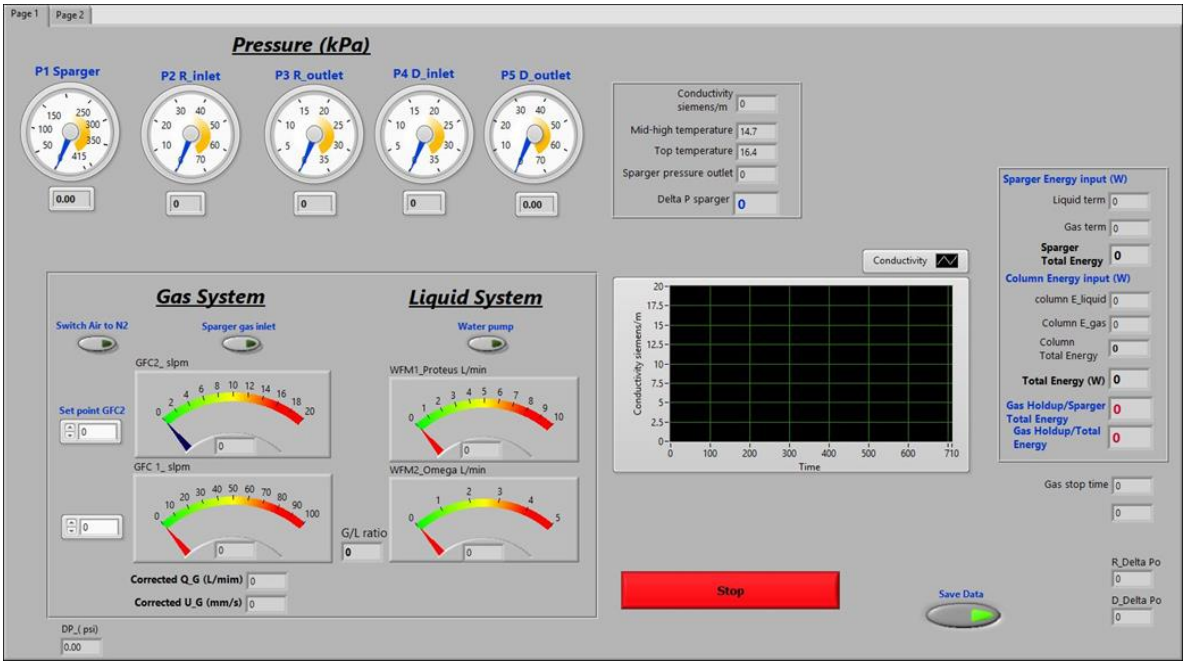

Figure 2.6. Setup control panel in LabVIEW.

2.3.6. DGD Methodology

The dynamic gas disengagement technique (DGD) was introduced by Sriram and Mann (1977) and has since been used to estimate the bubble size distribution encountered in gas-liquid contactors operating in homogeneous and heterogeneous flow regimes. It classifies the bubble size distribution (BSD) into classes of bubble size for aqueous systems with or without contaminants. It is based on relatively simple assumptions, and its accuracy was significantly improved by taking into account the effect of the downward-moving liquid flow needed to compensate for the volume of gas disengaged (Schumpe and Grund, 1986). The DGD technique states that under a steady state, there are bubbles of different sizes in the gas-liquid dispersion, and this generates a global steady-state hold-up of the system, calculated by pressure transducers at the bottom and top of the reactor, as stated in Eqs. (2.1) and (2.2). By the time the aeration is ceased, bubbles start disengaging, however, each class of diameter of bubbles will have its disengagement profile with time. The global hold-up of the system will decrease in a profile comprised of all the disengagement profiles of each class of bubbles. This global profile will determine the number and diameter of each class of bubbles.

$$\Delta P = (P_B - P_T)_0 - (P_B - P_T)_A \tag{2.1}$$

$$\varepsilon = \frac{\Delta P}{\rho_L \cdot g \cdot H_L} \tag{2.2}$$

Where, P_B and P_T are the absolute pressure at the bottom and top of the column (kPa) before aeration starts (subscript "0") and during aeration (subscript "A"); ρ_L is de density of the liquid solution (kg m^{-3}); g is the gravity acceleration (9.8 m s^{-2}); and H_L is the distance between the two points of pressure measurement at the bottom and top of the column (m).

The procedure adopted for the experiments was to start the aeration process at the set conditions of frequency and gas flow rate and wait until the steady state was reached. The time to reach the steady state was observed to be around 180 seconds, which corresponds to the moment the pressure measurements did not change anymore. After the steady state was reached, the gas flow rate ceased and the acquisition data system started to acquire the pressure data from the transducers placed at the bottom and at the top of the column, to obtain the hold-up profile with the disengagement of the bubbles. This process lasted around 5 minutes for each run and it was determined by the moment the pressure measurements were constant. Fig 2.7 shows the procedure of the DGD technique applied to the FBG system in the experimental setup.

A general approach for extracting multi-class BSD from the DGD results was developed by Patel et al. (1989) and used by Daly et al., (1992) and Basha and Morsi (2018) to determine multi-class BSD encountered in pilot-scale bubble column reactors filled with relatively viscous paraffin wax. To enhance the accuracy and reliability of this technique, several investigators recently combined electrical resistance tomography (ERT) with the DGD technique to gain better insight into the gas holdup present in the vessel and its axial and radial distribution.

The methodology developed by Leng et al. (2022) uses a modular approach for selecting the models describing the drag on bubbles and how it is affected by the presence of contaminants and adjacent bubbles (i.e. gas holdup); thus providing the flexibility of using a wide base of fundamental information that enables for its use over a wide range of contaminated systems. The approach adopted by the group addresses many of the shortcomings associated with previous investigators of the DGD technique by taking into account both the temporal and axial variation of the gas holdup associated with various bubble size classes as well as the downward liquid

velocity that is driven by bubble disengagement. For situations where the first aforementioned two assumptions are satisfactorily approached, the use of the newly developed approach provides bubble size estimates that are close to those obtained using CFD analysis, particularly when a relatively large number of bubble size classes are used. To estimate BSDs from the experimentally measured DGD data (varying gas holdup as a function of the time), a series of algorithms were developed as automated as possible in Excel VBA. The overall logic flow diagram is shown in Fig. 2.8.

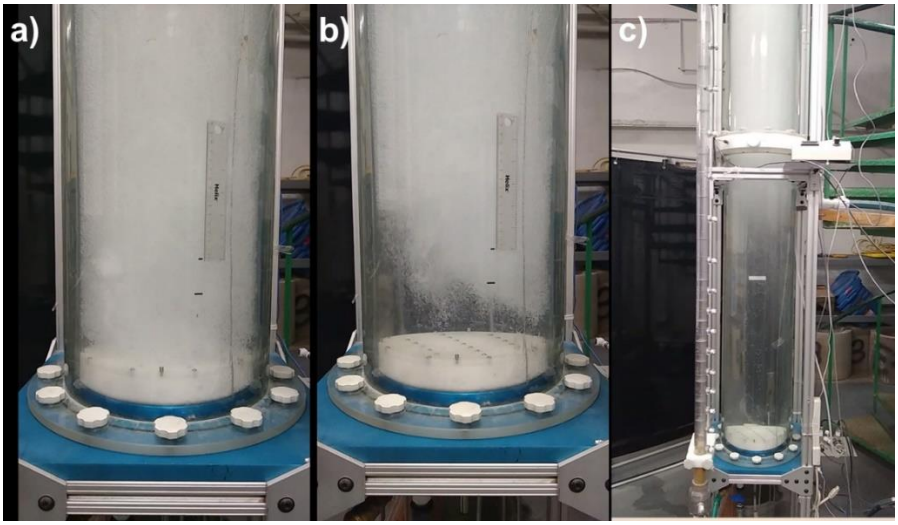

Figure 2.7. DGD methodology applied to the FBG system. (a) flow rate at the steady state; (b) ceasing of the aeration and starting pressure data acquisition; and (c) process of disengagement of bubbles**.**

The rise velocity of single bubbles is strongly affected by the bubble size and the extent of interfacial contamination, and many equations/correlations have been proposed for estimating the rise velocity of bubbles in the water. The DGD data analysis program is therefore provided with the option to select amongst 12 different well-accepted bubble rise velocity expressions. The model to estimate the effect of adjacent bubbles with the lowest deviation compared to the results obtained using image analysis was the one proposed by Griffith and Wallis (1961), and thus chosen for all the estimations of d_{32}. Under the same consideration, the model to estimate the effect interfacial contamination of the solution was the proposed by Karamanev (1996) for fully

contaminated Newtonian liquids, for which the drag coefficient (C_D) can be calculated as shown in Eq. (2.3).

$$C_D = max\left(\frac{24}{Re}(1 + 0.173 \cdot Re^{0.657}) + \frac{0.413}{1 + 16300 \cdot Re^{-1.09}} \cdot 0.95\right) \quad (2.3)$$

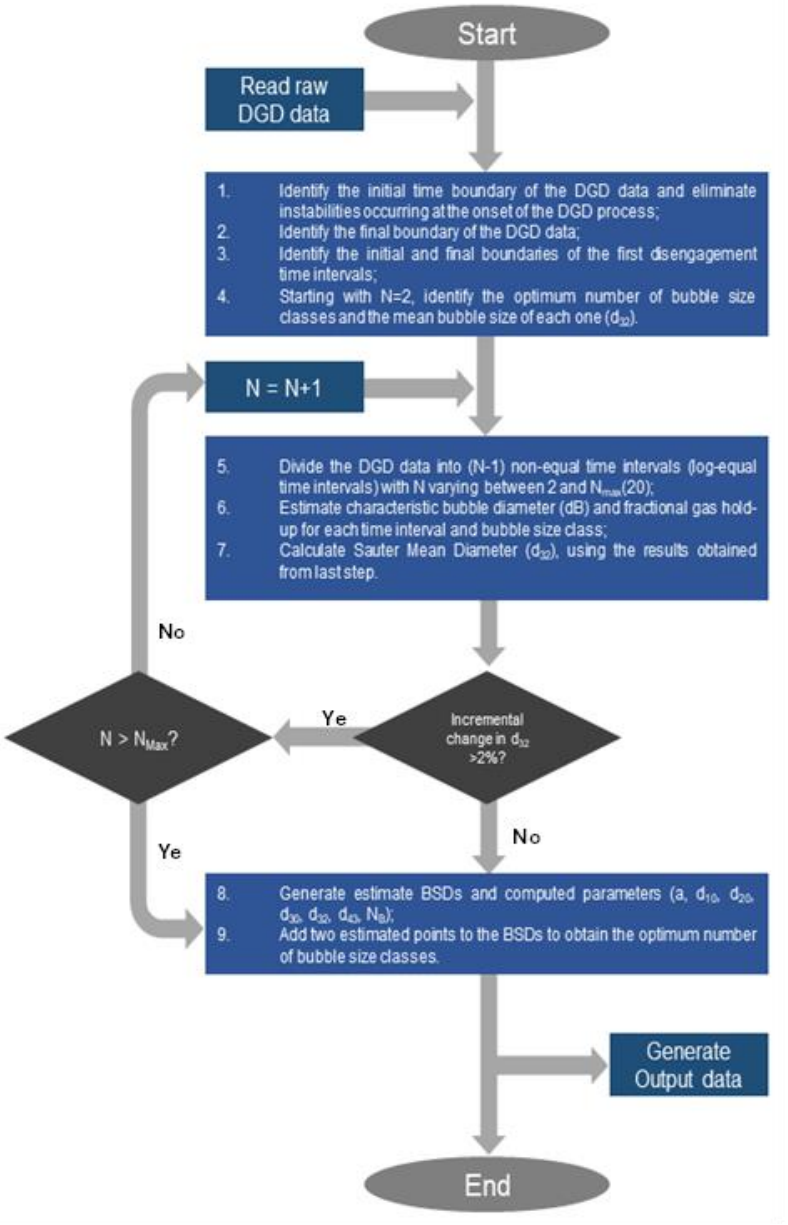

Figure 2.8. Diagram of the algorithm to process DGD data. Adapted from Leng et al. (2022).

2.3.7. Image Analysis

To verify the accuracy of the DGD methodology, the results obtained for some operating conditions under the continuous flow rate were processed using the DGD methodology and compared to the image analysis through image acquisition.

The images were obtained at a height of 400 mm above the sparger. Two 65 W and 7000 LM LED light sources were positioned and fixed outside on both sides of the reactor. Images were obtained using a pco.imaging high-speed camera, model pco.dimax S1, with a Nikkor Lens AF Micro-Nikkor 60mm f/2.8D lens. Images were acquired at a frequency of 1 Hz, with a shutter opening time of 1.5 μs. A matte black plate was fixed inside the column and positioned at a height of 400 mm from the sparger and 4 mm far from the inner wall of the column working as a background. This was necessary to provide samples of bubbles from the bubble swarm during the aeration process and provide some contrast between the border of the bubbles and the liquid medium for image acquisition.

The ImageJ open access software (1.53k, National Institutes of Health (NIH), Bethesda, MD, USA) was used to process the images obtained. Several pre-processing procedures were carried out, such as background subtraction and high delimitation of the surface of the bubbles so that the binary images obtained could be submitted to automatic analysis to obtain the diameter of the bubbles. The bubbles were approximated to the shape of ellipses and their equivalent diameters could be obtained by Eq. (2.4). The ImageJ software automatically provides the measurement of the major and minor axes of the bubbles, whose values were used to determine the equivalent diameter of the analyzed particles. Images were obtained in triplicate for each operating condition of flow rate and frequency. Each processed image allowed the analysis of an average of 150 bubbles.

$$d_i = \sqrt{\frac{\alpha^2}{A_R}} \tag{2.4}$$

Where, d_i is equivalent diameter of each bubble (mm); α is the major axis of the ellipse diameter (mm); A_R is the ratio of the major and minor diameters of each sphere considered as an ellipse.

The Sauter mean diameter value (d_{32}), defined as the mean diameter of a sample of bubbles weighted by the volume each bubble occupies in the dispersion, is calculated by Eq. (2.5).

$$d_{32} = \frac{\sum_{i=1}^{n} d_i^3}{\sum_{i=1}^{n} d_i^2} \tag{2.5}$$

2.4 Results

2.4.1 Dynamic Gas Disengagement Results for d_{32}

Two different sets of experiments were carried out to characterize the FBG system. These data sets can be seen in Table 2.1.

Table 2.1. Set of experiments.

Data Set	Sparger	Liquid Solution	Frequency	Gas Flow rate
1	H3 (orifices of 300 μm)	20 ppm (SDS)	20 to	10 to
2	H3 (orifices of 300 μm)	Tap Water	160 Hz	55 L min^{-1}

The system was operated under 132 different conditions regarding the frequency of the solenoid valve, gas flow rate, and composition of the liquid phase (coalescent and non-coalescent solutions). All the conditions were carried out in triplicate, gathering a total set of 396 runnings.

The frequency of operation of the high-frequency solenoid valve was varied from 20 to 160 Hz in intervals of 10 Hz. As it was mentioned before, the duty cycle of the solenoid valve ranged from 3 to 10%, to prevent the overheating of the device. It was observed during the experiments carried out at the laboratory that reaching higher gas flow rates required increasing the frequency of operation of the solenoid valve. Therefore, the results showed that not all gas flow rate values can be reached by all the frequencies of operation. Even though, there were regions among all the frequencies in which a decrease in bubbles diameter was reached, compared to the aeration using the continuous flow rate mode. The experimental data regarding the continuous aeration mode was also obtained for each data set depicted in Table 2.1, varying the gas flow rate from 10 to 60 L min^{-1}. This was mandatory to assess the efficiency of the FBG system in the process of decreasing the diameter of bubbles in comparison with the conventional aeration mode.

The experimental results obtained for the first set of data (20 ppm of SDS) were divided into three different graphs to provide a better visual assessment of the results. The first graph shown in Fig. 2.9 comprises the d_{32} obtained for the continuous gas flow rate and operating frequencies from 20 to 60 Hz of the solenoid valve. There is a clear tendency of decreasing the diameter of the bubbles generated by increasing both the gas flow rate and the operating frequency. For example, at a gas flow rate of 20 L min^{-1}, the bubbles generated by the FBG system operated at 50 Hz provided a decrease of 38% in d_{32} compared to the bubbles generated at a continuous gas flow rate. However, only the frequency of 60 Hz was able to reach gas flow rates higher than 27.5 L min^{-1} reaching a decrease of 28% at 32.5 L min^{-1} in bubble diameter.

It is worth mentioning an interesting fact regarding the number of classes of bubbles generated for the FBG system, using the DGD technique. Unlike other systems used to generate fines and microbubbles (Al Taweel et al., 2003), the FBG system generated only 2 classes of bubbles for all the experimental conditions performed. This fact indicates an application field of the FBG system in processes that require an even bubble-size distribution, such as the flotation process and some biotechnological applications. The inner geometry of the sparger coupled with the pulsed gas flow rate played an important role in the even distribution of the gas among the orifices of the sparger, which corroborates the assumptions regarding the use of pulsed gas flow rate for conventional spargers to obtain smaller bubbles compared to the conventional aeration process (continuous mode). Moreover, one last fact that calls our attention is the decrease in the standard deviation of the measurements as the gas flow rate increases. This is related to the noise generated by the pressure transducer signals, which are amplified at lower hold-ups caused by the lower gas flow rates.

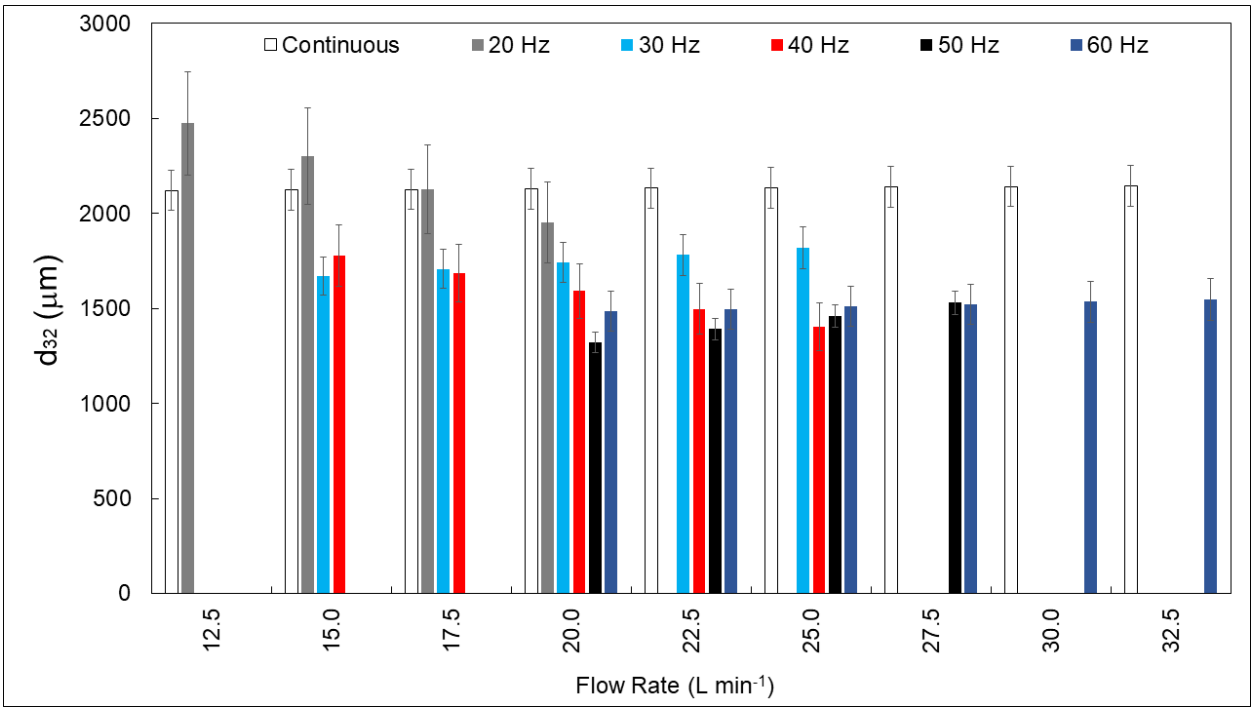

Figure 2.9. Results of d_{32} obtained for the first set of experiments ranging the frequency from 20 to 60 Hz as a function of the gas flow rate (L min^{-1}).

The second group of experimental results comprises frequencies ranging from 70 to 110 Hz, as shown in Fig. 2.10. The tendency of requiring higher frequencies to reach higher gas flow rates remains for this range of operating frequencies, which can be observed in the last two experimental gas flow rates (30 and 32.5 L min^{-1}). However, different from the first range of frequencies depicted in Fig. 2.9, the decrease in the d_{32} value compared to the continuous gas flow rate was about 35% for virtually all experimental conditions.

The FBG system, as mentioned before, is comprised of the high-frequency solenoid valve, the PWM module, the sparger, and the liquid solution. Summarizing, each set of conditions shown in Table 2.1 represents a different FBG system. Thus, the behavior observed in Fig. 2.10 may be indicating a bright spot of operation for this system specifically, ranging around 100 Hz. The hypothesis of an optimum range of operation can be corroborated by the third group of experimental results as shown in Fig. 2.11, which ranged the frequencies from 120 to 160 Hz.

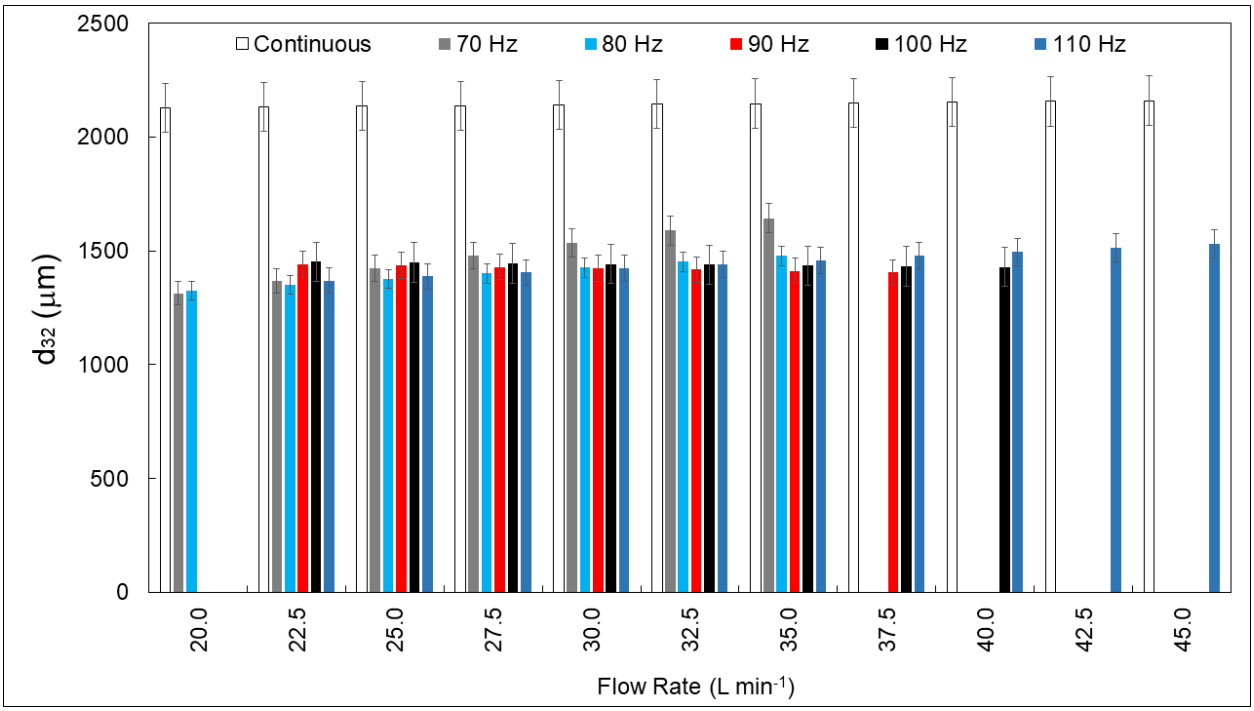

Figure 2.10. Results of d_{32} obtained for the first set of experiments ranging the frequency from 70 to 110 Hz as a function of the gas flow rate (L min^{-1}).

The tendency of the last two graphs is followed by the third one, reaching the highest gas flow rate with the highest frequency of 160 Hz. It is also interesting to notice there is a systematic decrease in the difference between the d_{32} values of bubbles generated under pulsed and continuous operation modes as the gas flow rate increases. The decrease in the d_{32} of 33% at 30 L min^{-1} and 120 Hz is virtually the same value reached by all the frequencies from 70 to 110 Hz in Fig. 2.10. However, at 55 L min^{-1} and 150 or 160 Hz, the d_{32} is just 12% lower than the one generated by the continuous gas flow rate regime. This indicates there may be an optimum range of frequency (70 to 120 Hz) and gas flow rate (25 to 30 L min^{-1}) for the operating conditions regarding the set of data assessed. The system may require a more hydrophilic material to operate at higher gas flow rates, i.e., higher gas velocities at the orifices, which would enhance the effect of momentum forces compared to surface tension, allowing bubbles to detach from the orifices at smaller sizes. This means that at some point, the material of the sparger and the characteristics of the liquid phase play a more important role in the early detachment of the bubble than the frequency of the valve does. This is the reason why studies were reported regarding the chemical treatment of the sparger's material (Calverley et al., 2020a). The evidence of a bright spot of

operating conditions was also stated by other authors previously (Brittle et al., 2015b), but never done for a pilot scale system operating with a conventional sparger.

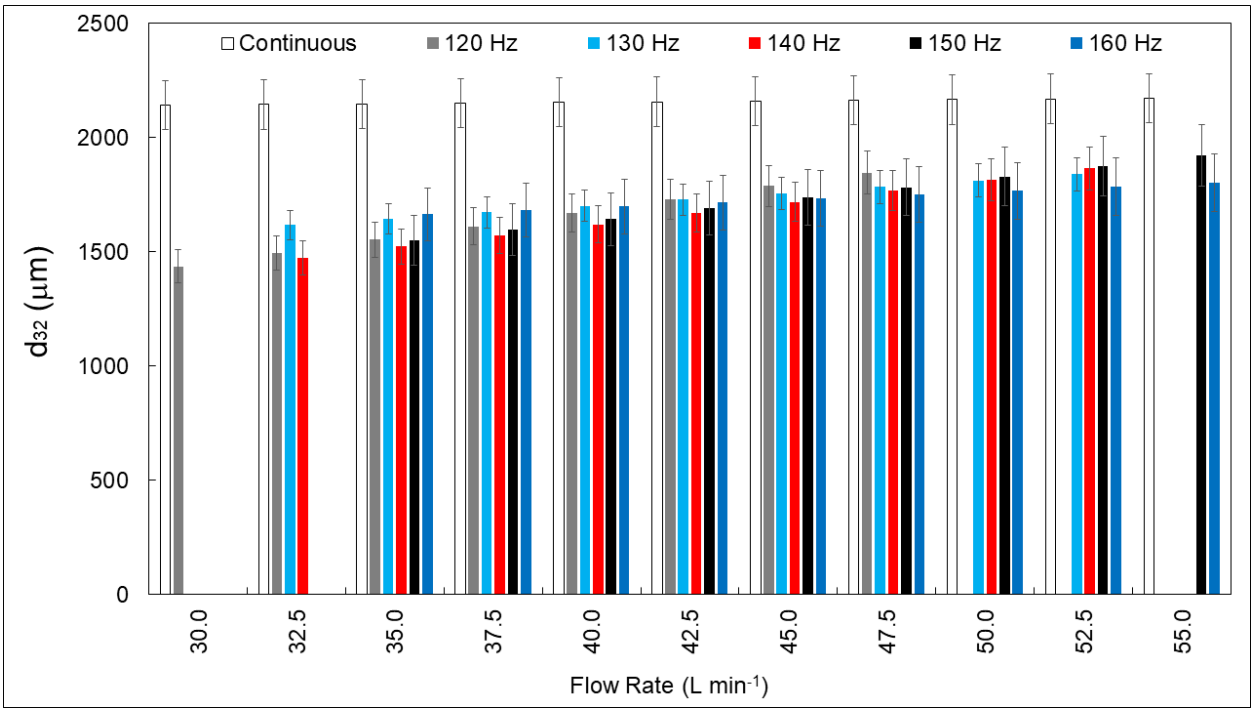

Figure 2.11. Results of d_{32} obtained for the first set of experiments ranging the frequency from 120 to 160 Hz as a function of the gas flow rate (L min^{-1}).

Fig. 2.12 shows the results of gas hold-up (ε) at the steady state for the operational conditions assessed in Figs. 2.9 to 2.11. As it was expected, the smaller the bubbles, the higher the gas hold-up, since its buoyancy force is smaller. However, the gas hold-up results appear to be less sensitive in identifying the reduction in bubble diameter, as they start to exhibit this reduction only from the operation at a frequency of 100 Hz and in the range of 35 to 40 L min^{-1}. This outcome merely corroborates the hypothesis that for this system under study, frequencies around or greater than 100 Hz are the most effective in achieving the reduction of bubble diameter.

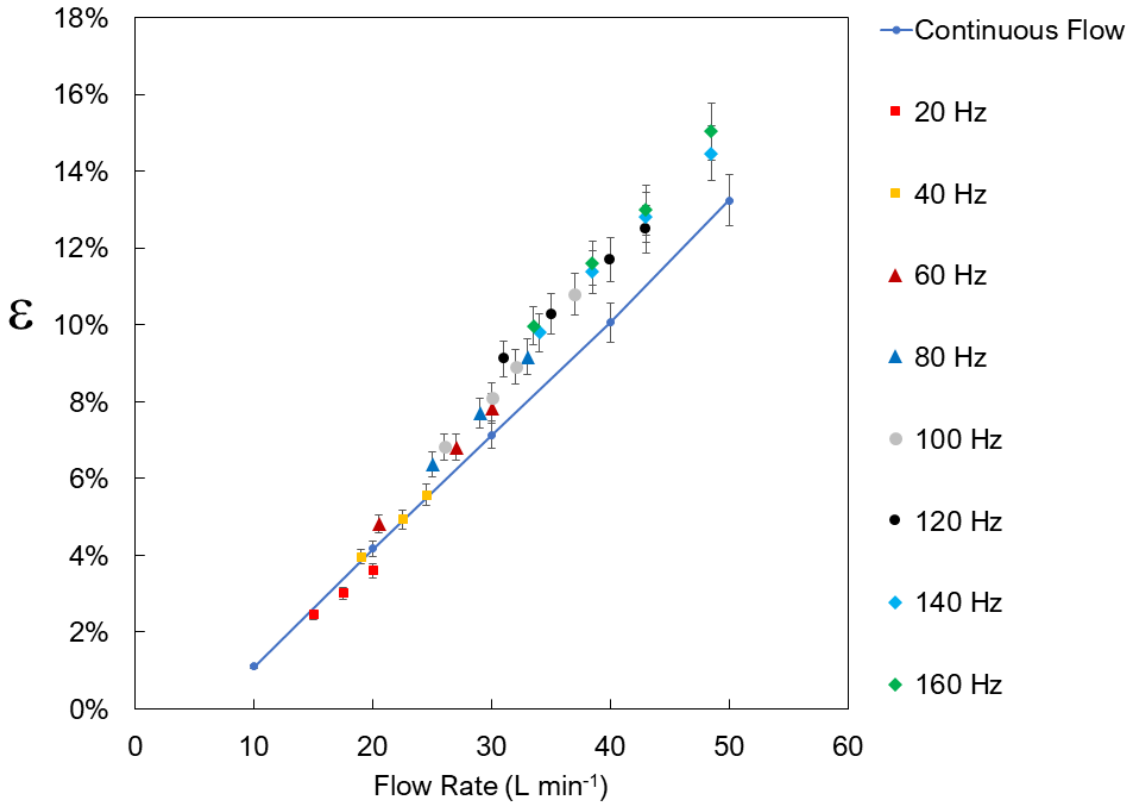

Figure 2.12. Gas hold-up (ε) results for the operation conditions of the first set of experiments.

The results depicted in Fig. 2.13 represent the d_{32} reached for each frequency of operation for the gas flow rates ranging from 15 to 50 L min^{-1} using tap water as liquid solution (second set of operation conditions shown in Table 2.1). Differently from the experiments carried out in the contaminated liquid solution (20 ppm of SDS), all the conditions of pulsed gas flow rate generated bigger bubbles than the ones formed using conventional aeration process (continuous gas flow rate). These results are corroborated by previous studies which point the importance of contaminated solutions in the generation of fine and microbubbles (Al Taweel et al., 2013b). Moreover, the results presented in Fig. 2.13 also confirm the significance of the sparger material and the liquid solution characteristics, as the phenomenon seemingly governing the delayed detachment of bubbles from the sparger orifices is conjunction (Tesař, 2014). The bubbles appear to lack sufficient energy for premature detachment, remaining anchored to the sparger material until they reach a sufficient volume to break free from the orifices.

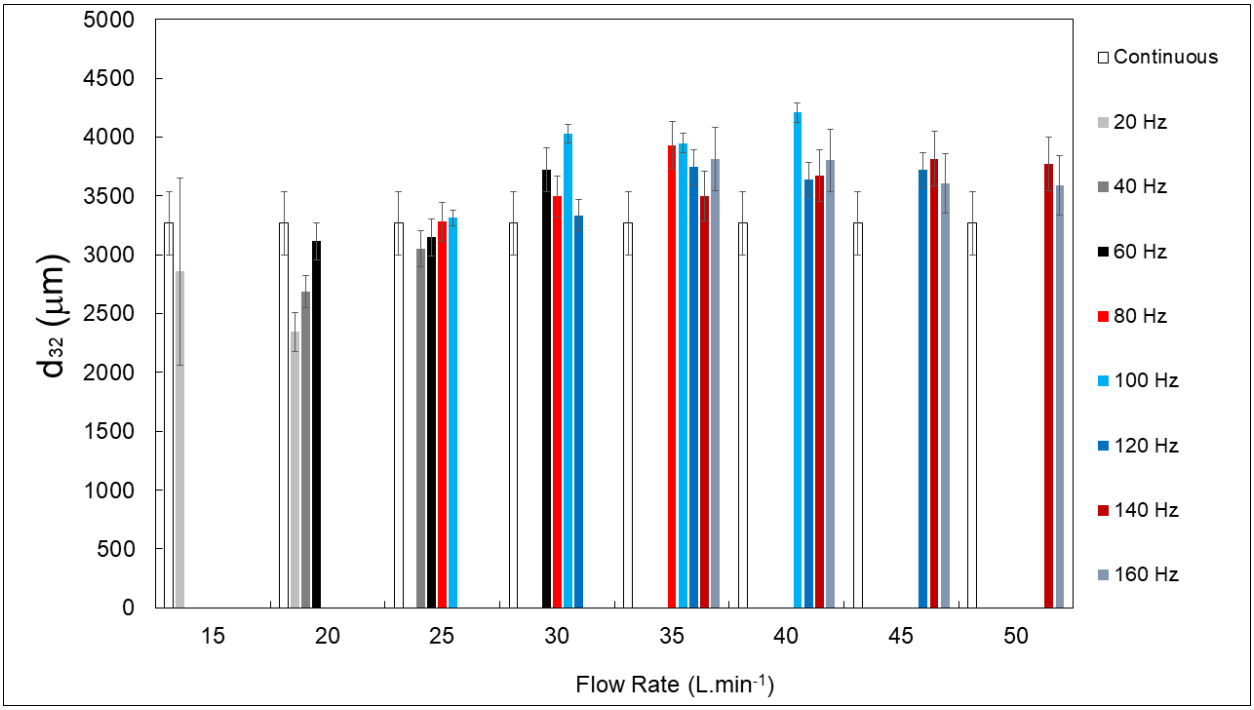

Figure 2.13. Results of d_{32} obtained for the second set of experiments (tap water) ranging the frequency from 20 to 160 Hz as a function of the gas flow rate (L min-1).

2.4.2 Image Analysis

As mentioned before in Section 2.3.7, images of the bubbles were captured to provide criteria for assessing the accuracy of the DGD methodology. A sample of images can be seen in Fig. 2.14, which refers to gas flow rates of (a) 20 and (b) 60 L min^{-1}. The liquid solution used for image acquisition was 20 ppm of SDS in tap water, and the flow regime was the continuous gas flow rate ranges from 20 to 100 L min^{-1}. The results obtained by the image analysis were compared with the ones obtained by the DGD methodology. The assessment of the bubble diameter through image analysis was performed always in triplicates using the software open-source ImageJ, and an average of 150 bubbles were analysed in each picture.

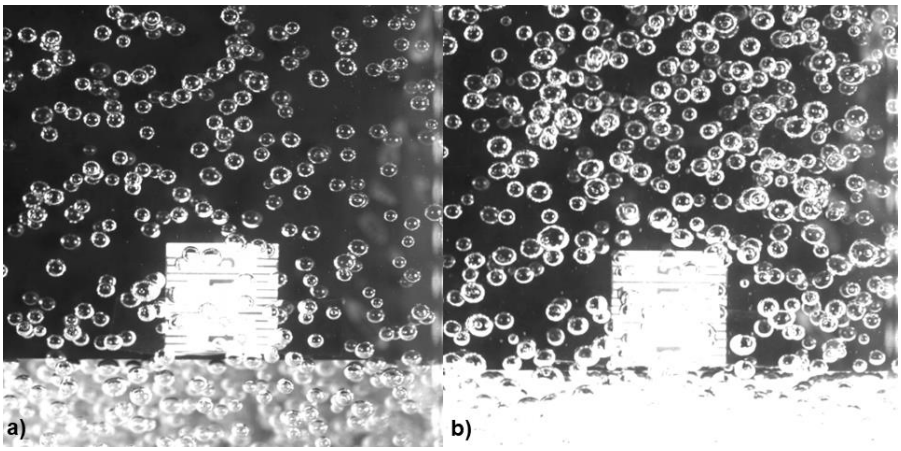

Figure 2.14. Image acquisition of the bubbles under continuous gas flow rate: (a) 20 and (b) 60 L min^{-1}.

The difference between the results of d_{32} using the DGD methodology and the image acquisition was below 10% for all the gas flow rates of gas operated, which indicates the data obtained for the 396 experiments can be reliable to characterize the FBG system in a pilot scale operation. The data comparing both sets of data is depicted in Fig. 2.15.

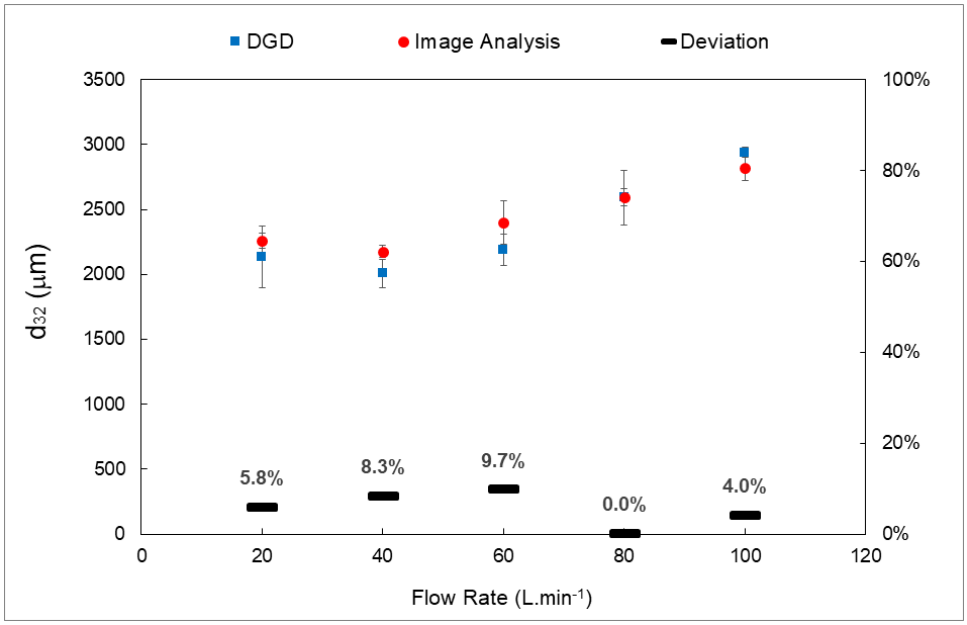

Figure 2.15. Comparison between the DGD and Image Acquisition methodologies to determine the diameter of bubbles generated (d_{32}).

2.5 Conclusions

One of the hypotheses raised at the beginning of the studies regarding the pulsed gas flow as a factor of decreasing the generated bubbles has been proven to be true in a pilot scale. The FBG system is comprised of the solenoid valve, the module PWM, the sparger, and the liquid medium in which the bubbles are generated. The effects of pressure due to the liquid column also affect the operation of the system. Thus, the first set of data processed regarding the experiments carried out showed reliable and promising results since the pulsed gas flow rate was able to decrease the diameter of the bubbles by almost 40% in comparison to the conventional aeration process. Moreover, the gas flow rate and the operating frequency have strongly affected the diameter of the bubble formed, indicating there may be an optimum region of operation depending on the FBG system. For the first data set employing 20-ppm SDS solution this region seems to be at the gas flow rate of 25 to 30 L min^{-1} and ranges between the frequencies from 70 to 120 Hz. It was also evident that for higher gas flow rates, it is mandatory to gradually also increase the operating frequency. However, it was also noticeable the importance the material of the sparger and the characteristics of the liquid solution play in the detachment of the bubbles, specially for higher flow rates. None condition of frequency operation was able to generate smaller bubbles than the ones generated under continuous gas flow rate using just tap water.

Such evidence corroborates the claims for devices that generate pulsed gas flow with some versatility, to be quickly tuned in terms of frequency and gas flow rates as the operating conditions change, but also the need of choosing the right material to build the sparger. It is evident that depending on the bioprocess which the fine bubbles will be used (liquid solution and gas flow rate) a customized set of operation conditions as frequency and sparger material will be required. This fact brings up the advantages of the high-frequency solenoid valves compared to the shortcomings of fluidic oscillators without moving parts and qualifies the FBG system to be applied on a pilot/industrial scale to decrease the diameter of the bubbles generated. Furthermore, the generation of only two classes of bubble diameter, which was determined by the DGD technique, makes this technology also available for processes that require more uniformity of the bubbles generated than the extremely small bubbles.

Chapter 3

Fine and Microbubbles in Oxygen Transfer

3.1 Introduction

The processes of oxygen or CO_2 transfer from the gas phase to the liquid phase are of significant importance for the industrial sector and various segments of the agro-industry. Proper gas delivery to the liquid medium, which will provide for the metabolic needs of microorganisms, is a key factor in the success of a bioprocess designed for the production of specific bioproducts (Zimmerman, et al., 2009). Hence, gas transfer to the liquid phase, specifically oxygen and CO_2 (Al-Mashhadani et al., 2012), has been a vital area of study to enable the bench, pilot, and industrial scales production of various bioprocesses. One of the focal points of these studies is the reduction of bubble diameters generated by spargers (Al-Mashhadani et al., 2012; AL-Mashhadani et al., 2015), as the interfacial area of the bubbles plays a critical role in mass transfer operations between phases in bioreactors.

Pulsed gas generation systems have proven effective in producing smaller bubbles through spargers (Tesař et al., 2006). Fluidic oscillators, for instance, have found application in diverse reaction systems and demonstrated efficacy in generating microbubbles, often utilizing porous or sintered spargers (Zimmerman, et al., 2011). On the other hand, the pulsed flow system using a high-frequency solenoid valve has received limited exploration thus far, with existing studies concentrating on generating microbubbles and employing porous spargers, which inherently produce considerably smaller bubbles (Song et al., 2021). The initial investigation of this system with conventional spargers on a pilot scale was undertaken and presented in Chapter 2 of this work.

Since the pulsed gas flow system, the subject of this study, has been tested and validated at a pilot scale under various operational conditions and evaluated in terms of bubble diameter reduction, this current chapter aims to scrutinize and assess the system at a bench scale concerning the oxygen volumetric mass transfer coefficient ($k_L a$) in aeration operations. Two types of spargers, one with conventional perforations and the other utilizing a sintered plate, were employed in both coalescent and non-coalescent systems. The results demonstrated a congruence between the achieved reductions in bubble diameter from Chapter 2 and the subsequent increases in $k_L a$ values. Nonetheless, the study underscores that the choice of sparger type and the liquid medium are pivotal factors influencing the effectiveness of the pulsed gas flow system in reducing bubble diameter. Thus, each process demands a customized solution, reinforcing the conclusions drawn in the preceding chapter of this work.

3.2 Objective

To assess the effectiveness of the pulsed gas flow system in increasing $k_L a$ values in oxygen transfer operations within coalescent and non-coalescent liquid media, using spargers that generate fine bubbles (R8H) and spargers that generate microbubbles (SSD).

3.3 Materials and Methods

3.3.1 The Setup

The experiments for determining the oxygen volumetric mass transfer coefficient ($k_L a$) were conducted in a bubble column reactor with a square cross-section and a useful volume of 10 L, composed of five connected modules, fabricated from polycarbonate with dimensions of 14 cm per side and 13.5 cm in height. The reactor features a lid with various connections, which were utilized for the attachment of the dissolved oxygen sensor and the measurement of gas flow rate. Due to the inherent difficulty in precisely measuring the pulsed gas flow at the reactor inlet, the decision was made to measure the air flow rate at the reactor outlet to obtain a reliable flow value for the purpose of performance comparison between pulsed and continuous flow conditions. The measurement of the air outlet flow rate was carried out using a GFC 17 digital mass flowmeter (Aalborg, Denmark).

Two types of spargers were fabricated for the oxygen transfer experiments: an 8-arm rosette sparger (R8H) and a sintered stainless-steel disc (SSD). The R8H sparger consists of eight perforated arms made from polyacetal, each containing 34 holes with a diameter of 0.3 mm (300 μm), totaling 272 holes. The SSD sparger is characterized by a sintered stainless-steel plate with a diameter of 10 cm, a thickness of 3.0 mm, and 5.0 μm pores, coupled with a circular aluminum base. The SSD sparger was designed to replicate configurations used in literature for microbubble formation (Desai et al. 2018; Hanotu et al. 2013; Hanotu, Bandulasena, and Zimmerman 2012; Hanotu et al. 2017, 2016; Mahmood et al. 2015; Zimmerman et al. 2008, 2011; Zimmerman, Hewakandamby, et al. 2009; Zimmerman, Tesař, et al. 2009), which employed porous materials with pores in the range of tens or units of micrometers.

The spargers can be observed in Fig. 3.1. Both have identical dimensions for air inlet connections, enabling them to be fixed in the same position on the reactor base. It is noteworthy that the SSD sparger contains an internal gas distributor made from polyacetal, responsible for evenly distributing the gas flow across its outlet surface. In addition to directing the gas flow from

internal ducts, these distributors reduced the empty volume of the air chamber (the space between the porous element and the sparger base). The gap between these two surfaces was reduced from 15 mm to approximately 1.0 mm distance.

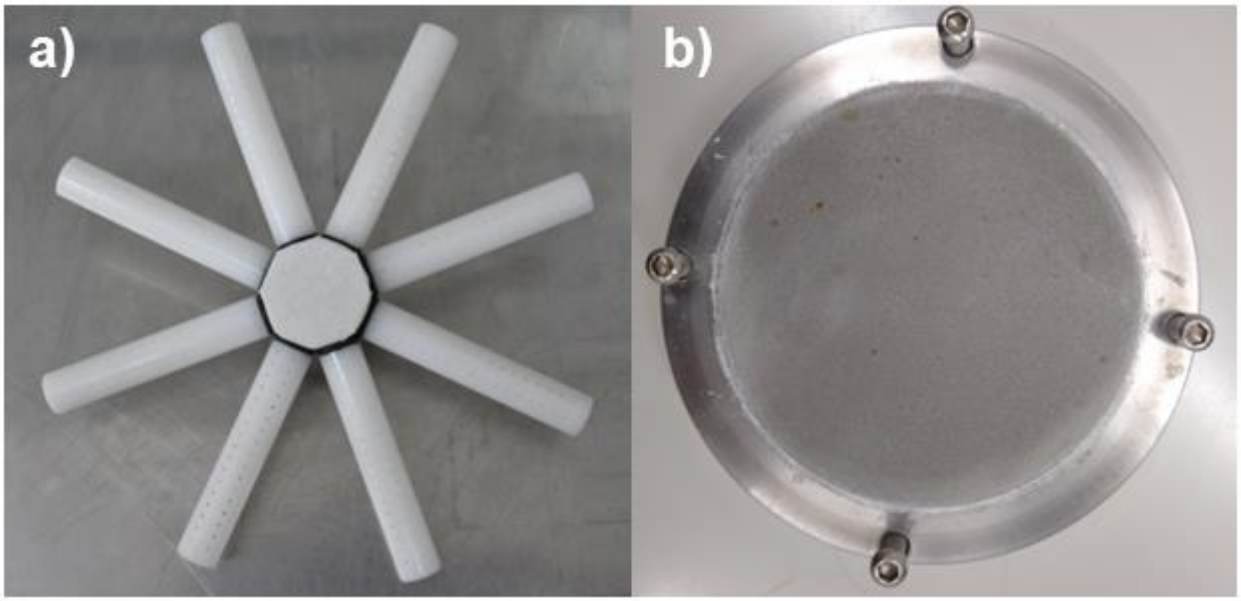

Figure 3.1. Spargers used for oxygen mass transfer experiments: (a) R8H and (b) SSD.

Dissolved oxygen measurements were conducted using an InPro 6800 polarographic electrode (Mettler Toledo), with data collected by the O_2 Transmitter 4500 (Mettler Toledo, Switzerland) transmitter. An adaptation of the system was required to remove microbubbles that became trapped at the electrode tip, affecting the dissolved oxygen measurements. A Watson Marlow 323-Dz peristaltic pump (United Kingdom) was installed to recirculate water from the reactor, with its discharge directed toward the electrode tip to remove the bubbles that became trapped during the assay. The pump rotation speed and the position of the water jet relative to the electrode were maintained constant for all experiments. The experimental setup for determining $k_L a$ under different operational conditions is illustrated in Fig. 3.2. The pressure inside the reactor was monitored and considered in the $k_L a$ calculations. It is also worth mentioning that gas flow rate control should be managed by adjusting the valve's duty cycle, rather than using a mass flow controller before the sparger, as the latter would eliminate the pulsed gas flow effect and, consequently, reduce the momentum force required to detach bubbles.

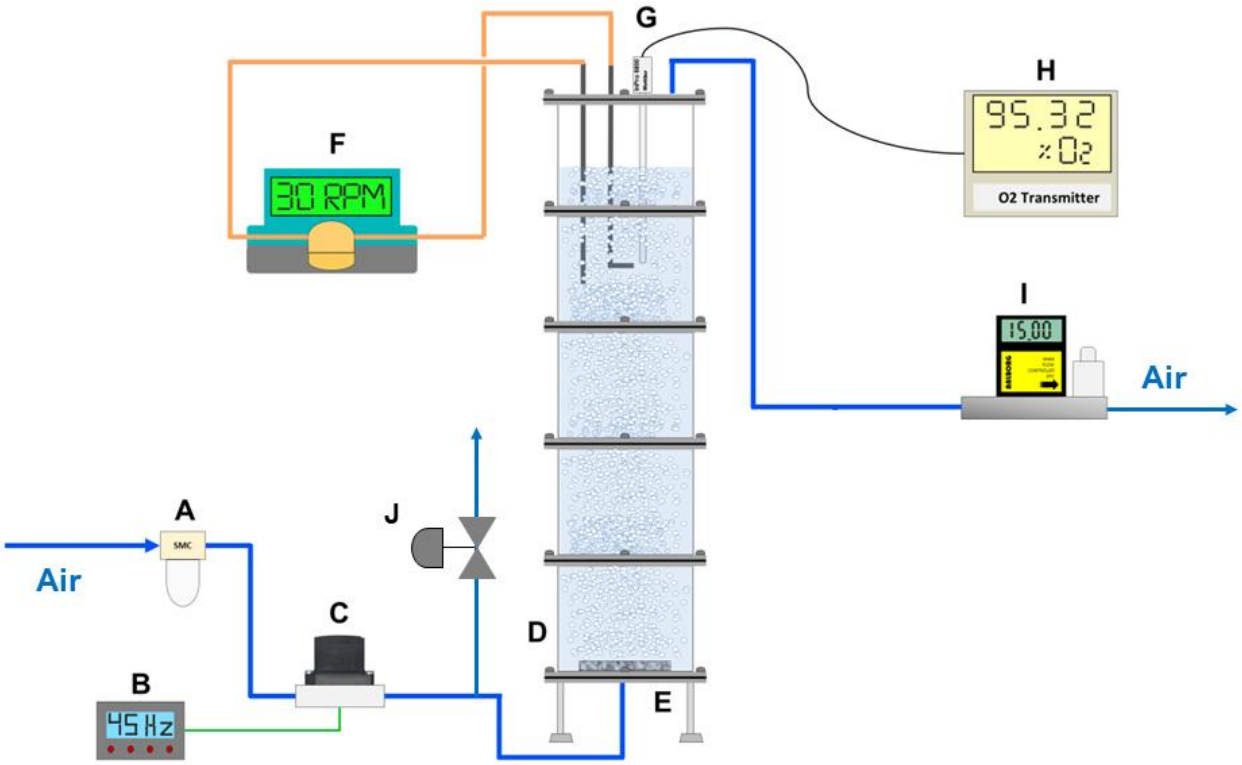

Figure 3.2. System Setup. (A) Air filter, (B) PWM module, (C) solenoid valve, (D) 10 L reactor, (E) sparger, (F) peristaltic pump for medium recirculation, (G) dissolved O_2 sensor, (H) dissolved O_2 transmitter, (I) mass flowmeter; (J) purge valve for flow rate control.

3.3.2 Experimental Conditions

The valve used for generating the pulsed gas flow was a SMC (Japan) brand, model SX11F-AG, with a power of 80W, a maximum gas volumetric flow capacity of 50 L min^{-1}, and a maximum operating frequency of 1200 Hz. The valve control was achieved through a 150 KHz PWM signal generator module, varying the valve's operating frequency from 10 to 425 Hz and adjusting the duty cycle between 2 and 20% to achieve the desired gas flow rate in the experiment. Compressed air from a compressor was used, with the line pressure adjusted to 3.5 bars at the valve inlet. The air flow rate used in the experiments ranged from 1 to 10 L min^{-1}, controlled by the opening of a purge valve just before the air inlet in the sparger. The reactor operating volume was 10 L of distilled water and then aqueous solution of Na_2SO_4 0.05 M.

3.3.3 Dynamic Method: $k_L a$ Determination

The dynamic method was employed for the determination of $k_L a$, which involves using a nitrogen gas stream to remove all dissolved oxygen from the liquid medium. Once a dissolved oxygen concentration close to zero was achieved in the liquid, aeration of the medium under the desired operating conditions was initiated. Aeration was then ceased upon reaching around 90% of liquid phase saturation. Each operating condition (frequency and flow rate) was conducted in triplicate.

To determine the value of the volumetric oxygen mass transfer coefficient ($k_L a$), the adjustment of Eq. (3.1), as described by Cerri et al. (2016) , was performed on the experimental dissolved oxygen tension values. The minimization of the sum of squared residuals was employed as the objective function by adjusting the value of $k_L a$.

$$DOT_e = DOT_{e0} e^{-k_e(t-t_0)} + 100\left[1 - e^{-k_e(t-t_0)}\right] + \frac{k_e}{k_e - k_L a}(DOT_0 - 100)\left[e^{-k_L a(t-t_0)} - e^{-k_e(t-t_0)}\right] \quad (3.1)$$

Where, DOT_{e0} is the dissolved oxygen tension at $t = t_0$ measured by the sensor (%), DOT_0 is the real dissolved oxygen tension at $t = t_0$ (%), k_e is the electrode sensitivity considered equal to 0.15 s^{-1} for the experimental conditions performed, t_0 is the initial time of the experiment (s).

3.4 Results

3.4.1 Oxygen Mass Transfer: Distilled Water

The results of $k_L a$ for different flow rates and frequencies using the R8H and SSD spargers in distilled water are presented in Figs. 3.3 and 3.4, respectively. It is evident that the R8H sparger exhibited a more favorable range of operation, falling within 100 to 150 Hz. This observation aligns with the earlier findings concerning the reduction in bubble diameter achieved at the pilot scale, as detailed in Chapter 2. With a consistent gas flow rate, an increase in $k_L a$ values is expected as the bubble diameter decreases. This expectation arises from the fact that the term "a" in the volumetric mass transfer coefficient is determined based on the overall surface area available for mass transfer. In the case of a constant gas flow rate, smaller bubbles correspond to a greater total number, resulting in an increased total area available for mass transfer. Furthermore, it can be

observed that the percentage increase in $k_L a$ for the frequency of 150 Hz in comparison to the continuous flow rate drops from 88% at 1.0 L min^{-1} to 12% at 10 L min^{-1}, also corroborating the lower difference in bubble diameter for higher flow rates of gas as demonstrated in pilot scale. It is also important to notice that higher frequencies (300 Hz, as an example) do not contribute for the decrease in bubble diameter and consequently an increase in $k_L a$ values. On the contrary, higher frequencies seem to leverage the effect of the conjunctions at the detachment of the bubbles (Tesař, 2014).

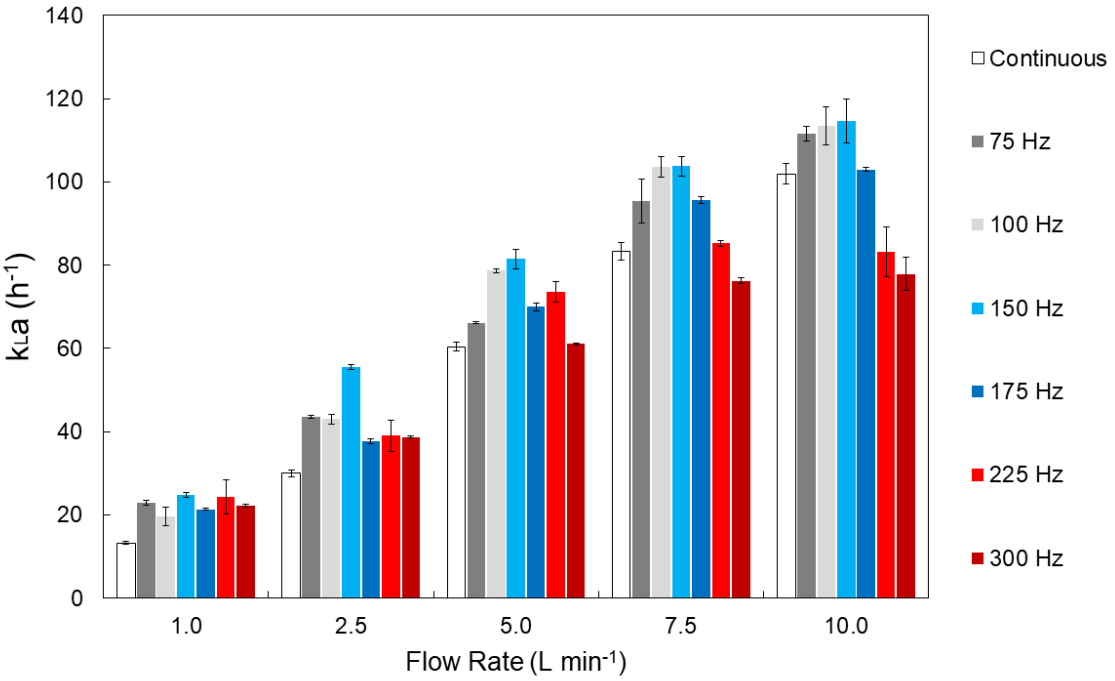

Figure 3.3. $k_L a$ values obtained for the R8H sparger in distilled water.

However, upon analyzing the results obtained for the SSD sparger (Fig. 3.4), it is not possible to discern any difference between the coefficients obtained for the continuous flow rate and those obtained for different frequencies. This intriguing result can be explained relying on the diameter of the pores in the SSD sparger. The SSD sparger is a sintered stainless-steel disc comprised by pores of 5 µm. Numerous studies (Zimmerman et al., 2008; 2009) have highlighted that bubbles naturally form under a characteristic frequency of generation, primarily influenced by the diameter of the orifice through which the gas flows. Considering bubbles under continuous flow rate are expected to detach from the orifice at 10 times its diameter, it results in bubbles of

50 μm for the SSD sparger. This indicates that may the frequency of 425 Hz was not enough to overcome the natural frequency of the bubble's formation for this sparger. Nevertheless, other aspects as the material of the sparger and its thickness also can hinder the effect of the increase in momentum force generated by the pulsed gas flow (Calverley et al., 2020).

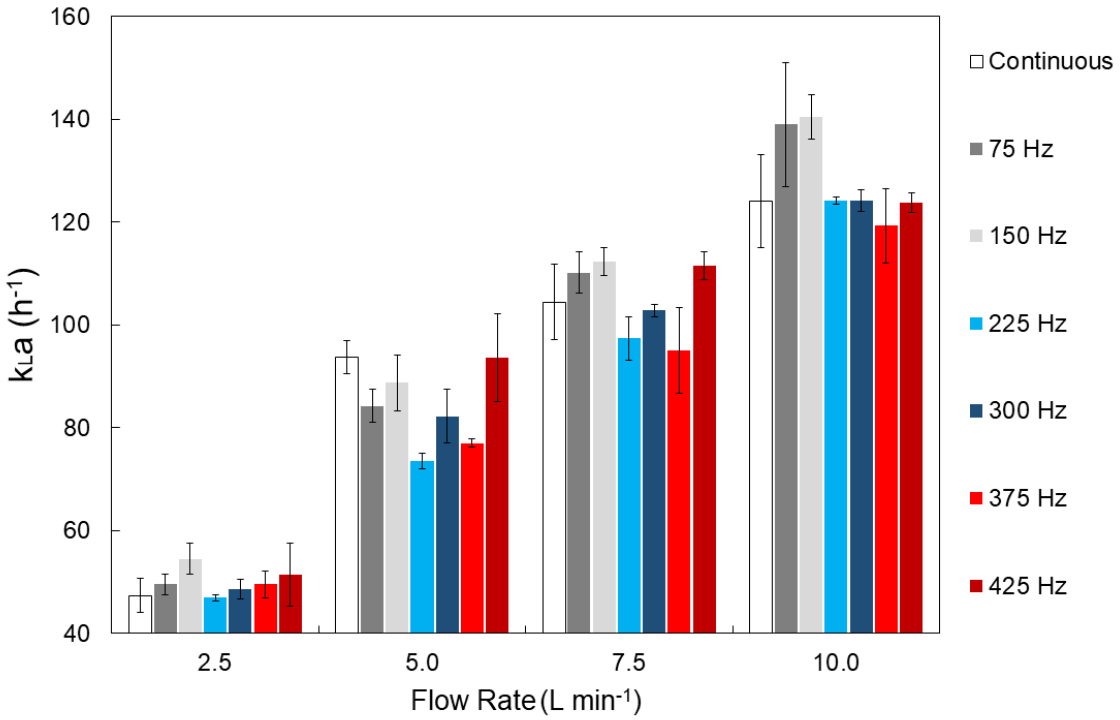

Figure 3.4. $k_L a$ values obtained for the SSD sparger in distilled water.

3.4.2 Oxygen Mass Transfer: Presence of Contaminants (Na_2SO_4)

Figs. 3.5 and 3.6 show the results of k_La obtained using the R8H and SSD spargers in Na_2SO_4 solution, respectively. It is noticeable that the oxygen volumetric mass transfer coefficient was higher in all situations compared to the system with pure distilled water. The continuous flow rate for example, at 10 L min^{-1} (ϕ=1 vvm) reached k_La values of around 100 and 125 h^{-1} in distilled water for the R8H and SSD sparges, while the values of 120 and 210 h^{-1} were achieved for the same spargers in Na_2SO_4 solution, respectively. The percentual increase of 68% for the SSD sparger were much higher than the 20% of increase for the R8H sparger. It means that the solution composition had a positive effect regarding the detachment of bubbles maybe due to the material of the SSD sparger, which seems to be more hydrophilic.

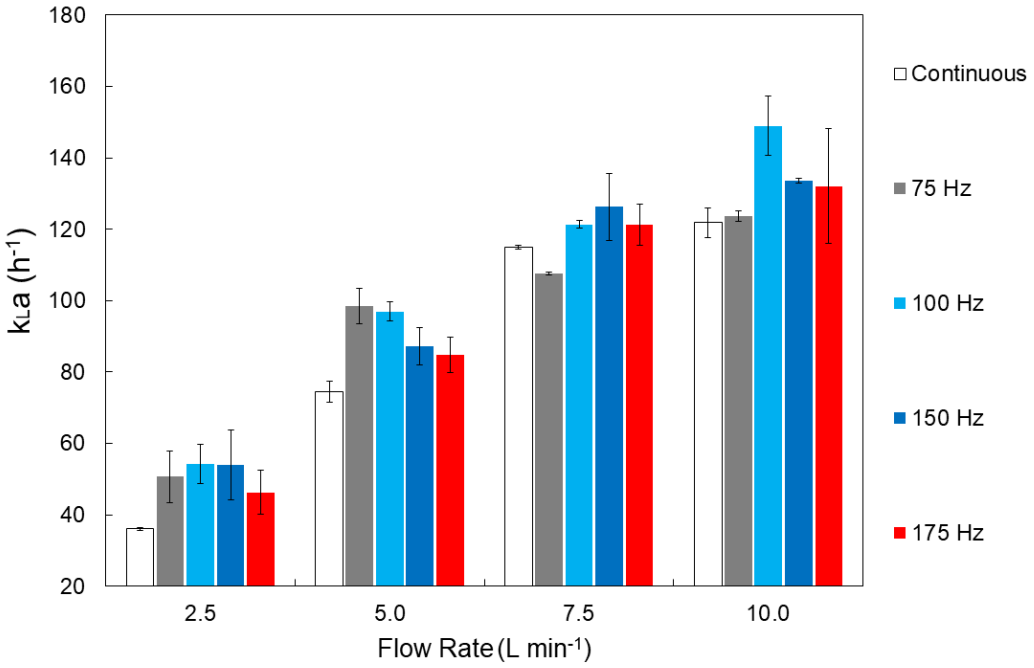

Figure 3.5. $k_L a$ values obtained for the R8H sparger in Na_2SO_4 solution (0.05 M).

The percentual increase in the mass transfer coefficient shown in Fig. 3.5 for the pulsed gas flow compared to the continuous flow rate is not so evident as it was in the distilled water system. Frequencies of 100 and 150 Hz remains being more positive than the others. The percentual difference of the $k_L a$ values obtained ranged from 53 to 23% from 2.5 to 10 L min^{-1}, i.e., slightly lower than the one obtained in the system operating with distilled water. Nevertheless, the behaviour of the system remained in accordance with the previous system. However, it seems that the non-coalescent solution leverages the continuous flow rate, which makes the effect of the pulsed gas flow less pronounced for this system.

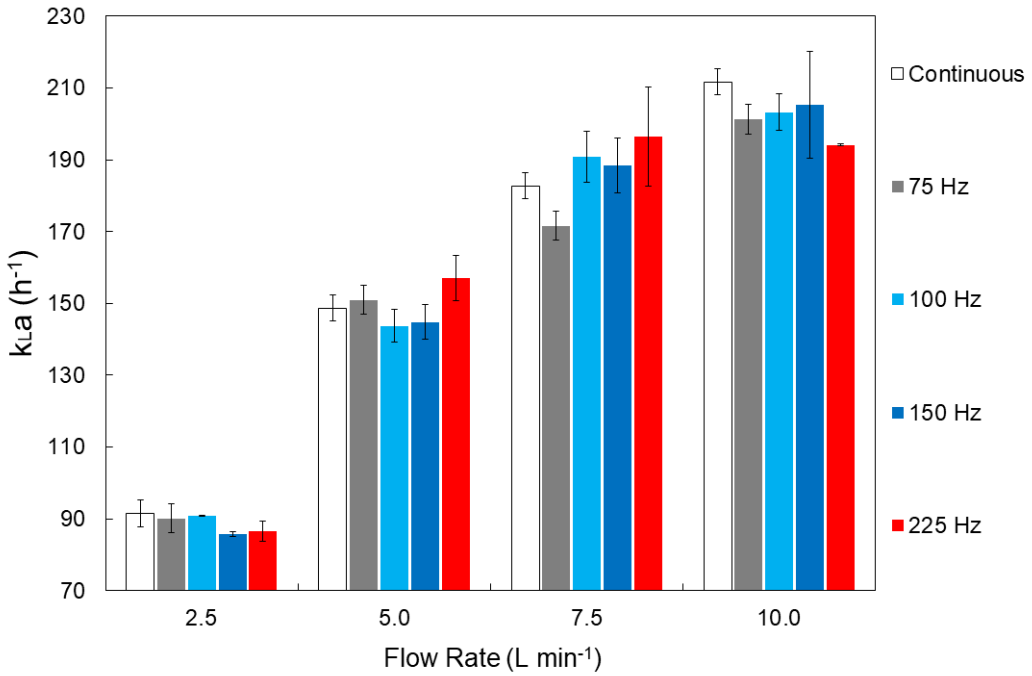

Figure 3.6. $k_L a$ values obtained for the SSD sparger in Na_2SO_4 solution (0.05 M).

For the results of the SSD sparger, shown in Fig 3.6, as already seen in the system of distilled water, there was no difference between the results obtained at continuous and pulsed gas flow rates. The reason for those results for the SSD sparger remains the same, based on the natural frequency of detachment of the bubbles.

3.5 Conclusions

Oxygen transfer emerges as one of the key processes that can benefit from the generation of smaller-sized bubbles, as it relies on the total bubble surface area available for mass transfer between the gas and liquid phases. The impact of this variable becomes evident when comparing the absolute $k_L a$ values achieved by the R8H and SSD spargers. Microbubbles generated by the SSD sparger, regardless of the liquid medium used, facilitate oxygen transfer up to 5 times faster than that achieved by fine bubbles. However, when analyzing the effect of reducing the diameter of microbubbles and fine bubbles using the pulsed gas flow system through $k_L a$ determination in the various studied setups, it was observed that the system is only effective for the fine bubble system generated by the R8H sparger.

It is believed that there is a natural frequency of bubble generation with a continuous gas flow rate, dependent on the diameter of the orifices through which the gas is passing. This natural frequency of bubble formation is higher for the SSD sparger, which has pores of 5 μm in diameter compared to the R8H sparger (300 μm). Thus, for there to be any effect of reducing the bubble diameter using pulsed flow, the valve's operating frequency must necessarily be higher than the natural frequency of bubble formation for each sparger. Therefore, we believe that frequencies in the range of 100 to 150 Hz are sufficient for reducing the diameter of bubbles generated by the R8H sparger, as evidenced by the increased $k_L a$ values within this operating range. On the other hand, frequencies above 400 Hz were not sufficient to observe the same effect for the SSD sparger.

The composition of the liquid medium also proved to be significant in increasing the $k_L a$ value overall, across all operational conditions, including continuous gas flow. Thus, while the apparent trends of reduced bubble diameter generated by the R8H sparger were maintained, the presence of salts in the medium might have further increased the natural frequency of bubble formation for the SSD sparger. This could potentially diminish the effectiveness of the pulsed flow system even more for the SSD sparger.

This demonstrates that the pulsed flow system is effective in reducing bubble diameter and consequently increasing $k_L a$, but in conjunction with the appropriate sparger for each application. Considering operations at pilot and industrial scales, using porous spargers does not make sense due to numerous operational issues that can arise from them (maintenance, cleaning, clogging, operation). Therefore, the solution of pulsed gas flow should be paired with a suitable sparger for each specific application.

Chapter 4

Stripping Process: Mechanical and Thermodynamic Entrainments and the Role of Bubbles

4.1 Introduction

The processes to recover volatile compounds from fermentation broths have been widely studied especially for processes that generate high-value products. For the bioethanol industry in Brazil, the stripping process applied to recover the ethanol from the fermentation broth seems to be a process with many advantages (Almeida et al., 2021). More than recovering ethanol from the fermentation broth, the stripping process acts to decrease the inhibition effect they cause in the yeast which is performing the fermentation (Sonego et al., 2014b). This is one of the major obstacles to be overcome in the bioethanol industry in Brazil. The yeast suffers from the inhibition caused by the accumulation of ethanol during the fermentation process, a fact that reduces the productivity of the industrial unit. Thus, the stripping process can act to recover ethanol and consequently decrease the inhibition by-product and the broth temperature due to the vaporization of ethanol and water. The ethanol inhibition and the control of temperature have been important drawbacks of ethanol production in Brazil (Almeida et al., 2021).

Sonego et al. (2014, 2016) studied the modeling and assessed the experimental results of ethanol production operating the stripping with CO_2. The authors found a suitable specific flow rate of 2.5 vvm to operate the bioreactor and reached a production of ethanol around 33.0% higher than the conventional process. Besides the stripping process in the ethanol fermentation being carried out with CO_2 produced by yeasts as stripping gas, the cooling effect promoted by the stripping led to an advantageous energy balance of the fermentation unit. Not only for ethanol from sugarcane, but for ethanol produced at high temperatures by thermophilic bacteria as reported by Calverley et al. (2020), stripping has been successfully applied for preliminary tests using hydroalcoholic solutions. The authors reached values of ethanol recovery above the ones estimated by the thermodynamic equilibrium, as well reported by Abdulrazzaq et al. (2016), using microbubbles. Inert gas was also used by Ezeji et al. (2005) to recover butanol from a fermentation broth. The authors also reported using estimations that the gas phase would reach the saturation concentration of butanol during the experiments.

There are many important results about the advantages of the stripping process to recover volatile compounds. However, the study of the operational conditions to maximize the rate of stripping and selectivity of these compounds remains still unclear. Different studies reported concentrations of the volatile compounds in the gas phase above the equilibrium (Abdulrazzaq et al., 2016; Calverley et al., 2020, 2021), but do not evaluate the phenomena of the vaporization and

mechanical entrainments separately. This is an essential point for the science of the stripping process, which would bring to light the actual influence of the diameter of bubbles and the height of the liquid column (Rees-Zimmerman, 2021) rule in the process of stripping.

This work has the objective of evaluating the role of the diameter of bubbles in vaporization and mechanical entrainments. Here, the vaporization entrainments will be called thermodynamic entrainment, just to make the discussion easier to understand. It is well known that the phenomena we are discussing is the vaporization, however the term thermodynamic makes easier to the reader think about the thermodynamic equilibrium, which is the way the vaporization entrainment was calculated. Preliminary experiments were conducted to ensure the conditions under which bubble saturation occurs. A mathematical model was proposed to determine the contributions of thermodynamic and mechanical entrainment to the overall ethanol removal for each operational condition of the subsequent experiments. The obtained results were then evaluated in terms of total ethanol removal and selectivity for the scales of 1.0, 4.5, 8.0, and 50 L operation volumes using fine bubbles generated by a system of pulsed gas flow rate, and microbubbles generated using a sintered steel sparger. The parameters for evaluating ethanol removal were simpler and more straightforward compared to those found in the literature, as the main focus of the study was to separate and quantify the effects of thermodynamic and mechanical entrainment: how they can aid or hinder removal and ethanol concentration, and how liquid height, bubble diameter and operational scale influence the stripping process. The overcomes of this study is an essential point to assess the best operating condition of stripping for different processes.

4.2 Objective

Firstly, ensure the operational condition during the stripping operation where bubbles are saturated with ethanol and water. Then, model the removal of these components in the gas phase to separate and quantify the removal due to thermodynamic and mechanical entrainment, and evaluate the role of different bubble diameters in the stripping process.

4.3 Materials and Methods

4.3.1 Reactors and Spargers

The experiments were conducted in two different squared-face bubble column reactors of usable capacity of 10 and 50 L, built-in polycarbonate. The reactor of 10 L had side dimensions of

140x140 mm and its height could be arranged by mounting up five modules of 150 mm height each, as shown in Fig. 4.1 (a). The 10 L reactor was operated with two different spargers coupled at the base of the reactor, where the gas inlet is located. The 50 L reactor had dimensions of 240x240 cm on each side and a total height of 1000 mm, the latter being divided into two attached modules of 500 mm height each as can be seen in Figure 4.1 (b). The base of the reactor was composed of the sparger itself, also of a square face.

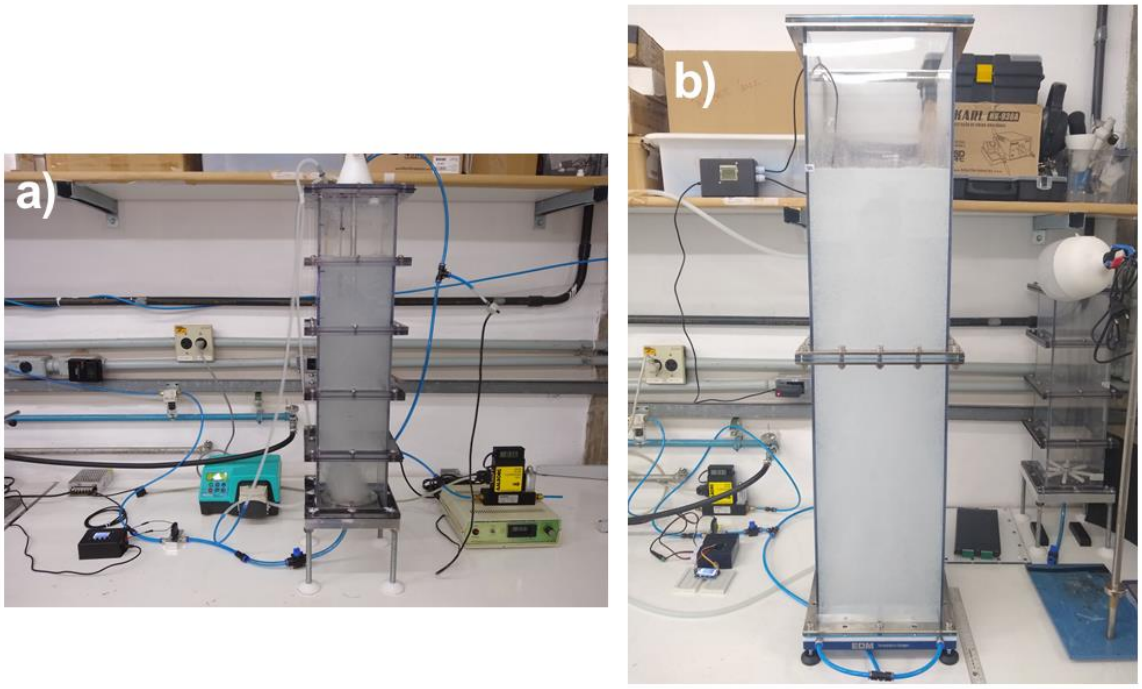

Figure 4.1. Reactors of (a) 10 and (b) 50 L.

Figure 4.3 (a) and (b) show the two diffusers that were built to carry out the ethanol stripping experiments at the 10 L rector: 8-arm rosette (R8H), and stainless-steel sintered disk (SSD). The RH8 sparger was comprised of 8 perforated Nylon rods, containing 34 orifices of 300 μm each in diameter, comprising a total of 272 orifices. The SSD sparger was comprised of a 304 stainless-steel sintered disc of 100 mm in diameter, 30 mm in thickness, and pores of 5 mm, similar to the spargers reported in the literature as the effective type to generate microbubbles (Abdulrazzaq et al., 2016; Al-Yaqoobi et al., 2016; Brittle et al., 2015; Desai et al., 2021; Hanotu et al., 2013, 2016; Hanotu et al., 2017). The R8H and SSD spargers were used to generate fine and microbubbles, respectively since the size of generated bubbles depends on both the pulsed gas

flow and the kind of sparger used. Figs. 4.2 (c) and (d) show the difference in bubbles generated by the R8H and SSD spargers, under the same operating conditions.

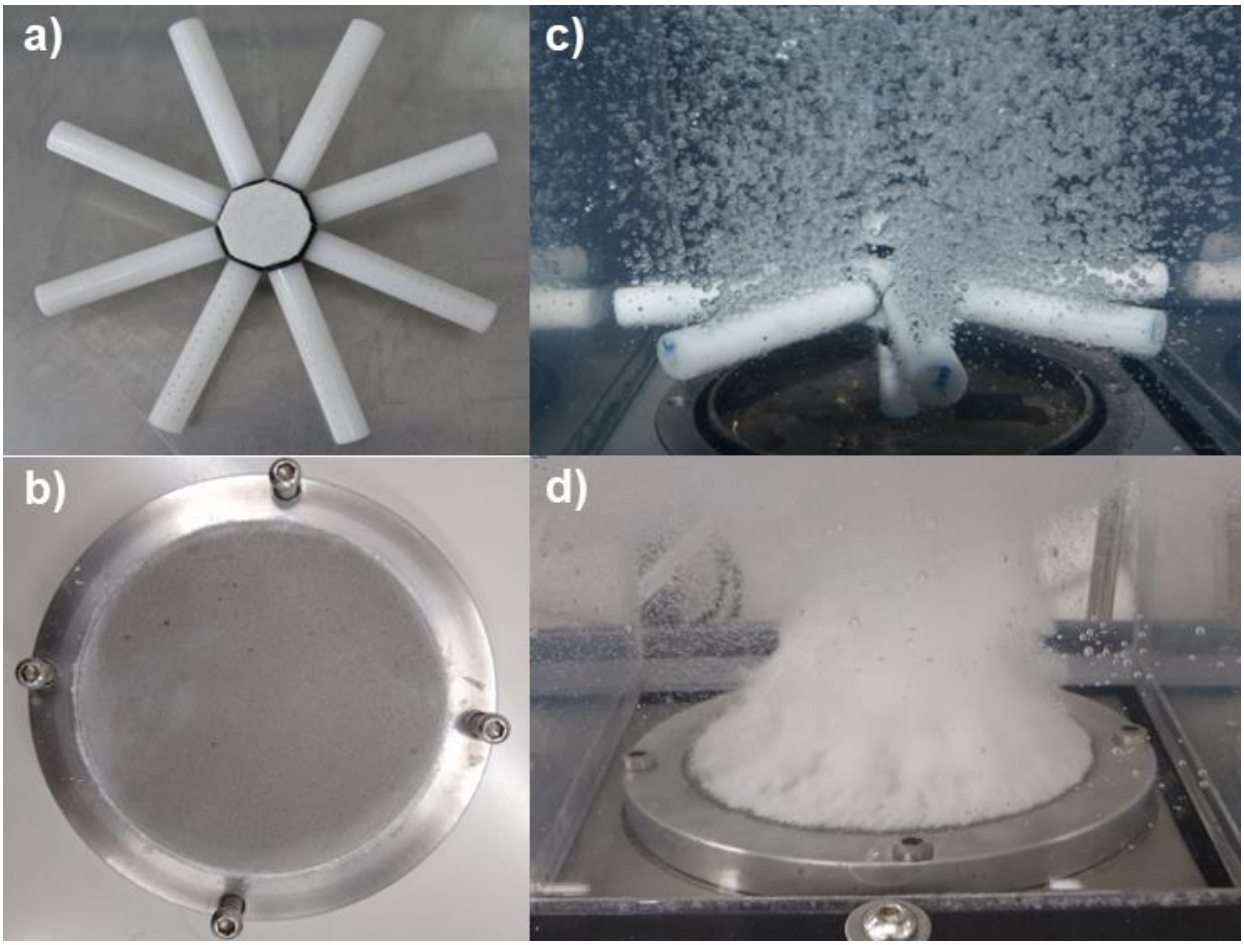

Figure 4.3. Spargers used in the stripping experiments (a) R8H, (b) SSD, and the profiles of bubbles generated by the (c) R8H and (d) SSD spargers.

The scale-up criterion for the design of the sparger used in the 50 L reactor, named PS3 (Polyacetal Sparger 0.3 mm), which also serves as the base of the reactor, was based on the gas velocity at the orifices of the R8H sparger. The gas flow rate in the 10 L reactor ranged from 3 to 10 L min^{-1}, which corresponds to a gas velocity at each orifice ranging from 2.6 to 8.6 m s^{-1}, which the best results being around 4.0 m s^{-1}, as calculated using Eq. 4.1.

$$U_S = \frac{4 \cdot \dot{Q}}{n \cdot \pi \cdot d_o^2} \tag{4.1}$$

Where U_S is the gas velocity in the orifice (cm s^{-1}), $\dot{Q}$ is the total gas flow rate in the sparger (cm^3 s^{-1}), n is the total number of orifices in the sparger, d_o is the diameter of the orifices on the sparger (cm).

Therefore, the PS3 sparger was built in polyacetal, designed in a rectangular shape with a total side length of 300 mm, with 2622 orifices of 300 µm each. Those orifices were evenly drilled and arranged on 38 internal gas distribution channels in a square area measuring 240 cm on each side. There were four gas inlets distributed in each corner of the sparger as can be seen in Fig. 4.3 which depicts the PS3 sparger. Its design allows the operation of gas flow rates of up to 50 L min^{-1}, corresponding to a gas velocity of 4.5 cm s^{-1} in each hole, which matches the best operational range obtained for the R8H sparger.

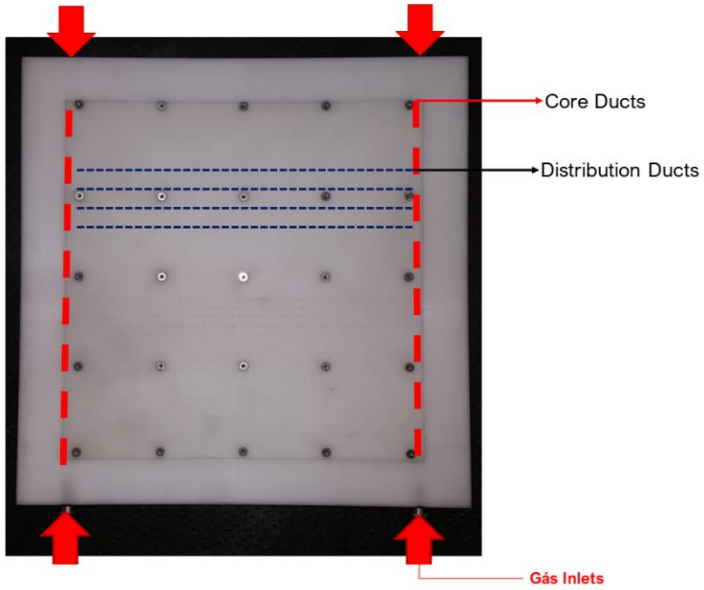

Figure 4.4. PS3 sparger.

4.3.2 Stripping Experiments

Hydroalcoholic solutions of ethanol and distilled water at a concentration of 80.0 g L^{-1} of ethanol (99.8% of purity) were used to perform stripping experiments using carbon dioxide. The 10 L reactor was used to conduct stripping experiments with CO_2 flow rates of 3.0, 6.5, and 10.0 L min^{-1} for liquid volumes of 1.0, 4.5, and 8.0 L. The aim of changing the volumes of the

hydroalcoholic solution was to assess the role of the height of the liquid in the mechanical entrainment effect. Each operational condition was tested using both the R8H (fine bubbles) and SSD (microbubbles) spargers. The pressure of the gas was adjusted at 3.5 bar in the inlet of a solenoid valve (SX-11AG, SMC, Japan), which was controlled by a PWM module (Pulse Width Modulation). The settings of the PWM module were adjusted at a frequency of 100 Hz and a duty cycle of 4%.

The solenoid valve was used to generate pulsed gas flow to decrease the diameter of bubbles formed by the sparger. The research group has extensively investigated the condition of 100 Hz and duty cycle of 4%, which has proven to be effective in reducing the bubble diameter for the R8H sparger compared to the conventional flow rate. During the experiments, a purge of CO_2 was introduced into the outlet pipe of the valve, as the minimum operating flow rate of the valve is 15 L min^{-1}, whereas the volumetric gas flow rates used in the stripping operation reached a maximum of 10 L min^{-1}. Therefore, the control of the flow rate for each operation condition was done by adjusting the purge valve. A scheme of the experimental setup for the 10 L reactor is shown in Fig. 4.4.

At the start of the experiment, the flow rate was calibrated using a mass flow meter (GFC-17, Aalborg, Denmark) at the outlet gas stream of the reactor. The experiments were conducted in an open atmosphere to avoid the formation of any kind of condensation of vapors in the headspace. This care was required to assess the role of the bubbles in the stripping process and the effect of the thermodynamic and mechanical entrainments without any interference of other phenomena. Thus, the gas flow rate was monitored and adjusted hourly when the lid of the reactor was closed. The stripping experiments were carried out for a duration of four hours, with the liquid temperature maintained at 34°C, consistent with ethanol fermentation processes in the industry (Veloso et al., 2019). Temperature control was achieved by recirculating the hydroalcoholic liquid solution through tubing placed inside a thermostatic bath (Ethik Technology 521TD, Brazil) set to 42°C. Hourly liquid samples were collected to determine the ethanol concentration, while the reactor volume was assessed by measuring the liquid level on the reactor wall.

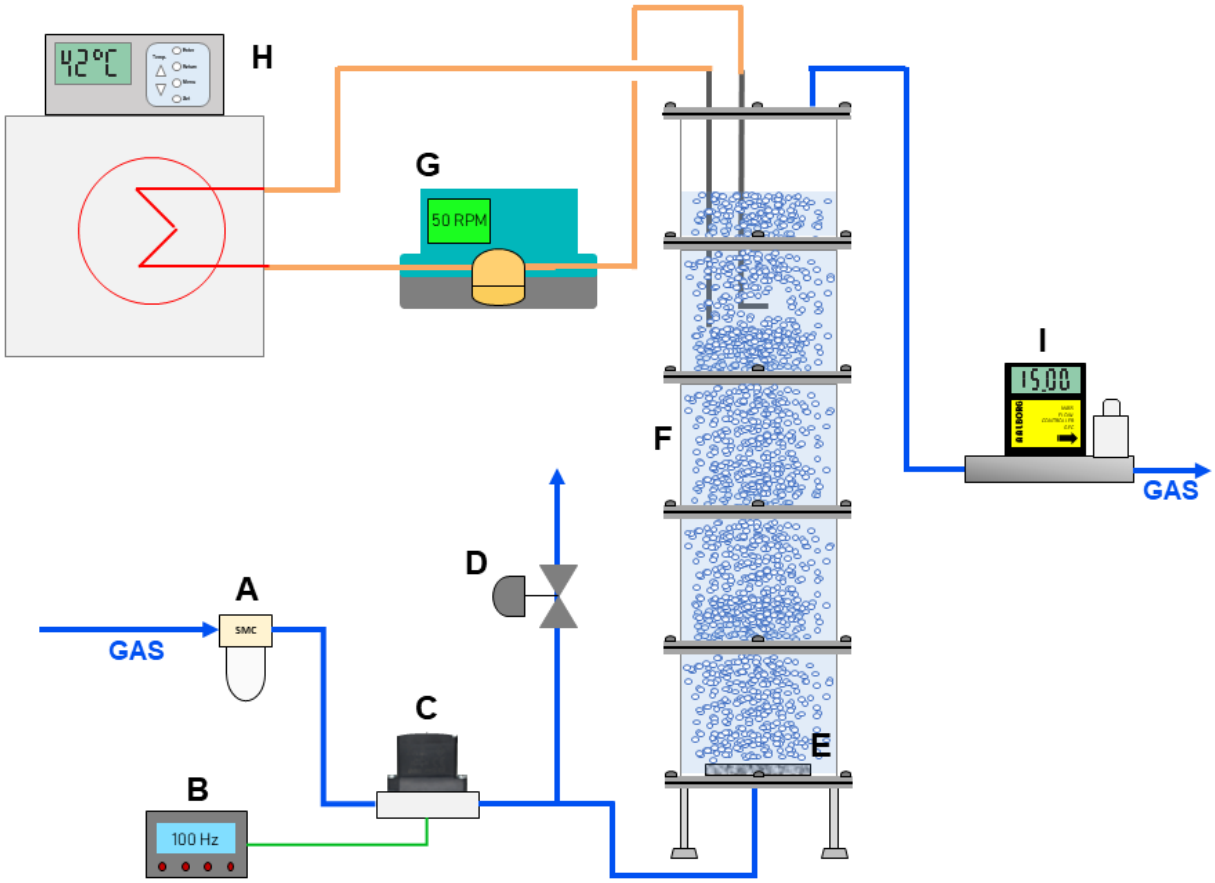

Figure 4.5. Experimental setup for 10 L reactor. (A) gas filter; (B) PWM module; (C) solenoid valve; (D) purge valve; (E) sparger; (F) 10 L bubble column reactor; (G) pump of medium recirculation; (H) thermostatic bath; (I) mass flow meter.

The stripping experiments conducted in the 50 L reactor were carried out with CO_2 flow rates of 20 and 40 L min^{-1}, while maintaining a constant volume and initial ethanol concentration of hydroalcoholic solution at 50 L and 80 g L^{-1}, respectively. Each of the gas flow rates was supplied to the reactor in two different modes: continuous (conventional method) and pulsed flow using a solenoid valve operated at frequencies of 70 and 120 Hz for flow rates of 20 and 40 L min^{-1}, respectively. For continuous gas supply, the flow rate was measured and controlled by the mass flow meter. In the case of pulsed flow, the flow rate control was achieved by setting the duty cycle values in the PWM module, with duty cycles of 5 and 12% for frequencies of 70 and 120 Hz, respectively.

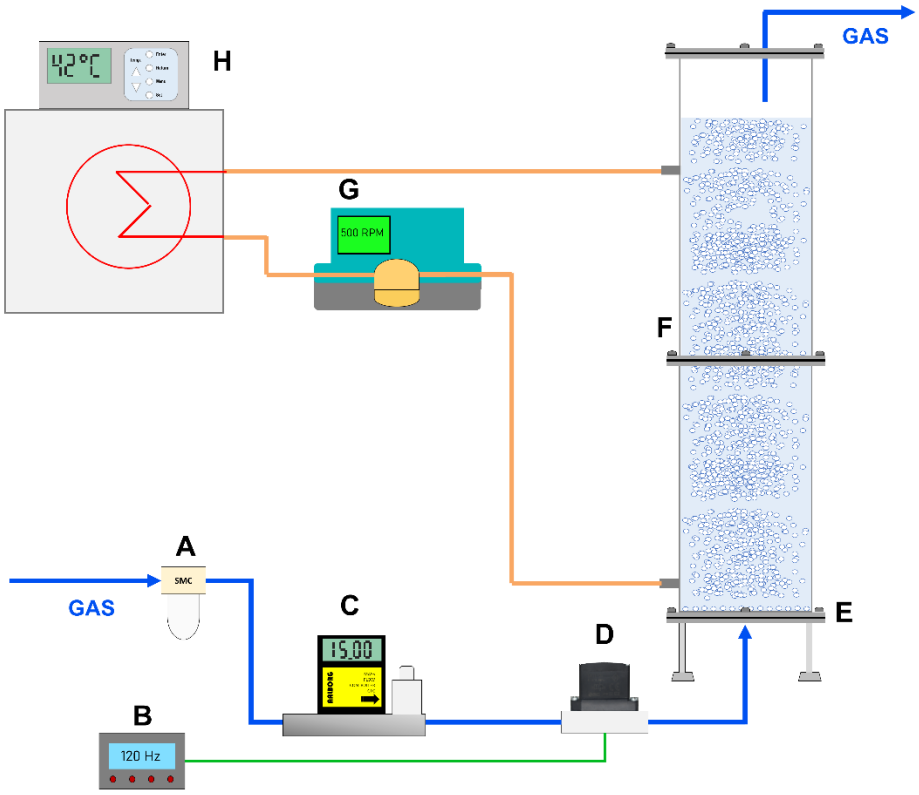

Figure 4.6. Experimental setup for the 50 L reactor. (A) gas filter; (B) PWM module; (C) mass flow meter; (D) solenoid valve; (E) sparger; (F) 50 L bubble column reactor; (G) pump of medium recirculation; (H) thermostatic bath.

No purging valve was required at this scale as the minimum operating flow rate for the experiments exceeded the minimum operating flow rate of the high-frequency solenoid valve. The temperature control system for the 50 L reactor was the same as that used for the 10 L reactor, as shown in the experimental setup diagram in Figure 4.5, as so the procedures for sampling and measuring the volume hourly.

4.3.3 Image Analysis: Determination of Sauter Mean Bubble Diameter

The image acquisition technique was used to determine the bubble diameters generated by the R8H and PS3 spargers for the 10 L and 50 L reactors, respectively. This technique has been widely adopted by various research groups used (Brittle et al., 2015; Song et al., 2021; Tesař, et al., 2009) and has proven to be one of the most accurate methods for determining the bubble diameter distribution in a gas-liquid system. The operational conditions used in the experiments

corresponded to gas flow rates ranging from 3.0 to 10 L min^{-1} for the R8H sparger and 20 and 40 L min^{-1} for the PS3 sparger, with an ethanol concentration in the liquid phase of approximately 80 $g.L^{-1}$.

The images of bubbles were captured using a Nikon D5200 camera and Nikon DX lens (AF-S NIKKOR 18-55 mm 1: 3,5-5,6 G). The image acquisition settings were configured for automatic mode with a focus on the shutter speed, set to 1/4000 s to capture sharp images of the bubbles while minimizing the impact of any movement. Due to the brief exposure time, additional lighting was provided using two 50 W LED bulbs, strategically positioned on either side of the reactor's face. To enhance the visibility of the bubbles, a dark background was installed inside the reactor, maintaining a constant distance of 4 mm from its internal surface. This setup ensured sufficient contrast in the bubble boundaries for accurate imaging.

ImageJ (1.53 k, National Institutes of Health (NIH), Bethesda, MD, USA), an open-access image-processing program, was used to obtain the binary images (grayscale) with a posterior treatment of them. The images were converted to the 8-bit format and pre-processed with the subtraction of the background before the automatic analysis of the diameters. As attested by Mohagheghian et al. (2020), the spheres were considered ellipsoids in shape and their equivalent diameters can be obtained by Eq. (4.2). ImageJ software provides automatically the measurement of the major and minor axes of the bubbles, which values were used in the determination of the equivalent diameter (Mohagheghian et al., 2020).

$$d_i = \sqrt{\frac{\alpha^2}{A_R}} \tag{4.2}$$

Where d_i is the equivalent diameter (mm) of each bubble, A_R is the aspect ratio of the bubble (α/β), and α and β are the major and minor bubble axes, respectively. The Sauter mean diameter (d_{32}) is the value used to express the average bubble size for a sample of bubbles and can be calculated by using Eq. (4.3), which shows the relation between the volume and the surface area of each bubble.

$$d_{32} = \frac{\sum_{i=1}^{n} d_i^3}{\sum_{i=1}^{n} d_i^2} \tag{4.3}$$

4.3.4 Ethanol Concentration Analysis

Samples of 2.0 mL of liquid solution were collected every hour and stored under refrigeration for subsequent analysis. Sample spectra were acquired using a fiber-optic attenuated total reflection probe coupled to a Fourier transform infrared spectrometer (ReactIR 45 m, Mettler-Toledo AutoChem, Inc.). The system was equipped with a liquid nitrogen-cooled mercury-cadmium-telluride detector and a purge system employing nitrogen gas to remove CO_2 and water from the optical compartment. The spectra were acquired in the range from 3000 to 15,000 nm, at a resolution of 4.2 nm, with 256 scans per sample. An air background spectrum was acquired before starting each experiment. To assess the saturation of the bubbles, the gas phase of the reactor was led to a gas chamber of the FTIR, where the concentration of ethanol could be assessed.

For determination of the contents of water and ethanol in the outlet gas phase of the reactor and, consequently, the concentration level of the bubbles, the mixed gas stream (water, ethanol, and CO_2) was directed to the gas sampling chamber through a stainless steel pipeline heated to 80 °C to prevent condensation. The spectra were acquired in the range from 3335 to 15411 nm (256 scans per sample, 4.2 nm resolution), at 110 °C (the temperature of the gas chamber). Prior to the analyses, nitrogen gas was used to purge air and water from the gas chamber, after which a background spectrum of nitrogen gas was acquired. To cover a wide calibration range, a total of 44 samples with various combinations of molar fractions of ethanol and water were used in the calibration procedure, as described by Santos et al. (2022). The PLS model was generated using a calibration dataset consisting of the FT-MIR spectra for gas streams with varying ethanol and water molar fractions, determined by a combination of thermodynamic assumptions and mass balances (Santos et al., 2022).

4.3.5 Saturation of Bubbles: Theoretical Estimation

The theoretical time for a bubble of a defined diameter to reach saturation in ethanol and water was initially determined. The methodology used was the same as proposed by Ezeji et al. (2005), in which the authors estimated the time for a bubble to saturate in butanol. The mass transfer coefficients for ethanol and water in CO_2 were obtained from Cussler (2009) and used in this study. Together with the time the bubble requires to saturate, it was also necessary to estimate the rising velocity of the bubble to establish which would be the minimum height of liquid to reach the gas saturation in the bubble.

The rising velocity of the bubbles was first proposed by Clift et al. (1978) and evolved to a parametrization method more recently by Park et al., (2017). The methodology is based on the determination of the Eotvos (E_o), Reynolds (Re), and Morton (M) numbers, which are calculated using Eqs. (4.4) to (4.6). The Eotvos number represents the ratio between the body and surface tension forces, while the Reynolds number expresses the relation between the inertial and viscous forces.

$$E_o = \frac{g \cdot \rho_L \cdot d_b^2}{\sigma_L} \tag{4.4}$$

$$Re = \frac{v_b \cdot \rho_L \cdot d_b}{\mu_L} \tag{4.5}$$

$$M = \frac{g \cdot \mu_L^4}{\rho_L \cdot \sigma_L^3} \tag{4.6}$$

Where, μ_L is the viscosity (Pa s), ρ_L is the density (kg m^{-3}), σ_L is the superficial tension of the liquid solution (N m^{-1}), g is the gravity acceleration (m s^{-2}), d_b is the diameter of the bubble (m), and v_b is the final rising velocity of the bubble (m s^{-1}).

The parameterization proposed by Park et al. (2017) overcomes the need for prior determination of the bubble shape. This aspect proves to be advantageous compared to the equations initially proposed by Clift et al. (1978), enabling the determination of the bubble rise velocity based solely on the physical properties of the liquid solutions used and the Sauter diameter of the generated bubbles, as shown in the Eq. (4.7).

$$Re = \frac{1}{\sqrt{f_{sc}^2 \left(\frac{144 \cdot M}{E_o^3} + \frac{M^{5/6}}{0.14425^2 \cdot E_o^{5/2}} \right) + \frac{M^{1/2}}{E_o^{1/2}(2.14 + 0.505 \cdot E_o)}}} \tag{4.7}$$

Where, f_{sc} is a factor accounting for the suppressed internal gas circulation due to surface contaminants, calculated using Eq. (4.8).

$$f_{sc} = 1 + \left(\frac{0.5}{1 + Exp\left(\frac{\log E_o + 1}{0.38} \right)} \right) \tag{4.8}$$

The calculation of the time required for bubble saturation in ethanol and water was carried out using the methodology proposed by Ezeji et al. (2005). The authors developed an overall mass balance for the bubble (Eq. (4.9)) coupled with the mass transfer equation (Eq.(4.10)) which turned out the equation to determine the time to saturate the bubble, shown in Eq. (4.11).

$$\frac{V_b}{R \cdot T} \cdot \frac{dp_1}{dt} = N_1 \cdot A_b \tag{4.9}$$

$$N_1 = (p_1^* - p_1) \cdot K_P \tag{4.10}$$

Integrating with the following boundary conditions:

$p_1 = 0$ at $t = 0$, $p_1 = 0.95 \cdot p_1^*$ at $t = t$

$$t = \frac{d_b}{2 \cdot R \cdot T \cdot K_P} \tag{4.11}$$

Where, V_b is the volume of the bubble (cm^3), R is the universal gas constant (82.05 cm^3 atm mol^{-1} K^{-1}), T is the temperature of the gas (K), N_1 is the flux of ethanol/water (mol cm^{-2} s^{-1}), A_b the area of the bubble (cm^2), p_1 is the partial pressure of ethanol/water in the bubble (atm), p_1^* is the hypothetical partial pressure of ethanol/water in equilibrium with the bulk liquid concentration (atm), K_P is the overall gas side mass transfer coefficient (mol cm^{-2} s^{-1} atm^{-1}), and t is the time required to saturate the bubble.

The overall gas side mass transfer coefficient K_P for the ethanol and water can be calculated using its definition (Cussler, 2009) given by Eqs. (4.12) to (4.14).

$$K_P = \frac{1}{\frac{1}{k_P} + \frac{H}{k_L}} \tag{4.12}$$

$$k_P \approx \frac{D}{L \cdot R \cdot T} \tag{4.13}$$

$$k_L \approx \frac{D_{EtOH-H2O}}{L} \tag{4.14}$$

Where k_P is the gas film mass transfer coefficient (mol cm^{-2} s^{-1} atm^{-1}), k_L is the liquid mass transfer coefficient for the solvent (cm s^{-1}), H is the Henry's law constant for the solvent in the gas (atm cm^3 mol^{-1}), T is the temperature of the gas phase, D is the diffusion coefficient of the solvent in the gas (cm^2 s^{-1}), $D_{EtOH-H2O}$ is the diffusion coefficient of ethanol in water and vice-versa (cm^2 s^{-1}), and L is the regular value used for the thickness of the stagnant liquid layer of the bubble (0.01 cm).

We could consider the temperature of the gas inside the bubble be the same of the temperature of the liquid medium. Although the temperature of the gas is approximately 20°C before being fed to the reactor, the passage of gas through the connecting tubes with the reactor and the sparger ensures that the gas inside the bubbles reaches a temperature very close to that of the liquid. However, Eq. (4.15) was used to estimate the time required for the bubble to reach the temperature of the liquid phase in case its initial temperature was 20°C. The model was proposed by Santana (1994) and considers no temperature gradient in the gas inside the bubble – which is suitable but not possible to affirm or measure. That means the only resistance considered for the heat transfer is the liquid layer surrounding the bubble.

$$ln\frac{T_\infty - T}{T_\infty - T_0} = -\frac{h_L \cdot A_b \cdot t}{C_{Pg} \cdot V_b \cdot \rho_g} \tag{4.15}$$

Where T_∞ and T_0 are the liquid and the initial bubble temperatures (K), h_L is the convective heat transfer coefficient of the liquid solution (J m^{-2} K^{-1} s^{-1}), A_b is the area of the bubble (m^2), V_b is the

volume of the bubble (m^3), ρ_g is the density of the gas (kg m^{-3}), and C_{Pg} is the specific heat at constant pressure of the gas (J kg^{-1} K^{-1}).

4.3.6 Saturation of Bubbles: Experimental Procedure

Stripping experiments were performed in the 10 L reactor close to the atmosphere, under atmospheric pressure, to determine the extent of saturation of the gas phase. Two out of the five available modules were utilized, allowing for working with solution volumes of 1.0 and 4.5 L, respectively. The R8H sparger was used under two temperature conditions, 22 and 34°C, and SSD sparger for 34°C. The liquid phase temperature was maintained constant using a thermostatic bath (Ethik Technology 521TD, Brazil), and the entire system, including the reactor (side and top walls) and gas outlet pipes, was covered with thermal insulation and controlled by an electric resistor through a dimmer to match the liquid phase temperature. Temperature measurements of the pipes and reactor walls were regularly taken using an infrared thermometer (Major Tech MT694 Infrared Thermometer). The gas exiting the reactor was directed through the outlet pipe to the gas composition analysis chamber of the FTIR equipment for ethanol gas phase composition analysis, which results were monitored and acquired on a laptop, as shown schematically in Fig. 4.6. Gas flow rates varied from 1.0 to 10 L min^{-1} for the two liquid volumes and the two operating temperatures. To ensure no contamination from thermodynamic entrainment due to solution droplets carried by mechanical entrainment, a long gas outlet line (approximately 4 m) with several fittings (curves and elbows) was set up. The schematic shown in Fig. 4.6 is purely illustrative.

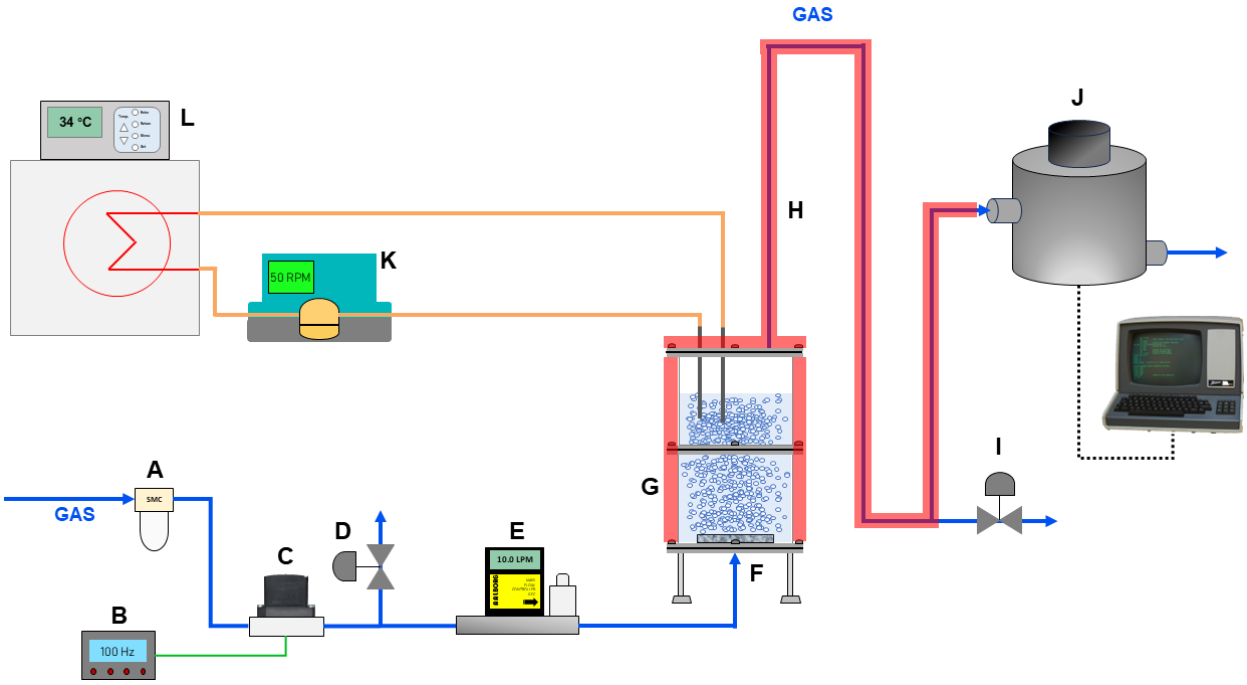

Figure 4.7. Experimental setup for saturation determination. (A) gas filter; (B) PWM module; (C) solenoid valve; (D) purge valve; (E) mass flow meter; (F) bubble column reactor; (G) insulator; (H) exit gas tubing; (I) purge valve; (J) ReactIR gas chamber; (K) pump of medium recirculation; (L) thermostatic bath.

Unlike the other stripping experiments in this study, the experiments to determine the degree of bubble saturation were conducted with the reactor lid closed. In this particular experiment, the gas phase was also analyzed, in addition to the liquid phase. To ensure accurate results, the entire headspace of the reactor and gas outlet pipes were maintained at the temperature of the liquid phase (22 or 34°C). This careful approach prevented any condensation of the thermodynamic entrainment or vaporization of the mechanical entrainment, which can occur when the headspace temperature and pipes are lower or higher than the liquid phase, respectively.

For all systems (liquid volume, temperature, and gas flow rate), the solenoid valve was set to a frequency of 100 Hz to ensure the generation of previously known bubble diameters. The flow meter was installed solely to verify the gas flow rate and was removed afterward to prevent any damping effect on the pulsed gas flow. Gas supply for each operational condition lasted approximately 5 minutes, allowing sufficient time to renew the gas phase in the reactor headspace and outlet pipes. At each operational condition, a 1.0 mL sample of liquid solution was collected

for ethanol composition analysis, while the gas phase was analyzed using the probe in the ReactIR gas chamber. There was a purge valve just before the gas chamber used to regulate the flow rate of the gas sample to be analysed.

The Modified Raoult's Law (Eq. 4.16) was used to determine the composition of the thermodynamic equilibrium in the gas phase to be compared to the experimental results obtained in the gas chamber. The activity coefficients were calculated using the Non-Random Two Liquid Model (NRTL), which is based on the use of empirical binary parameters of interaction.

$$y_i P = x_i \gamma_i P_i^{sat} \tag{4.16}$$

Where y_i is the mole fraction of component "i" in the gas phase, P is the total pressure of the system (kPa), x_i is the mole fraction the component "i" in the liquid phase, γ_i is the activity coefficient of the component "i" in the liquid phase, and P_i^{sat} is the vapour pressure of the component "i" (kPa).

Antoine Equation Eq. (4.17) was used to calculate the vapour pressure of ethanol and water.

$$\ln P_i^{sat} = A \cdot ln(T) + \frac{B}{T} + C + D \cdot T^2 \tag{4.17}$$

Where A, B, C, and D are the Antoine's constants for each component, and T is the temperature of the system (K).

The gas component (CO_2) was considered insoluble in liquid phase since $x_{CO2} \ll x_{EtOH}$ (1.10^2 times smaller) and its presence in the calculations highly increases the numerical complexity of the forward integrations.

4.3.7 Determination of Thermodynamic and Mechanical Entrainments

In each of the stripping experiments conducted, as described in section 4.3.2, equations were fitted to the experimental data points of ethanol concentration (C_E) and liquid volume (V_L) decay over the 4-hour duration of the experiment. The density of the solution (ρ_L) was calculated

using Eq. (4.18) as a function of the ethanol concentration, and the concentration of water (C_W) was determined by the difference of ρ_L and C_E, as shown in Eq. (4.19).

$$\rho_L = 994.04 + 1.54 \cdot 10^{-4} \cdot C_E^2 - 0.19048 \cdot C_E \quad (4.18)$$

$$C_W = \rho_L - C_E \quad (4.19)$$

Where ρ_L is the liquid density (g L^{-1}), C_W is the water concentration (g L^{-1}), and C_E is the ethanol concentration (g L^{-1}).

The C_E and C_W for each experimental data point were converted into moles using Eq. (4.20) to standardize the calculation basis with the units used in thermodynamic equilibrium. Second-degree equations were used to fit the experimental decay of ethanol and water number of mols in the liquid phase ($f(t)$), reaching R^2 values over 0.98. This approach was applied to determine the experimental number of moles of each species in the liquid phase for any interval of time (Δt) during the experiment.

$$n_i^L = \frac{C_i \cdot V_L}{MM_i} \quad (4.20)$$

Where n_i^L is the number of mols of specie "i" in the liquid phase (mol), C_i is the concentration of specie "i" in the liquid phase (g L^{-1}), MM_i is the molecular mass of specie "i" (g mol^{-1}) and V_L is the volume of the liquid phase in the reactor (L).

The experimental removal of ethanol and water from the liquid phase was due to the removal promoted by the gas flow rate, which is a result of both thermodynamic and mechanical entrainments. The total number of moles of each species removed by the gas flow rate can be expressed by Eq. (4.21).

$$n_i^{R_{Exp}}(t) = n_{i0}^L - f_i(t) \quad (4.21)$$

Where $n_i^{R_{Exp}}$ is the total experimental number of moles of specie "i" removed by the gas flow rate during the stripping process (mol), n_{i0}^L is the initial number of moles of specie "i" in the liquid phase (mol), and $f_i(t)$ is the function of time which gives the experimental remaining number of mols of specie "i" in the liquid phase (n_i^L) at t moment of stripping (mol).

A molar balance was proposed for the ethanol and water removal in the liquid phase, based on the gas flow rate used for each experiment, as show in Eqs. (4.22) and (4.23).

$$\frac{dn_E}{dt} = -\dot{n}_E^o \tag{4.22}$$

$$\frac{dn_W}{dt} = -\dot{n}_W^o \tag{4.23}$$

Where n_E and n_W are the number of moles of ethanol and water in the liquid phase (mol), respectively, $\dot{n}_E^o$ and $\dot{n}_W^o$ are the mol flow rate of ethanol and water that exits the reactor (mol min^{-1}), respectively.

Considering the hypothetical situation in which the removal of ethanol and water was due only to the thermodynamic entrainment, the molar flow rate of each species that exits the reactor can be calculated using Eqs. (4.24) to (4.26). It is considered that the molar flow rate of pure gas entering and exiting the reactor is the same (Eq. (4.24)).

$$\dot{n}_G^o = \dot{n}_G^i = \frac{P_{Cal} \cdot \dot{Q}}{R \cdot T_{Cal}} \tag{4.24}$$

$$\dot{n}_E^o = \frac{\dot{n}_G^i}{y_3}\, y_1 \tag{4.25}$$

$$\dot{n}_W^o = \frac{\dot{n}_G^i}{y_3}\, y_2 \tag{4.26}$$

Where $\dot{n}_G^i$ and $\dot{n}_G^o$ are the molar flow rates of gas entering and exiting the reactor (mol min^{-1}), respectively, $\dot{Q}$ is the volumetric gas flow rate fed to the reactor (L min^{-1}), P_{Cal} and T_{Cal} are the pressure and temperature of calibration of the mass flowmeter (100 kPa and 293.15 K), respectively, R is the universal gas constant (8314.46 L Pa K^{-1} mol^{-1}), y_1, y_2, and y_3 are the molar fractions of ethanol, water and carbon dioxide in the vapor phase, respectively.

Simulations using the open-source software SciLab (version 6.1.1) were performed using the 4th Order Runge-Kutta method to solve Eqs. (4.22) and (4.23) and come up with a solution to the decay of ethanol and water number of mols in the liquid phase ($g_i(t)$). The inputs for the solution were the volumetric gas flow rate ($\dot{Q}$) and the initial moles of ethanol and water in the liquid phase for each experiment, n_{E0}^L and n_{W0}^L, respectively. The outcome of the simulations was Eq. (4.27) which determines the total ethanol removed by the thermodynamic entrainment solely ($n_i^{R_{Therm}}$).

$$n_i^{R_{Therm}}(x_i, t) = n_{i0}^L - g_i(x_i, t = \Delta t) \tag{4.27}$$

Where $n_i^{R_{Termo}}$ is the number of moles of specie "i" removed by the thermodynamic entrainment solely (mol), n_{i0}^L is the initial number of moles of specie "i" in the liquid phase, and $g_i(t)$ is the solution of the differential equation provided by the Runge-Kutta method, which expresses the decay of the number of moles of specie "i" in the liquid phase due to the thermodynamic entrainment (mol).

However, by simulating the thermodynamic removal for a stripping duration of $t = 240$ min and comparing the final concentration of ethanol one can find $x_{E_{Therm}} > x_{E_{Exp}}$. This means that the decay in concentration for the simulated and experimental processes are not the same. And here lies a trick point.

The thermodynamic entrainment is fully dependent on the time and the liquid composition (x_E). However, both mechanical and thermodynamic entrainments are responsible for the removal of ethanol and, consequently for the changes in the experimental liquid concentration. This is the reason the simulations of the ethanol removed thermodynamically cannot use a time step

comprising the whole stripping experiment (Δt=240 min). This action would overestimate the removal of ethanol by the thermodynamic entrainment since its x_E decay is slower when compared to the experimental stripping (thermodynamic and mechanical entrainments working together). In other words, the calculation of thermodynamic equilibrium must track the experimental change in the liquid phase concentration (x_E), to correspond to reality.

An alternative for this problem would be to use an Δt small enough, which would not cause any significant change in the concentration of the liquid phase (pseudo-steady state), for different initial concentrations of ethanol. By doing so, it would be possible to obtain a new function $z_i(x_E)$ (Eq. (4.28)), representing the fraction of ethanol removed by the thermodynamic entrainment relative to the total removed, using $n_i^{R_{Therm}}$ as a function of x_E solely. The change of calculation basis is the ace in the hole of the study.

The integration time step Δt in Eq. (4.28) is there just to indicate the pseudo-stationary state, it does not mean time dependence. Previous attempts showed that a $\Delta t \leq 5$ min presented no difference in the fraction of the thermodynamic entrainments, thus as a safe procedure to generate the function $z_i(x_i)$, the value of $\Delta t = 2$ min was chosen for all simulations for each stripping experiment.

$$z_i(x_i) = \frac{n_i^{R_{Therm}}(x_i, \Delta t)}{n_i^{R_{Exp}}(\Delta t)}, \qquad \Delta t = 2\ min \tag{4.28}$$

After determining de $z_i(x_E)$ function, it becomes possible to calculate and assess the total ethanol and water removed by the thermodynamic entrainment for any t during the entire 4-hour long stripping experiment using Eq. (4.29), finally as time-dependent expression, indeed.

$$n_i^{R_{Therm}}(x_i, t) = n_i^{R_{Exp}}(t) \cdot z_i(x_i) \tag{4.29}$$

The number of mols of specie "i" removed by the mechanical entrainment ($n_i^{R_{Mech}}$) can be calculated using Eq. (4.30) which is the difference between the experimentally removed ethanol and the thermodynamic entrainment.

$$n_i^{R_{Mech}}(x_i, t) = n_i^{R_{Exp}}(t) \cdot \left(1 - z_i(x_i)\right) \tag{4.30}$$

Thus, the total experimental removal of species "i" at the end of the stripping experiments, and the thermodynamic and mechanical entrainments removal were calculated using Eqs. (4.21), (4.29), and (4.30) at $t = 240$ min, respectively.

The experimental specific selectivity (β_{Exp}) was calculated using Eq. (4.31). This parameter assesses the level of ethanol concentration in the gas phase at the end of the process compared to the initial concentration of ethanol in the liquid phase.

$$\beta_{Exp} = \frac{n_E^{R_{Exp}}(t)/n_W^{R_{Exp}}(t)}{n_{E0}^L/n_{W0}^L}, \quad t = 240\,\text{min} \tag{4.31}$$

Where $n_E^{R_{Exp}}$ is the total experimental removal of ethanol (mol), $n_W^{R_{Exp}}$ is the total experimental removal of water (mol), n_{E0}^L is the initial ethanol content in the liquid phase (mol), n_{W0}^L is the initial water content in the liquid phase.

Eqs. (4.32) and (4.33) are used to calculate the specific selectivity reached by the thermodynamic (β_{Therm}) and mechanical (β_{Mech}) entrainments separately.

$$\beta_{Therm} = \frac{n_E^{R_{Therm}}(t)/n_W^{R_{Therm}}(t)}{n_{E0}^L/n_{W0}^L}, \quad t = 240\,\text{min} \tag{4.32}$$

$$\beta_{Mech} = \frac{n_E^{R_{Mech}}(t)/n_W^{R_{Mech}}(t)}{n_{E0}^L/n_{W0}^L}, \quad t = 240\,\text{min} \tag{4.33}$$

Where $n_E^{R_{Therm}}$ and $n_E^{R_{Mech}}$ are the thermodynamic and mechanical removal of ethanol (mol), $n_W^{R_{Therm}}$ and $n_W^{R_{Mech}}$ are the thermodynamic and mechanical removal of water (mol).

4.4 Results

4.4.1 Sauter Mean Bubble Diameter for R8H Sparger

Three photos were analyzed for each operational condition, each containing approximately 500 bubbles. Those images were examined to determine the bubble diameter distribution and, consequently, the Sauter mean diameter. The images of bubbles obtained for subsequent treatment to determine the Sauter mean diameter can be observed in Fig. 4.7. After processing the images using ImageJ software, the values of d_{32} obtained can be seen in Figure 4.8. The increase in the mean bubble diameters can be approximated by a linear equation (Eq. 4.34). The valve operation frequency was set at 100 Hz, which corresponds to the same condition used in the subsequent stripping experiments.

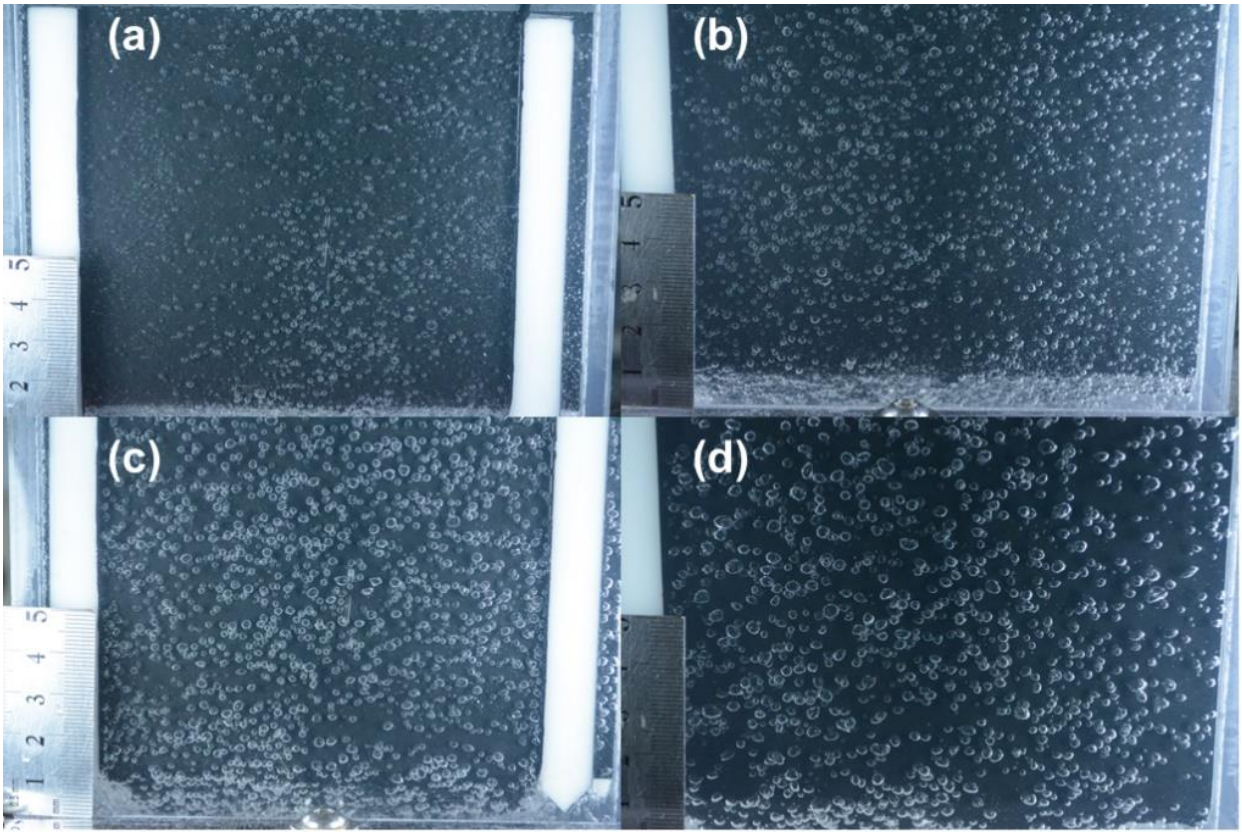

Figure 4.8. Bubbles profile in the 8.0 L hydroalcoholic solution under the conditions of **(a)** 1.0 L min^{-1}, **(b)** 3.0 L min^{-1} **(c)** 6.5 L min^{-1}, and **(d)** 10.0 L min^{-1} of gas flow rates.

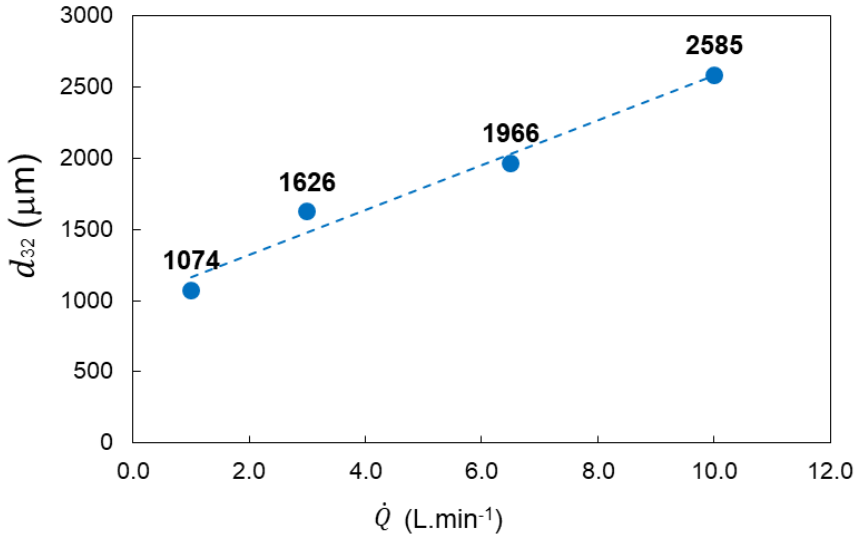

Figure 4.9. Sauter mean bubble diameter (d_{32}) profile for the 8.0L solution operated with the R8H sparger.

$$d_{32} = 157.21 \cdot \dot{Q} + 1007.1 \ \ (R^2 = 0.9718) \tag{4.34}$$

Indeed, the determination of bubble diameter in the system is of great importance for theoretically assessing the conditions of ethanol and water saturation within the bubbles. Parameters such as the rise velocity and saturation velocity of the bubbles are dependent on their diameter. By accurately measuring the bubble diameter, we can better understand the behavior of bubbles in the stripping process and predict their interactions with the surrounding liquid phase.

Fig. 4.9 presents the images captured during the airflow rate of 3.0 L min^{-1} using the SSD sparger. Measuring the bubble diameter for this sparger was challenging due to the presence of microbubbles that extended beyond the available measurement scale (1.0 mm). Consequently, determining their exact boundaries became impractical. While some bubbles with distinct boundaries are visible in the images, they primarily result from coalescence phenomena and do not fully represent the system for this particular sparger.

Figure 4.10. Microbubbles generated by the SSD sparger at 3.0 L min^{-1}.

4.4.2 Saturation of Bubbles - Estimation

Ensuring the saturation of bubbles in ethanol and water, that is, the condition in which thermodynamic equilibrium is achieved, is a prerequisite before any attempt to determine the effects of thermodynamic and mechanical entrainment. Simulation results obtained by Ezeji et al. (2005) for the butanol stripping system revealed that a bubble of 5.00 mm in diameter would reach saturation approximately 0.14 seconds after its formation within the liquid. Those assumptions were also carried out in this present study, following the methodology and the parameters provided by Cussler (2009). Before proceeding, it was essential to determine the bubble's rise velocity, as the liquid height is a crucial factor in ensuring that the bubble has sufficient time in the dispersed phase before reaching the liquid surface and bursting.

Using the parametrization method developed by Park et al. (2017), the simulation of the rising velocity was carried out for only one bubble of 5.00 mm in diameter. This value was chosen to overestimate the diameter of the bubble to guarantee the eventual saturation for all bubbles of smaller diameters that might be generated during the experiments of stripping. The parameters and physical properties of the hydroalcoholic solution used for the estimation and the result of the rising velocity of a bubble can be observed in Table 4.1.

Table 4.1. Parameters, physical properties, and the result obtained for the simulation of the rising velocity of a bubble in a hydroalcoholic solution.

Parameters / Properties / Result		Units
x_{EtOH}	0.08	-
μ_L	9.0E-04	Pa s
ρ_L	978.5	kg m^{-3}
σ_L	0.037	N m^{-1}
g	9.8	m s^{-2}
d_b	0.005	m
M	1.30E-10	-
E_o	6.48	-
f_{sc}	1.0	-
Re	1096.8	-
v_b	20.2	cm s^{-1}

Where, x_{EtOH} is the mass fraction of ethanol, μ_L is the viscosity, ρ_L is the density, σ_L is the superficial tension of the liquid solution, g is the gravity acceleration, d_b is the diameter of the bubble, M is the Morton number, E_o is the Eotvos number, f_{sc} is the factor accounting for the suppressed internal gas circulation due to surface contaminants, Re is the Reynolds number and v_b is the final rising velocity of the bubble.

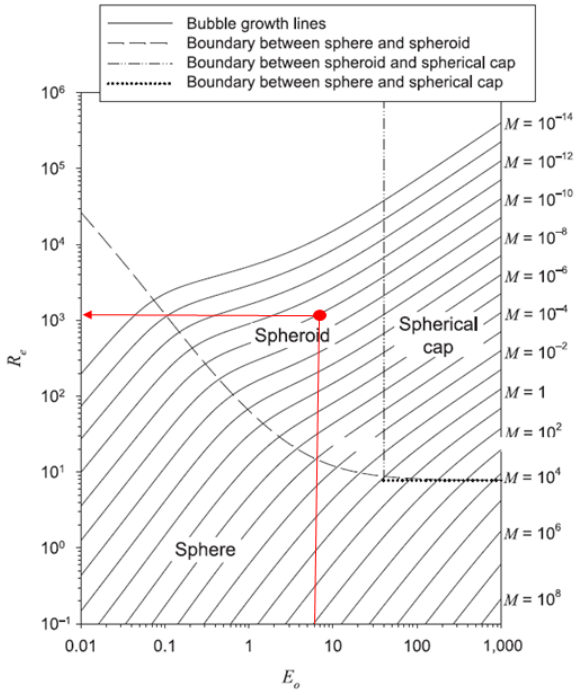

Figure 4.11. Diagram showing different bubble shape regimes in the E_o and Re plane. (Park et al., 2017).

For a 5.00 mm diameter bubble in a hydroalcoholic solution, a final rising velocity was found to be 20.2 cm s^{-1} as shown in Table 4.1. It was also found that the shape of the bubbles is spheroids, as can be seen in Fig. 4.10, which is in agreement with the images shown in Fig. 4.7.

The overall mass transfer coefficients for ethanol and water were calculated using the methodology established by Cussler (2009) and applied by Ezeji et al. (2005), considering the binaries interactions of C_2H_6O-CO_2, H_2O-CO_2 and C_2H_6O-H_2O. Estimating the overall mass transfer coefficients is crucial to provide a theoretical prediction of the time required for the bubble to reach saturation in ethanol and water. For the referred calculations, a constant temperature of 34°C was considered for both the liquid and gas phases, consistent with the stripping experiments that followed. The force constants for the interactions between the unlike pairs and the tabulated functions for the Lennard-Jones potential can be seen in Table 4.2. Table 4.3 depicts the values obtained for the gas and liquid film mass transfer coefficients, the overall mass transfer coefficients and the time to reach saturation of ethanol and water in the gas phase.

Table 4.2. Diffused coefficients for ethanol and water in carbon dioxide were calculated through the tabulated functions for the Lennard-Jones potential (Cussler, 2009).

	D (cm² s^{-1})
$EtOH - CO_2$	0.087
$H_2O - CO_2$	0.158

Table 4.3. Gas and liquid film mass transfer coefficients, and the overall mass transfer coefficients for ethanol and water.

Ethanol Diffusivity		
$k_{P_{EtOH-CO2}}$	3.46E-04	mol cm^{-2} s^{-1} atm^{-1}
$k_{L_{EtOH-H2O}}$	8.40E-04	cm s^{-1}
$K_{P_{EtOH-CO2}}$	6.75E-05	mol atm^{-1} cm^{-2} s^{-1}
$t_{EtOH-CO2}$	0.15	s
Water Diffusivity		
$k_{P_{H2O-CO2}}$	6.26E-04	mol cm^{-2} s^{-1} atm^{-1}
$k_{L_{H2O-EtOH}}$	8.40E-04	cm s^{-1}
$K_{P_{H2O-CO2}}$	3.56E-04	mol atm^{-1} cm^{-2} s^{-1}
$t_{H2O-CO2}$	0.03	s

Where D is the diffusion coefficient, k_P and k_L are the gas and liquid film mass transfer coefficients, K_P is the overall mass transfer coefficient for the gas side, and t is the time to reach the saturation in the bubbles.

The calculations of the time required to saturate the bubble in ethanol, based on the estimated mass transfer coefficients and Eq. 4.11, resulted in a value of 0.15 seconds, which is consistent with the value obtained by Ezeji et al. (2005). Additionally, the calculated time for the bubble to reach saturation in water using Eq. 4.15 was 0.03 seconds. Based on the estimates of bubble rise velocity and the time for saturation in ethanol, it can be inferred that the bubble would require a minimum liquid column of 3.00 cm to reach the thermodynamic equilibrium composition of ethanol and water. Therefore, it is estimated that all operational conditions analyzed in this study

reach saturation in both ethanol and water, as the liquid heights in every experiment exceed the 3.00 cm threshold. It is also important to note that the estimation of the saturation time was conducted considering a bubble with double the maximum diameter of the ones generated in the experiments (2.5 mm).

In an attempt to achieve greater accuracy in estimating the minimum liquid column height required to promote bubble saturation, the time for the gas bubble to reach the temperature of the liquid phase was determined. This calculation was carried out to eliminate any doubts regarding thermodynamic equilibrium, which is dependent on the temperature of the system (liquid and bubbles). Initially, the gas from cylinders entered the reactor at room temperature (25°C). Hence, the determination of the temperature inside the bubble considered the initial gas temperature of 25°C and the temperature of the liquid film equal to the operating temperature of the solution (34°C).

The gas inside the bubble was considered completely mixed, thus there was no thermal gradient within its interior, and the internal resistance was assumed to be negligible, with only the resistance of the liquid film surrounding the bubble. This assumption simplified the analysis, focusing primarily on the heat transfer at the liquid-gas interface. The parameters and the result regarding the time the bubble required to reach 34°C are depicted in Table 4.3.

Table 4.4. Parameters to calculate the time the CO_2 bubble requires to reach the temperature of the liquid phase, (NIH, National Library of Medicine, PubChem).

Parameters		Units
T_∞	307.15	K
T_0	298.15	K
h_L*	41.48	J m^{-2} K^{-1} s^{-1}
d_b	0.005	m
A_b	7.85E-05	m^2
V_b	6.54E-08	m^3
ρ_g	1.98	kg m^{-3}
C_{Pg}	846	J kg^{-1} K^{-1}

*Santana, 1994.

Where T_∞ and T_0 are the liquid and the initial bubble temperatures, h_L is the convective heat transfer coefficient of the liquid solution, d_b, A_b, and V_b are the diameter, area and volume of the bubble, ρ_g is the density of the gas at room temperature and C_{Pg} is the specific heat at constant pressure of the gas.

The time required for the bubble to reach the temperature of the liquid phase, calculated based on the considerations mentioned earlier, was 0.10 seconds. This value is still lower than the estimated time to reach thermodynamic equilibrium. We know that heat and mass transfer occur simultaneously, however, for this study, an approach that overestimates this time is already sufficient. It is worth noting that the gas enters the reactor at a temperature higher than room temperature, considering that the sparger and the entire gas delivery system are close to the liquid temperature in the reactor. Therefore, the estimation that a minimum liquid column of 3.00 cm is sufficient to saturate the bubbles is plausible.

4.4.3 Saturations of Bubbles – Experimental

Stripping experiments were conducted to analyze the experimental gas phase composition and compare those values with the saturation composition calculated by the thermodynamic equilibrium. The volumes of 1.0 and 4.5 L of hydroalcoholic solution were used, which means liquid column heights of 5.1 cm and 22.9 cm, respectively. The liquid phase in the reactor was maintained at temperatures of 22°C and 34°C using a thermostatic bath. The entire reactor and the gas outlet piping were insulated and had their temperatures monitored and controlled to match the liquid temperatures, aided by an electric resistance fixed to the reactor and piping walls. The liquid phase composition was continuously analyzed to estimate the thermodynamic equilibrium for each analyzed gas phase sample. Fig. 4.11 depicts the results obtained for each flow rate in the scales of 1.0 and 4.5 L and temperature of 22°C using the R8H sparger. Fig. 4.12 depicts the results at 34°C and comprises the data for both the R8H and SSD spargers. The ethanol compositions of the analyzed gas phase are expressed as a percentage relative to the calculated values of thermodynamic equilibrium.

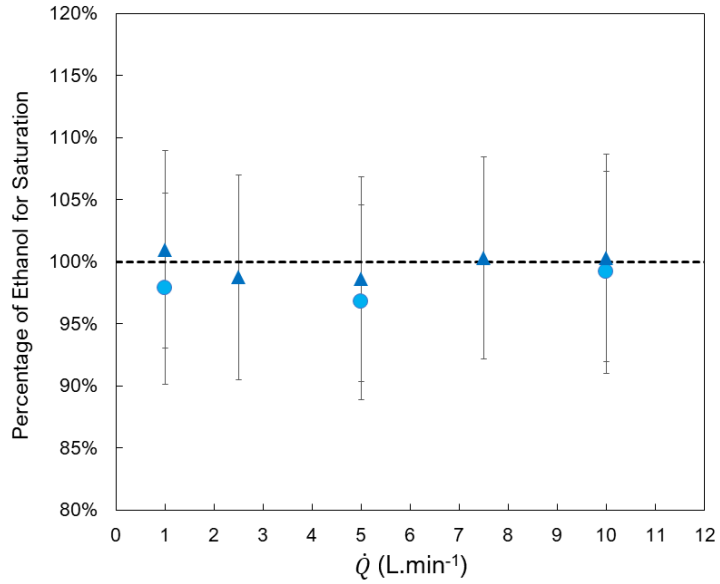

Figure 4.12. Percentage of experimental concentration of ethanol in the gas phase relative to the equilibrium concentration at 22°C using the R8H sparger. The volume of liquid of (●) 1.0 L and (▲) 4.5, and (----) saturation curve.

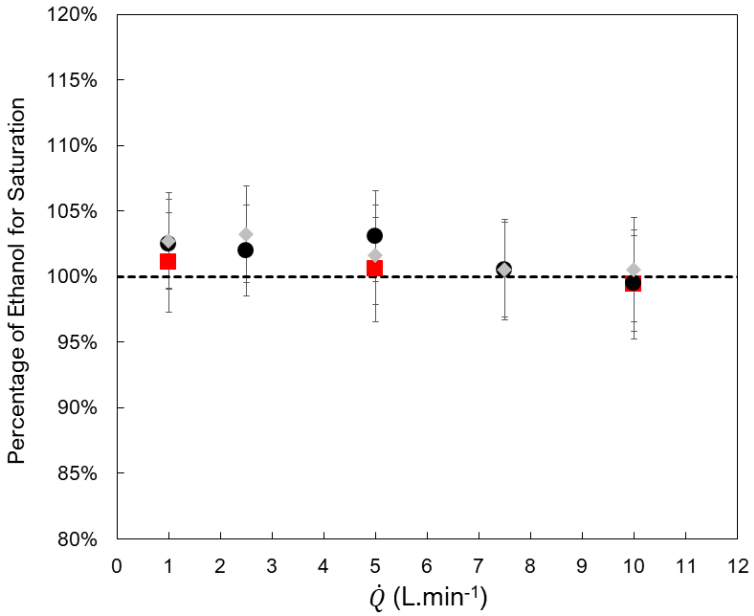

Figure 4.13. Percentage of experimental concentration of ethanol in the gas phase relative to the equilibrium concentration at 34°C. The volume of liquid of (■) 1.0 L with R8H sparger, (●) 4.5 L with R8H sparger, (◆) 4.5 L with SSD sparger, and (----) saturation curve.

The results shown in Figs. 4.11 and 4.12 demonstrate that the ethanol concentration in the gas phase reached the thermodynamic equilibrium as predicted by theoretical calculations which corroborates the previous theoretical estimations. The deviation associated with the measurements is due to the measurement uncertainty of the equipment (FTIR), based on the calibration curves for the ethanol-water system. The uncertainty associated with the measurements is in absolute terms, which is why it tends to be higher for the results at 22°C, as the ethanol concentrations in the gas phase are approximately half of those achieved at 34°C.

We emphasize that if there were any contribution from mechanical entrainment in the gas phase measurements, there would be a significant increase in ethanol concentration above the equilibrium values, which did not happen. The long extension of the gas outlet tubes from the reactor in the experimental setup, combined with the reduced diameter and the presence of many accidents in the gas collection pipelines, prevents mechanical entrainment droplets from entering the gas analysis chamber. As a result, the measurements are solely and exclusively representative of the thermodynamic entrainment effect. Values much below saturation would indicate that the bubbles did not reach saturation, which was also not the case. Moreover, the comparison between the results of the R8H and SSD sparger (Fig. 4.12 for 4.5 L), which generate fine and microbubbles, respectively, presented no difference regarding the ethanol concentration.

The results obtained showed that all the conditions of temperature, flow rate, and diameter of bubbles reached the thermodynamic equilibrium. This means a breakthrough regarding the understanding of the mechanical and thermodynamic entrainment in stripping operations, which will lead us to the possibility of distinguishing the effects of each phenomenon separately. Calling attention to the diameter of bubbles, different from the initial idea microbubbles turned out to have the same effectiveness as fine bubbles regarding thermodynamic entrainment.

4.4.4 Stripping Experiments

The stripping experiments were conducted in a 10 L reactor with varying operating volumes of hydroalcoholic solution (1.0, 4.5, and 8.0 L). The experiments spanned a duration of 4 h, and the outcomes are visually represented in the ensuing Figs. 4.13, 4.14, and 4.15 depicts the total ethanol removed for each experiment and the total specific selectivity, which regards the effect of thermodynamic and mechanical entrainments together.

Fig. 4.13 exhibits the specific selectivity and total moles of ethanol removed at different continuous gas flow rates in the reactor with an initial volume of 1.0 L of hydroalcoholic solution. As observed, there was a noteworthy 36% increase in the total moles of ethanol removed as the gas flow rate escalated from 3.0 to 10.0 L min^{-1}, a result that aligns with our prior expectations. Notably, the specific selectivity achieved using both spargers (R8H and SSD) declined from 6.0 to 4.0 with the elevation of the gas flow rate, which could be explained by the sharp ethanol depletion in the liquid phase. However, the specific selectivity was kept up above the value of unity, which means by the end of the process the gas phase was 4 times more concentrated than the proportion of ethanol/water in the initial liquid phase.

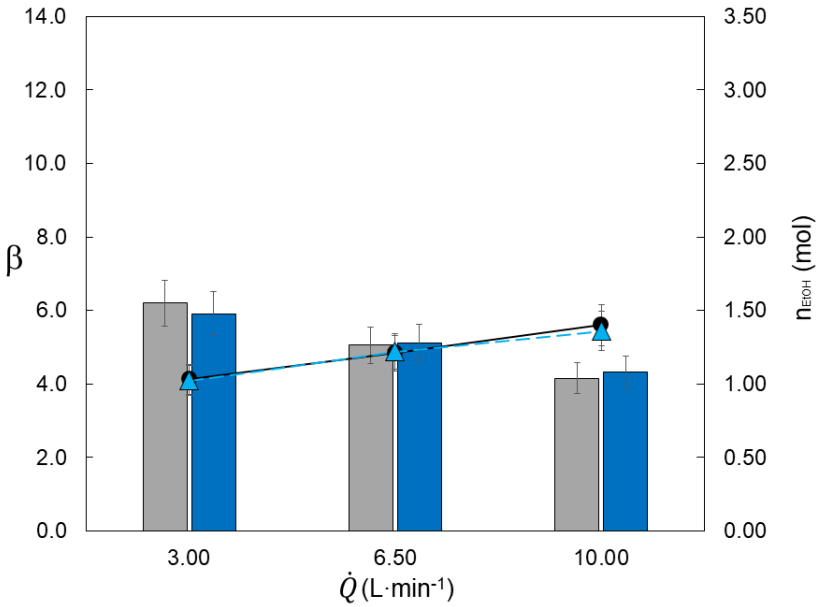

Figure 4.14. Specific selectivity (β) and total mols of ethanol were removed from the liquid phase after 4 hours of stripping carried out in 1.0 L of liquid volume. (■) Specific selectivity of the R8H sparger, (■) specific selectivity of the SSD sparger, (●) total ethanol removed using the R8H sparger, and (▲) total ethanol removed using the SSD sparger.

It is worth noticing that at first sight, the total number of mols of ethanol removed from the liquid phase is directly related to the gas flow rate, while the drop in ethanol concentration in the liquid phase depends on the specific gas flow rate. This statement would lead one to expect the same amount of ethanol removed for different initial volumes of liquids for the same gas flow rate, which did not occur, as seen in Fig. 4.14. Using the R8H sparger, there was an increase of 70% of

the total amount of removed ethanol by increasing the flow rate from 3.0 to 10.0 L min^{-1}, which corresponds to 110% more ethanol compared to the same gas flow rate (10 L min^{-1}) in the 1.0 L volume of operation. The same behavior was followed by the system using the SSD sparger.

Once the reactor used for operation with liquid volumes of 1.0, 4.5, and 8.0 L was the same, i.e., with the same cross-sectional area, the different volumes were achieved by increasing the liquid column height. The increase in the liquid height seems to have a noticeable effect on ethanol removal in the system, as can be observed by comparing Figs. 4.13 and 4.14. The effect of the depletion of ethanol in the liquid phase caused by the increase in the flow rate does not seem to have an impact as thought at first since the specific selectivity increased as the gas flow rate also increased, as shown in Fig. 4.14. The specific selectivity virtually doubled with the increase in the gas flow rate from 3.0 to 10.0 L min^{-1}, reaching the values of 11.5 and 9.3 for the R8H and SSD spargers, respectively. At this scale of liquid volume, it becomes evident a slight superiority of the R8H sparger regarding the ethanol removal at the gas flow rate of 10 L min^{-1} and the selectivity for all gas flow rates.

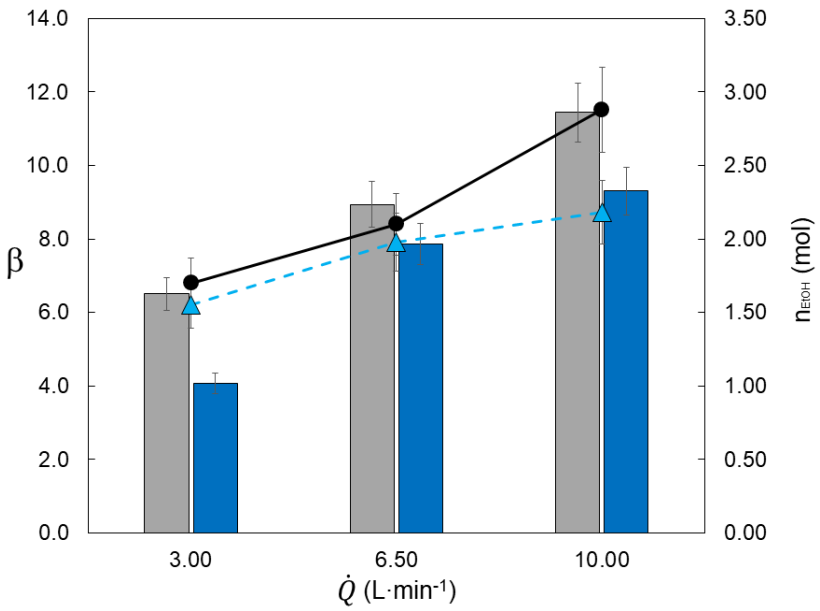

Figure 4.15. Specific selectivity (β) and total mols of ethanol removed from the liquid phase after 4 hours of stripping carried out in 4.5 L of liquid volume. (■) Specific selectivity of the R8H sparger, (■) specific selectivity of the SSD sparger, (●) total ethanol removed using the R8H sparger, and (▲) total ethanol removed using the SSD sparger.

As mentioned earlier, gas phase saturation is achieved under all operational conditions, and the thermodynamic entrainment becomes a function solely of the gas flow rate used for stripping and the ethanol concentration in the liquid phase. The latter is influenced by mechanical entrainment, which can be affected by the terminal velocity of bubbles, which, in turn, depends on the liquid height. It appears that the increase in the terminal velocity of bubbles with the increase in liquid height may have led to an increase in ethanol removal and specific selectivity of the system operated at 4.5 L. On the other hand, the results shown in Fig. 4.15 for the liquid volume of 8.0 L indicate a stabilization for the specific selectivity (approximately 8.0) and the total ethanol removed for all gas flow rates close to the ones reached in the 4.5 L of liquid. Also, a close behavior of the systems operated by the R8H and SSD spargers is noticed. These facts indicate there may be a minimum height of liquid for the system (reactor and sparger) which can maximize the ethanol selectivity and removal despite the drop in ethanol concentration in the liquid phase, which corresponds to the volume of liquid of 4.5L and flow rate of gas of 10 L min^{-1} ($\phi \approx 2.2$ vvm).

Those results contrast with those obtained by Calverley et al. (2020, 2021b), in which the authors observed greater ethanol removal for smaller liquid column heights. However, it should be noted that the system used by the authors is non-isothermal, meaning that the temperature of the microbubbles (120°C) is initially twice that of the liquid phase in the reactor (60°C). This leads to a transient energy state governing the phenomena occurring in the reported stripping operation. In the case of the current study, care was taken to maintain the gas and liquid temperatures very close and to establish a sufficiently high liquid column height to ensure that upon leaving the reactor, the gas phase has already reached a steady state in terms of temperature and concentration with the liquid phase. Thus, all the effects reported here that contribute to the increased concentration of ethanol in the gas phase are attributed to the presence of pure mechanical entrainment.

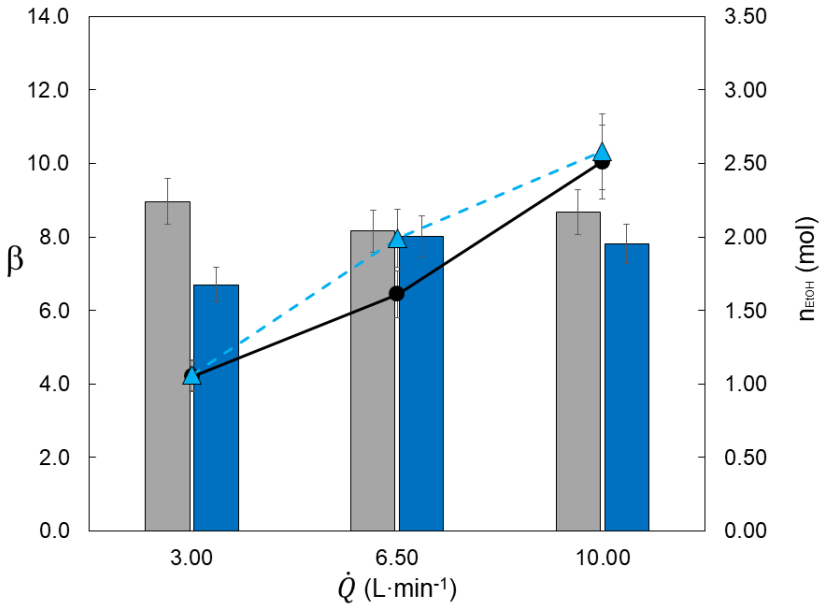

Figure 4.16. Specific selectivity (β) and total mols of ethanol removed from the liquid phase after 4 hours of stripping carried out in 8.0 L of liquid volume. (■) Specific selectivity of the R8H sparger, (■) specific selectivity of the SSD sparger, (●) total ethanol removed using the R8H sparger, and (▲) total ethanol removed using the SSD sparger.

Figs. 4.16 to 4.18 depict the effect of the mechanical and thermodynamic entrainments separately, for each volume of liquid operated. Fig. 4.16 regards the system of 1.0 L of liquid volume. The first important point highlighted by the results is that the specific thermodynamic selectivity is higher than the mechanical selectivity for virtually all operational conditions for both spargers. However, despite being lower than the thermodynamic selectivity, the mechanical selectivity still exceeds unity, indicating the scientific breakthrough achieved with these results. Unlike what has always been believed, the composition of the thermodynamic entrainment is not equal but rather at least 3 times higher than the composition of the liquid phase, considering the system with the lowest total specific selectivity (volume of 1.0 L). The second point is the similarity of results for both sprayers, R8H, and SSD, even though the SSD generates microbubbles at least tens of times smaller in diameter than the fine bubbles produced by the R8H sparger. This fact corroborates the previous findings of bubble saturation, indicating that at least thermodynamically, there is no difference between microbubbles or fine bubbles generated by porous and conventional spargers, respectively.

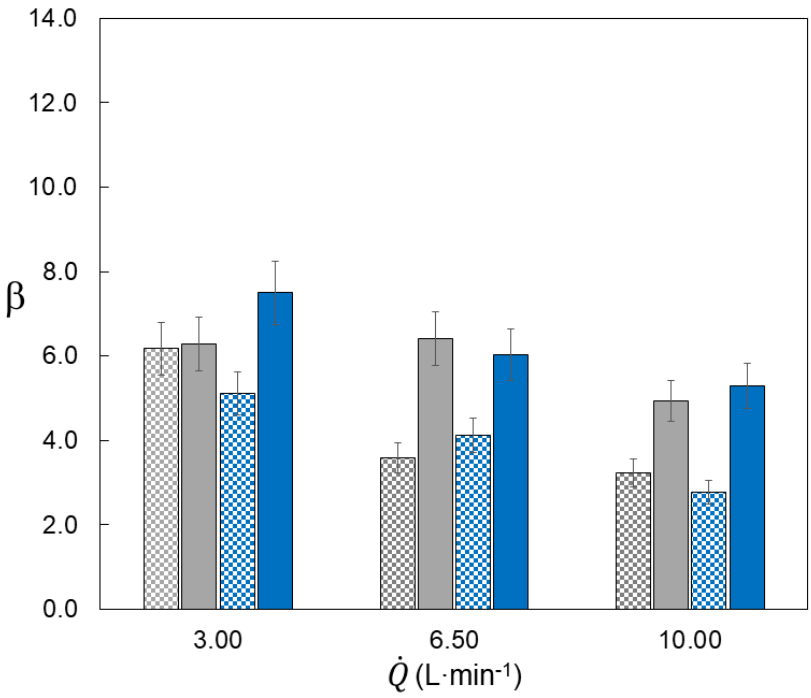

Figure 4.17. Specific selectivity (β) after 4 hours of stripping carried out in 1.0 L of liquid volume. (▩) Mechanical and (▬) thermodynamic specific selectivity for the R8H sparger, (▩) mechanical and (▬) thermodynamic specific selectivity for the SSD sparger.

The specific selectivity of the thermodynamic entrainment is essentially the same for both spargers (approximately 9.0) for all gas flow rates operated in the 4.5 and 8.0 L volumes, as shown in Figs. 4.17 and 4.18. However, it is noteworthy that the specific selectivity of the mechanical entrainment increases considerably at the 4.5 L volume when the gas flow rate is increased from 3.0 to 10 L min^{-1}. The increase in mechanical selectivity is reflected in the total selectivity increase for the 10 L min^{-1} condition, as shown earlier in Fig. 4.14. The concentration achieved by the mechanical entrainment under this operational condition was about 12 times higher than the composition of the liquid phase. This indicates that there is an effect of the liquid height on the increase in mechanical entrainment selectivity, which stabilizes after a certain value, as shown in Fig. 4.18. Furthermore, for the 8.0 L volume, the selectivity of the mechanical entrainment becomes lower than the thermodynamic entrainment selectivity again, for both spargers.

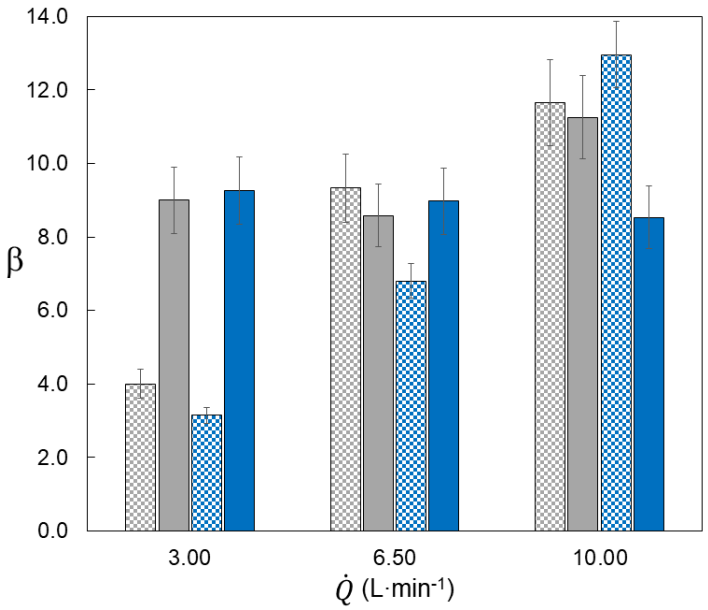

Figure 4.18. Specific selectivity (β) after 4 hours of stripping carried out in 4.5 L of liquid volume. (▩) Mechanical and (▩) thermodynamic specific selectivity for the R8H sparger, (▩) mechanical and (▩) thermodynamic specific selectivity for the SSD sparger.

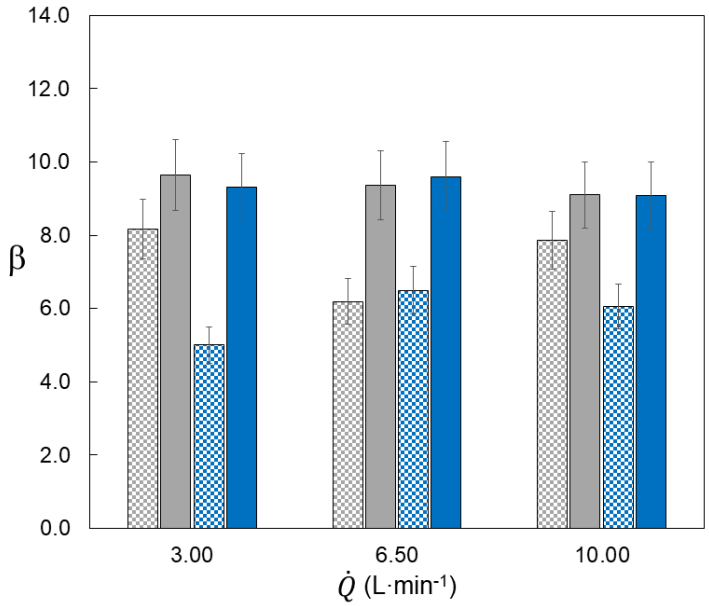

Figure 4.19. Specific selectivity (β) after 4 hours of stripping carried out in 8.0 L of liquid volume. (▩) Mechanical and (▩) thermodynamic specific selectivity for the R8H sparger, (▩) mechanical and (▩) thermodynamic specific selectivity for the SSD sparger.

Considering the total number of moles of ethanol carried over from the liquid phase, it was possible to determine the percentage of removal promoted by the thermodynamic and mechanical entrainments using the mathematical modeling proposed in the Materials and Methods section, as shown in Figs. 4.19 to 4.21. Upon analyzing the performance of the R8H sparger at a liquid volume of 1.0 L, as depicted in Fig. 4.19, the percentage of ethanol removed from the liquid phase due to the thermodynamic entrainment remained constant and approached 70% regardless of the gas flow rate employed. However, as the volume increased to 4.5 L, the percentage of ethanol removal by the thermodynamic entrainment equaled that of the mechanical entrainment at the 50% threshold, as illustrated in Fig. 4.20. This fact does not mean a shortcoming of the process, since the mechanical entrainment can also contribute to the ethanol concentration in the gas phase, as shown previously in Fig. 4.17 for 10.0 L min^{-1}. Notably, this plateau was sustained at a gas flow rate of 3.0 L min^{-1} when the operating volume escalated to 8.0 L. Nevertheless, the percentage of ethanol removed via the thermodynamic entrainment surged back to the 70% level when gas flow rates of 6.5 and 10 L min^{-1} were applied as shown in Fig. 4.21.

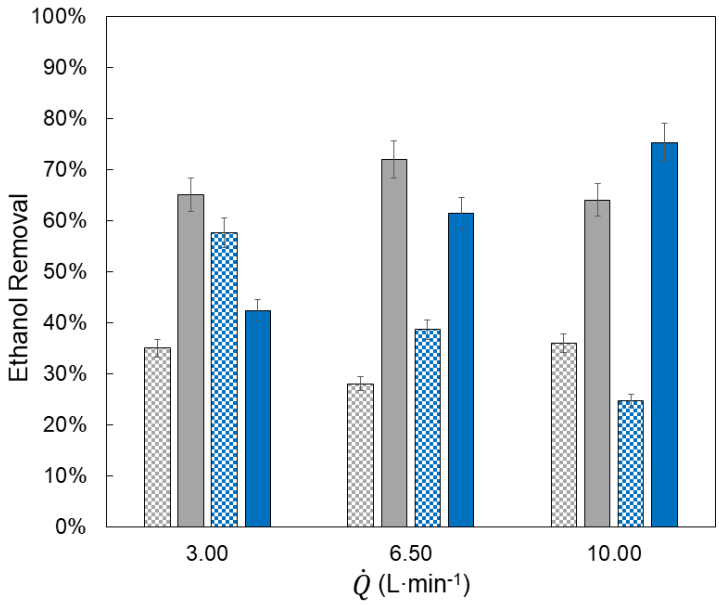

Figure 4.20. Percentage of ethanol removal in 1.0 L of liquid volume. (▩) Mechanical and (▭) thermodynamic percentage of removal using the R8H sparger, (▩) mechanical and (▭) thermodynamic percentage of removal using the SSD sparger.

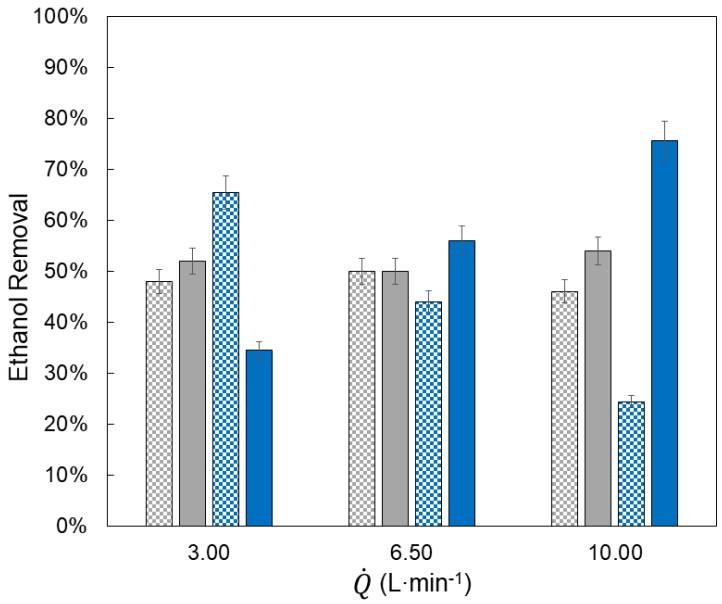

Figure 4.21. Percentage of ethanol removal in 4.5 L of liquid volume. (▩) Mechanical and (▭) thermodynamic percentage of removal using the R8H sparger, (▩) mechanical and (▬) thermodynamic percentage of removal using the SSD sparger.

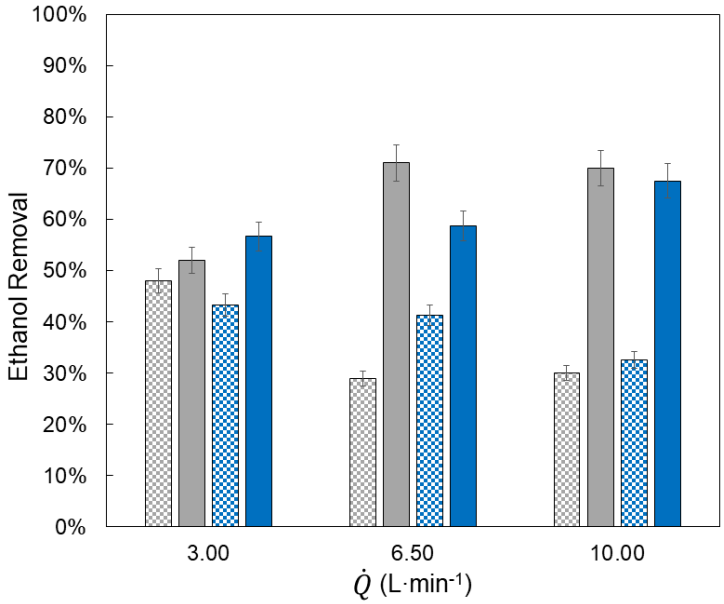

Figure 4.22. Percentage of ethanol removal in 8.0 L of liquid volume. (▩) Mechanical and (▭) thermodynamic percentage of removal using the R8H sparger, (▩) mechanical and (▬) thermodynamic percentage of removal using the SSD sparger.

However, the most intriguing finding from the analysis of ethanol removal percentages via mechanical and thermodynamic entrainment lies in the results obtained for the SSD sparger. Remarkably, across all liquid volume conditions (1.0, 4.5, and 8.0 L), there is a gradual increase in the percentage of removal via thermodynamic entrainment with the increase in gas flow rate. Although this increase is less pronounced at the largest volume (Fig. 4.21), it remains evident. This phenomenon can be attributed to the rise in gas retention resulting from the higher gas flow rates, particularly with the SSD sparger, which generates microbubbles, imparting a milky appearance to the dispersed phase due to their abundance. Microbubbles have a natural tendency to resist coalescence compared to fine bubbles, leading to an accumulation of microbubbles at the liquid surface, forming a thick foam. As the gas flow rate increases, so does the thickness of the foam, causing the portion of ethanol removed by mechanical entrainment to decrease in comparison to thermodynamic entrainment. It turns out the role of the foam be compared to the presence of a natural demister at the top of the reactor. The profile of the foam thickness increase can be observed in Fig. 4.22, where the reactor was operated at a volume of 8.0 L. This dynamic underscores the complex interplay between gas flow rate, foam generation, and the distribution of ethanol removal via mechanical and thermodynamic mechanisms in the SSD sparger.

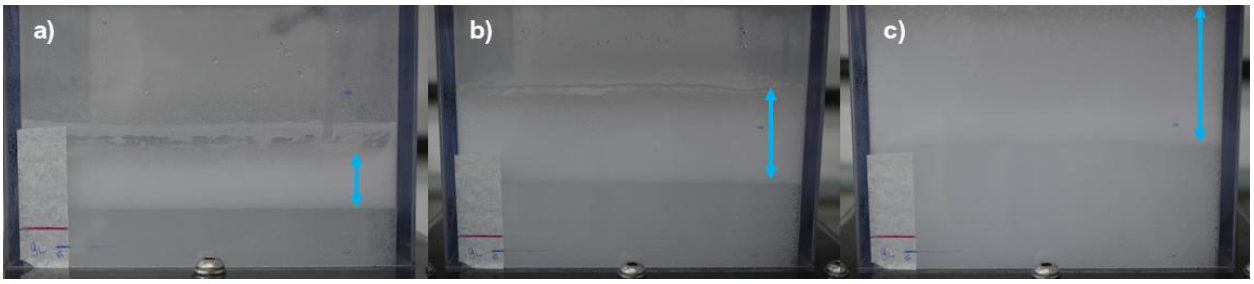

Figure 4.23. Profile of foam thickness for 8.0 L of hydroalcoholic solution volume under the gas flow rates conditions of (a) 3.0, (b) 6.5, and (c) 10 L min^{-1}.

Alongside the discovery that bubbles smaller than 5 mm in diameter leave the system fully saturated, the key finding from the ethanol stripping experiments was that mechanical entrainment in the gas phase is at least 3 times more concentrated in ethanol than in the liquid solution. This fact can be explained based on the analysis of the surface tension of water and ethanol. Sharma et al. (2019) investigated the surface tension of liquid mixtures containing ethanol and water at different ethanol concentrations. Pure ethanol has a surface tension of 21.6 mN m^{-1}, while pure

water has a surface tension of 72.8 mN m^{-1}. When the bubble exits the reactor, moments before its bursting, it carries water and ethanol molecules on its surface. Due to the tendency of ethanol to adhere more to any surface, including the liquid layer surrounding the bubble, there is a higher likelihood of entraining ethanol rather than water during bubble bursting. Hyde et al. (2019) previously combined neutron reflectivity (NR) experiments with molecular simulations, which supported the hypothesis that ethanol tends to be enriched at the water/air interface, with its concentration in the surface layer being significantly higher than in the bulk medium. The ethanol molecule combines a hydrophilic head with a nonpolar tail, making it weakly amphiphilic, as corroborated by analysis of the surface tensions of water and ethanol. The higher concentration of ethanol in their liquid film than water, leading to a significantly greater removal of ethanol compared to water at the moment of the bubble bursting.

The same previous analyses were performed for the stripping experiments carried out in a square-section reactor with a volume of 50.0 L. However, only two different gas flow rates were used to compare each of them under continuous and pulsed feeding conditions. As discussed earlier in Chapter 2, the newly developed system for generating pulsed gas flow requires that the higher the gas flow rate used, the higher the operating frequency of the valve should be. Consequently, the reactor was operated at a fixed volume of 50.0 L of hydroalcoholic solution, with gas flow rates of 20 and 40 L min^{-1} in continuous mode and at frequencies of 70 and 120 Hz, respectively. Unlike the previous comparisons made between the results obtained with microbubbles and fine bubbles generated by the R8H and SSD spargers, respectively, the experiments in the 50 L reactor were conducted using the same sparger, the PS3. The difference in the bubble diameters in each system was achieved by employing pulsed gas flow at each operational flow rate. The pre-processing images of the bubbles generated in each system can be observed in Fig. 4.23. It is evident that despite being smaller in diameter, the bubbles generated by the pulsed gas flow are still classified as fine bubbles (d_{32} > 1.00 mm).

The conditions depicted in Fig. 4.23 (a) and (b) refer to the continuous and pulsed gas flow rate of 20 L min^{-1}, respectively. The first condition generated a Sauter diameter (d_{32}) of 2.3 mm, while the bubbles generated by the pulsed condition at 70 Hz reached 1.3 mm. This means bubbles are 43% smaller using the system of pulsed gas flow compared to the continuous condition. For the condition of 40 L min^{-1} shown in Fig. 4.23 (c) and (d), the system operated under continuous and pulsed (120 Hz) gas flow rates generated bubbles of 2.5 and 1.6 mm of Sauter diameter,

respectively, which means a decrease of 34 % in size using the new system of pulsed gas flow. Moreover, while it was not possible to precisely determine the number of bubbles in the liquid phase, it is visually evident that the number of bubbles increases with the rising gas flow rate and the transition from continuous to pulsed flow rate.

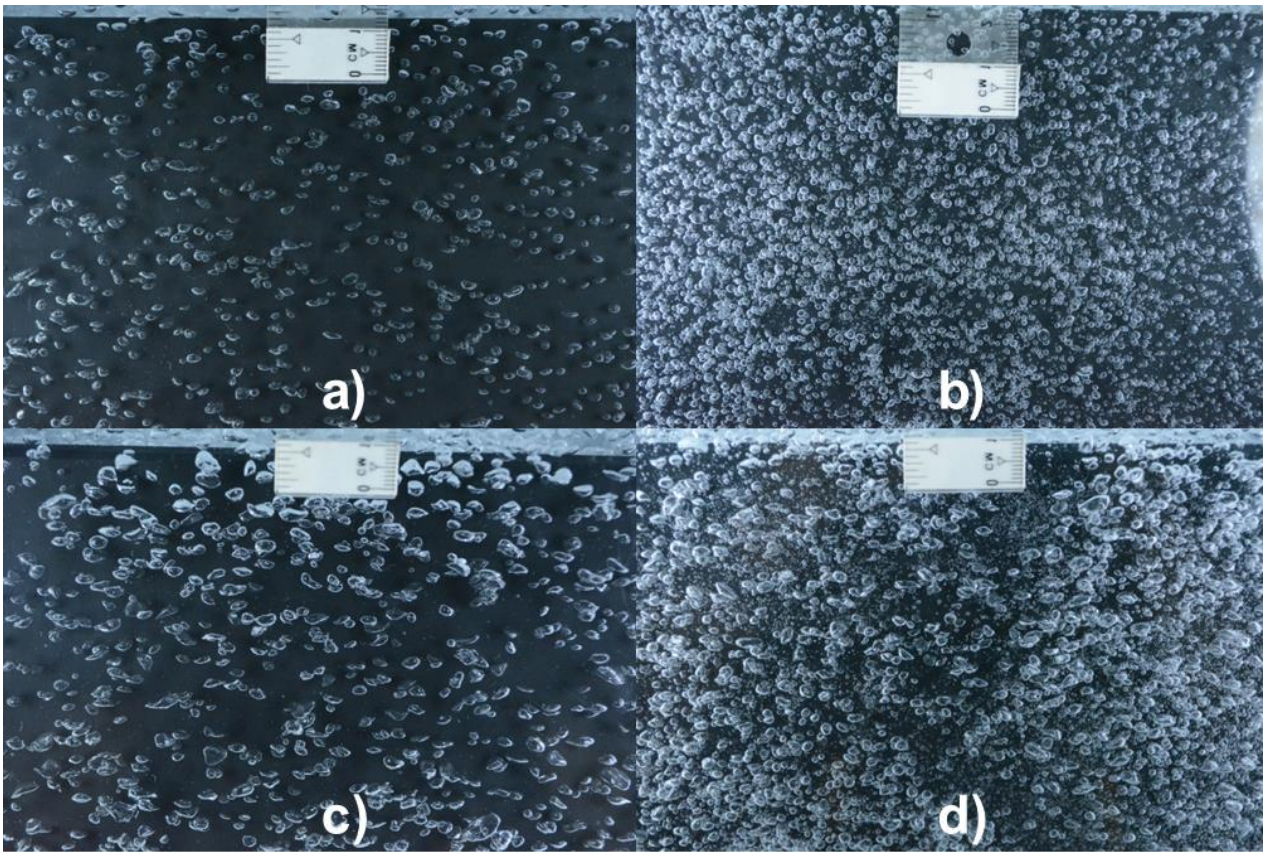

Figure 4.24. Bubbles profile in the 50 L hydroalcoholic solution under the condition of 20 L min^{-1} **(a)** continuous and **(b)** pulsed (70 Hz) and 40 L min^{-1} **(c)** continuous and **(d)** pulsed (120Hz) gas flow rates.

Fig. 4.24 presents the results of the total number of moles of ethanol removed and the overall specific selectivity for each of the aforementioned operational conditions for the 50 L reactor. There was no difference in either of the two parameters analyzed when comparing the two operating modes (continuous and pulsed gas flow). There was a tendency of increasing ethanol removal with the increase in gas flow rate, but a trend of diminishing overall specific selectivity. Comparing the results from the 50.0 L reactor with those obtained for gas flow rates of 3.0 and 6.5

L min^{-1} in the 8 L liquid volume reactor (maintaining the specific gas flow rate at 0.4 and 0.8 vvm in both reactors), it is observed that the increase in total ethanol removal scaled up by a factor of 6 times. However, the specific selectivity was approximately 50% and 25% higher in the 50.0 L reactor for gas flow rates of 20 and 40 L min^{-1}, respectively, compared to the 8.0 L reactor.

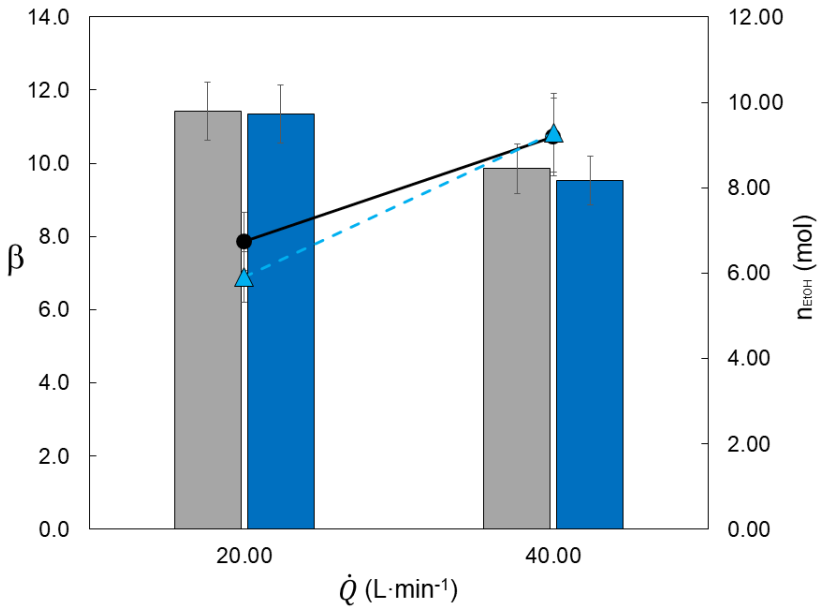

Figure 4.25. Specific selectivity (β) and total mols of ethanol removed from the liquid phase after 4 hours of stripping carried out in 50 L of liquid volume. (■) Specific selectivity under continuous and (■) pulsed (70 and 120 Hz) gas flow rates, (●) total ethanol removed using continuous, and (▲) pulsed (70 and 120 Hz) gas flow rates.

By evaluating the results of specific selectivity separately for mechanical and thermodynamic entrainment shown in Fig. 4.25, it can be observed for the condition of 0.4 vvm (20 L min^{-1}), the specific selectivity of mechanical entrainment was approximately 50% higher than that achieved by thermodynamic entrainment, and this was consistent for both spargers. Comparing this result with those obtained for the 8.0 L liquid volume system, the specific selectivity of mechanical entrainment in the 50.0 L system was approximately twice that achieved in the previous one. On the other hand, the specific selectivity of thermodynamic entrainment was approximately 10.0 for both operational scales, which demonstrates the robustness of the calculation methodology used to differentiate mechanical and thermodynamic entrainment. For the same specific gas flow rate, the thermodynamic entrainment should be equal for both

operational scales, and this fact was corroborated by the results obtained at the 50.0 L scale. The consistency of the thermodynamic entrainment selectivity across different reactor scales further supports the accuracy and reliability of the calculations employed in the study.

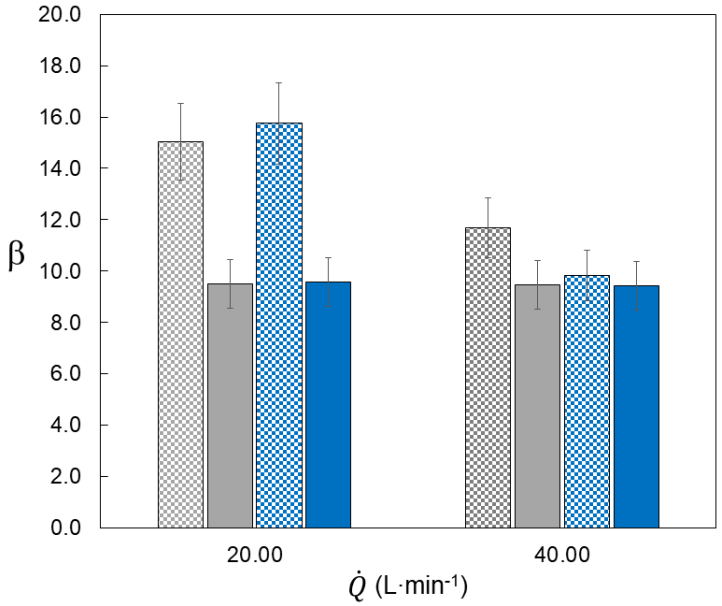

Figure 4.26. Specific selectivity (b) after 4 hours of stripping carried out in 50 L of liquid volume. (▨) Mechanical and (▭) thermodynamic specific selectivity for the continuous gas flow rates, (▨) mechanical and (▭) thermodynamic specific selectivity for the pulsed (70 and 120 Hz) gas flow rates.

The significant increase in the specific selectivity of mechanical entrainment in the 50.0 L system compared to the 8.0 L system highlights the potential advantages of scaling up the reactor for enhanced ethanol removal efficiency and indicates the selectivity of the ethanol removal is also related to the height of the liquid column and the gas flow rate together. Moreover, the reliable and consistent behavior of thermodynamic entrainment across different scales reinforces the validity of the methodology used to differentiate the two mechanisms of entrainment.

Fig. 4.26 presents the calculated results concerning the percentage of ethanol removed by mechanical and thermodynamic entrainment in the 50.0 L liquid volume reactor. The profiles are very similar to those observed at the 8.0 L scale, with the difference being a lower contribution of mechanical entrainment (20%) at the specific gas flow rate of 0.8 vvm. The difference in the contribution of mechanical entrainment between the two gas flow rates shown in Fig. 4.14 cannot

be attributed to the liquid height since both conditions were operated with 50.0 L of liquid volume. Nor did the bubble diameter make a difference, as the results of selectivity and ethanol entrainment were the same for continuous and pulsed gas flow (larger and smaller bubbles, respectively).

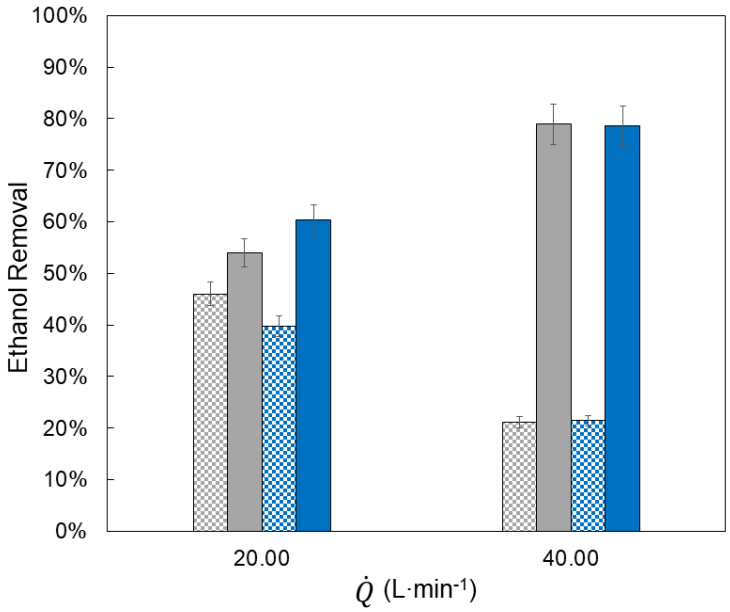

Figure 4.27. Percentage of ethanol removal in 50 L of liquid volume. (▩) Mechanical and (▭) thermodynamic percentage of removal using continuous gas flow rates, (▩) mechanical and (▭) thermodynamic percentage of removal using the pulsed (70 and 120 Hz) gas flow rates.

These results, therefore, indicate that the number of bubbles generated under different conditions may be the factor that impacts the higher or lower portion of mechanical entrainment when operating with fine bubbles. The findings highlight the importance of considering the bubble generation rate and the resulting bubble population in influencing the relative contribution of mechanical entrainment during the stripping process for this scale.

4.5 Conclusions

The results obtained from the stripping experiments brought to light discoveries regarding the ethanol removal process. The first one is the saturation of bubbles with water and ethanol, regardless of their diameter distribution. In the range from micrometers to 5.0 mm, bubbles were found to saturate under all operational conditions, confirming the results estimated by the equations and parameters proposed by Cussler (2009). Based on this crucial finding and the

methodology of simulating thermodynamic equilibrium during ethanol removal in small time intervals, it was possible to differentiate the mechanical and thermodynamic entrainment effects.

Equally significant is the revelation that contrary to our initial assumptions, mechanical entrainment can concentrate ethanol in the gas phase to even higher levels than thermodynamic entrainment. This concentration reached levels close to a factor of 15.0, expressed in terms of specific selectivity. Mechanical entrainment consistently demonstrated higher ethanol concentration than the composition of the liquid phase in all situations, which could be attributed to the lower surface tension that ethanol possesses compared to water. This property would enable ethanol to more effectively "wet" the liquid film surrounding the bubbles, resulting in more ethanol being expelled from the reactor during bubble bursting.

Mechanical entrainment was found to be dependent on different factors at various operational scales. There are indications that the liquid height influences the ethanol concentration in mechanical entrainment, as it is related to the terminal velocity of the bubbles. Consequently, the best result achieved for the reactor at the 4.5 L scale was at the highest gas flow rate operated (10.0 L min^{-1}) with the R8H sparger. However, when scaling up to 50.0 L, the best operational condition was achieved with the lowest gas flow rate (20 L min^{-1}), resulting in a specific selectivity from mechanical entrainment around 15.0. This indicates that the number of bubbles generated in the dispersed phase can also impact the specific selectivity of this phenomenon.

Microbubbles generated at scales of 1.0, 4.5, and 8.0 L performed very similarly to the fine bubbles generated with the R8H sparger, showing slightly lower specific selectivity in some operational conditions. Mechanical entrainment was not favored using microbubbles, especially at higher gas flow rates, due to the formation of a thick foam layer on the liquid surface of the reactor, acting as a natural demister.

In the case of the 50.0 L reactor, the use of pulsed gas flow did not yield significant changes in the overall ethanol removal or the selectivity of the stripping process. The results indicate that both continuous and pulsed gas-feeding strategies resulted in comparable ethanol removal efficiency and selectivity. Although the pulsatile flow technique showed promising results in producing smaller bubbles while maintaining fine bubble characteristics, its impact on the overall performance of the stripping process in the larger 50.0 L reactor seems negligible compared to continuous gas flow.

These findings shed light on the mechanisms that influence the preferential entrainment of ethanol over water in the stripping process, providing valuable insights into the understanding of the dynamics involved and the potential for enhancing the efficiency of ethanol removal in various industrial applications.

Chapter 5
Extractive Fermentations

5.1 Introduction

One of the key applications of the stripping process in the context of biofuels in the Brazilian scenario is within alcoholic fermentation for the production of fuel ethanol. In this context, several researchers have reported a significant increase in productivity when applying the stripping process during alcoholic fermentation (Rodrigues et al., 2018; Sonego et al., 2014, 2016). This increase is attributed to the reduction of the inhibitory effect caused by the presence of ethanol on the yeast. Such improvements hold promise, especially considering the anticipated need for industrial facilities expansion to meet the growing demand for low-carbon emission fuels.

This chapter presents the results of integrating the processes of ethanol production through gas-stripping extractive fermentation using the FBG (Fine Bubble Generator) system for generating fine bubbles and compares these results with conventional operation. The experiments were conducted in batch mode in bubble column reactors of 2.0, 10.0, and 50.0 L. The 2.0 L reactor was used as a control for conventional fermentation in duplicate and was carried out to obtain kinetic parameters for cell growth to be used in simulations of extractive fermentations. Subsequently, two batch extractive fermentations using commercial CO_2 were conducted in a 10 L reactor using the R8H sparger, with continuous gas flow rate and utilizing the pulsed flow system (FBG). The concentration of total reducing sugars in the substrate was 180 g L^{-1} in all conducted assays. This step was performed to verify the results obtained in Chapter 4 for different bubble diameters generated. A final experiment involving scale-up to a 50.0 L reactor was carried out under the same conditions as the 10.0 L reactor, utilizing only the fine bubble generation system using the PS3 sparger. The specific CO_2 flow rate used in all experiments, both pulsated and continuous, in the 10.0 L and 50.0 L reactors was 0.4 vvm, significantly below the values reported by Sonego et al. (2014, 2016).

5.2 Objective

To assess the impact of reducing bubble diameters in batch mode extractive fermentations within volumes of 10.0 and 50.0 L.

5.3 Materials and Methods

5.3.1 Conventional Batch Fermentation

A conventional batch fermentation ("CF") was conducted in a 2.0 L bubble column reactor to estimate kinetic parameters of cell growth for use in simulating extractive fermentations. Industrial lyophilized Saccharomyces cerevisiae (Y-904, AB Brasil Indústria e Comércio de Alimentos Ltda) was used in this study. The medium was prepared using analytical grade reagents and contained sources of carbon, nitrogen, phosphorus, potassium, and magnesium, simulating the composition of sugar cane molasses used in distilleries, and supplying the nutritional requirements of the yeast. To prepare the culture medium (1.4 L), the sucrose was dissolved together with the other reagents. The composition of the culture medium considering the 2.0 L volume was (g L^{-1}): sucrose (180.0), KH_2PO_4 (5.6), $MgSO_4.7H_2O$ (1.4), yeast extract (6.8), and urea (5.32). The initial pH of the fermentation broth was adjusted to 4.6 by adding hydrochloric acid (1 M).

Inoculation with lyophilized Saccharomyces cerevisiae employed an initial concentration of 19.95 g L^{-1} (dry basis) (0.6 L). At the beginning of all the cultivations, the agitation speed was maintained at 800 rpm using a magnetic agitator to ensure complete dissolution of the yeast flakes and promote mixing in the reaction medium. A commercial antifoaming agent (Serquímica SQ 2005) was added at the start of the process to prevent excessive foam formation. The yeast was allowed to acclimatize for 20 min prior to removal of the first sample. After the start of the fermentation process, an agitation speed of 250 rpm was maintained throughout the conventional batch fermentation. The temperature was maintained at 34 °C by circulating water from a thermostatic bath through the reactor jacket. Samples (30 mL volume) were withdrawn every hour for analysis of total reducing sugars, ethanol, and cell concentration. Samples at the beginning, middle and at the end of the experiment were taken to analyse the viability of the cells.

5.3.2 Analytical Methods

The cell concentration (on a dry mass basis) was determined after sample centrifugation at 8000 rpm and 4 °C for 10 min. The precipitate was washed twice with distilled water and then dried at 60 °C for 24 h. The concentrations of sucrose, glucose, fructose, and ethanol in the supernatant were determined using an HPLC (Waters, U.S.A.) equipped with a refractive index detector and a Sugar-Pak I column (300 × 6.5 mm, 10 μm, Waters) maintained at 80 °C. Ultrapure

water was utilized as eluent, at 0.5 mL min^{-1}. The standards were solutions of sucrose, glucose, fructose, and ethanol, at concentrations of between 0.1 and 8.0 g L^{-1}.

5.3.3 Batch Fermentation Mathematical Modeling

For the conventional batch fermentation, assuming that the generation of the product (ethanol) was associated to cell growth, the model used three differential equations representing the mass balances of cells (X), substrate (S), and ethanol (E) as shown in Eqs. (5.1) to (5.3).

$$\frac{dC_X}{dt} = \mu \cdot C_X \tag{5.1}$$

$$\frac{dC_S}{dt} = -\frac{1}{Y_{X/S}} \cdot \mu \cdot C_X \tag{5.2}$$

$$\frac{dC_E}{dt} = \frac{Y_{E/S}}{Y_{X/S}} \cdot \mu \cdot C_X \tag{5.3}$$

Where C_x is the cell concentration (g L^{-1}), μ is the specific cell growth rate (h^{-1}), C_S is the limiting substrate concentration (g L^{-1}), obtained from the sum of the concentrations of glucose and fructose), C_E is the ethanol concentration (g L^{-1}), $Y_{X/S}$ is the cell yield coefficient (g_X g_S $^{-1}$), and $Y_{E/S}$ is the ethanol yield coefficient (g_E g_S^{-1}).

The ethanol and cells coefficients can be calculated as shown in Eqs. (5.4) and (5.5).

$$Y_{X/S} = \frac{C_X \cdot V - C_{X0} \cdot V_0}{C_{S0} \cdot V_0 - C_S \cdot V} \tag{5.4}$$

$$Y_{P/S} = \frac{C_E \cdot V - C_{E0} \cdot V_0}{C_{S0} \cdot V_0 - C_S \cdot V} \tag{5.5}$$

Where the subscript “0” means the initial state.

The hybrid Andrews−Levenspiel kinetic model was used to represent the growth, considering inhibition by both substrate and product, shown in Eq. (5.6).

$$\mu = \mu_{max} \cdot \frac{C_S}{\left(K_S + C_S + \frac{C_S^2}{K_{IS}}\right)} \cdot \left(1 - \frac{C_E}{C_{E_{max}}}\right)^n \tag{5.6}$$

Where μ_{max} is the maximum specific cell growth rate (h^{-1}), K_S is the saturation constant (g L^{-1}), K_{IS} is the substrate inhibition constant (g L^{-1}), $C_{E_{max}}$ is the maximum concentration of ethanol after which cell growth ceased, and n is a dimensionless constant.

The kinetic parameters of Eq. (5.6) were estimated using the nonlinear regression method of Nelder and Mead, and the differential equation system was solved using the 4th Order Runge−Kutta algorithm. The minimization of the sum of squared residuals was the criteria to fit the parameters.

5.3.4 Extractive Batch Fermentation

The extractive fermentation experiments were conducted in 10.0 L and 50.0 L reactors. In the 10.0 L reactor, two experiments were performed: the first (EF1) with continuous flow rate of CO_2 gas (conventional extractive fermentation) and the second (EF2) with the Fine Bubble Generator (FBG) system operating at a frequency of 100 Hz and gas flow rate of 4.0 L min^{-1}. In the 50.0 L reactor, only the extractive fermentation experiment (EF3) with the FBG system operating at a frequency of 100 Hz and gas flow rate of 20 L min^{-1} was conducted.

The first 3 hours of the experiment were identical to the CF experiment. From the third hour onward, a specific gas flow rate of 0.4 vvm was initiated for the EF1, EF2, and EF3 experiments. Substrate and cell concentrations, as well as the experimental sampling procedures, were strictly the same as those carried out in the CF experiment. In the 10.0 L reactor, the substrate volume corresponded to 70% of the total volume (7.0 L), with the remaining volume filled with cell inoculum. For the 50.0 L reactor, the 70-30% proportion for the substrate and cell inoculum was maintained (35.0 L and 15.0 L, respectively).

5.3.5 Extractive Batch Fermentation Mathematical Modeling

The mathematical model of the extractive batch fermentation employed mass balance equations for cells (X), substrate (S), and ethanol (E), considering the removal of ethanol (E) and water (W) by the CO_2 stream, as well as changes in the broth volume (V). The mass balances for each of these components are depicted in Eqs. (5.7) to (5.10), which were solved using the 4th Order Runge-Kutta algorithm.

$$\frac{dC_X}{dt} = \mu \cdot C_X - C_X \cdot \frac{1}{V} \cdot \frac{dV}{dt} \tag{5.7}$$

$$\frac{dC_S}{dt} = -\frac{1}{Y_{X/S}} \mu \cdot C_X - C_S \cdot \frac{1}{V} \cdot \frac{dV}{dt} \tag{5.8}$$

$$\frac{dC_E}{dt} = \frac{Y_{E/S}}{Y_{X/S}} \mu \cdot C_X - C_E \cdot \frac{1}{V} \cdot \frac{dV}{dt} - k_E \cdot C_E \tag{5.9}$$

$$\frac{dV}{dt} = -\frac{\left(k_E \cdot C_E + k_W \cdot (\rho_W - C_E)\right) \cdot V}{\rho_W} \tag{5.10}$$

Where V is the broth volume (L), k_E is the removal rate constant for ethanol (h^{-1}), k_W is the removal rate constant for water (h^{-1}), and ρ_W is the specific mass of water (g L^{-1}).

5.4 Results

The system of differential equations was solved for the batch fermentation using the experimental data points for substrate, product, and cell concentrations. Table 5.1 presents the obtained results for the estimation of kinetic parameters of the fermentation. As can be observed, despite the cells and products yields, the other parameters differed from the ones obtained by Sonego et al. (2014). However, it is worth mentioning the yeasts cells were different than the one used by the authors in the other study. This fact could explain the differences in the kinetic parameters obtained.

Table 5.1. Estimated values of the kinetic parameters for the conventional process.

Parameter	Value
$Y_{X/S}$ ($g_X\ g_S^{-1}$)	0.04 ± 0.01
$Y_{E/S}$ ($g_E\ g_S^{-1}$)	0.465 ± 0.007
μ_{max} (h^{-1})	0.14 ± 0.05
K_S ($g\ L^{-1}$)	72.13 ± 3.86
K_{IS} ($g\ L^{-1}$)	119.17 ± 10.85
$C_{E_{max}}$ ($g\ L^{-1}$)	91.03 ± 1.88
n (-)	0.15 ± 0.02

Fig. 5.1 shows the results of C_E and C_S for the duplicate of experiments performed at the 2-L scale for the conventional fermentation. The average of the values were used to compared the conventional mode of operation with the other extractive fermentations regarding the productivity of ethanol. The standard deviation of the parameters was calculated using the duplicates of the experiments.

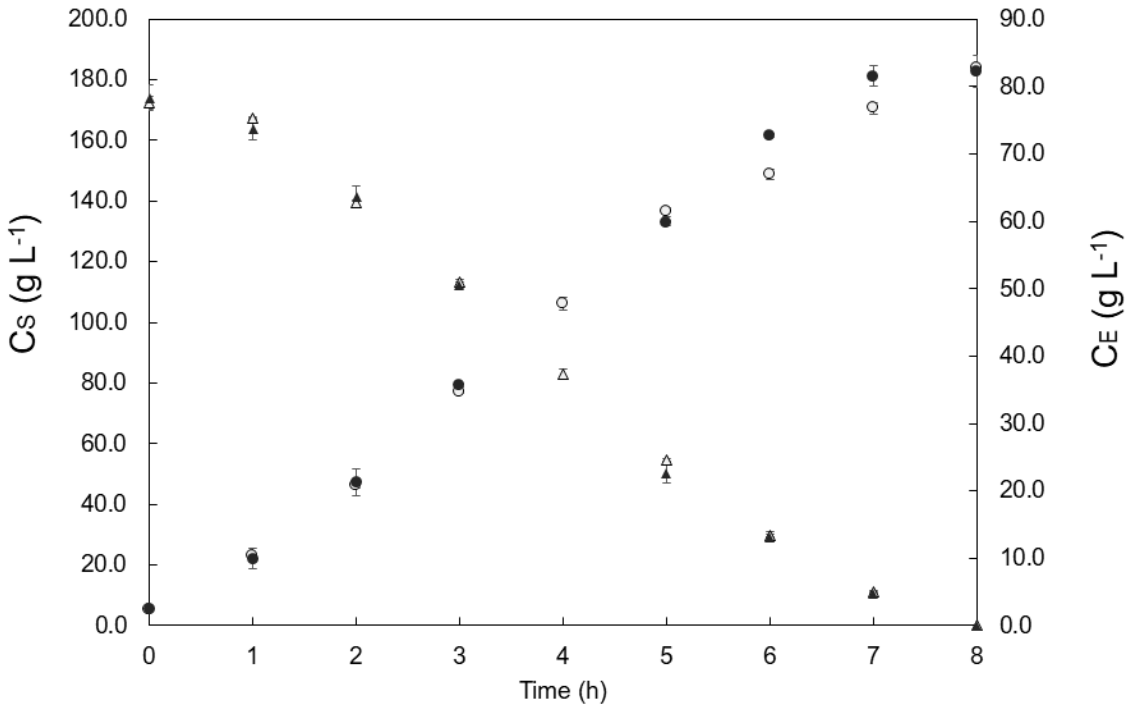

Figure 5.1. C_E and C_S profiles for the duplicate of conventional batch fermentation at 2-L scale. (▲) C_S and (●) C_E at CF (1), (△) C_S and (○) C_E at CF (2).

The obtained kinetic parameters, as well as the estimated substrate-to-product yield ($Y_{E/S}$) value from the conventional batch, were employed in the extractive fermentation model for the experiments conducted in 10.0 and 50.0 L reactors. The values of k_E and k_W were experimentally determined from previous hydroalcoholic stripping assays and are presented in Table 5.2.

Table 5.2. k_E and k_W value obtained for the same experimental conditions in stripping experiments using hydroalcoolic solutions.

Experiment	k_E (h^{-1})	k_W (h^{-1})
EF1	0.020 ± 0.002	0.0020 ± 0.0005
EF2	0.021 ± 0.002	0.0025 ± 0.0005
EF3	0.018 ± 0.001	0.0017 ± 0.0005

The simulations for the extractive fermentations in the 10.0 L reactors (EF1 and EF2) and the 50 L reactor (EF3) were conducted to determine the time at which substrate concentrations are

depleted and the final ethanol concentration in the solution. These calculations were based on the initial substrate concentration of each experiment and the $Y_{E/S}$ obtained from the conventional batch experiments. The experimental profiles of C_S and C_E for the CF, EF1 and EF2 experiments can be observed in Fig. 5.2.

It is worth noting that the final ethanol concentrations in the extractive fermentations were very similar to those obtained in the conventional batch fermentation. This similarity can be attributed to the low specific gas flow rate used in the EF1 and EF2 experiments. However, even with a specific gas flow rate of 0.4 vvm (Sonego et al. (2014) used 2.0 and 2.5 vvm), it is evident that substrate depletion occurred earlier in the pulsed gas flow extractive fermentation (EF2) than in the continuous gas flow system (EF1), with substrate exhaustion before the 7-hour mark in EF2. In contrast, the depletion in the conventional batch fermentation (CF) occurred at 8 hours. Those results seem to indicate a slightly advantage of using the pulsed gas flow, which generates bubbles around 40% smaller than the conventional ones. This eventual effect could be related to the surface tension of the liquid solution which directly impacts the mechanical entrainment caused by the bursting of bubbles. As was concluded in Chapter 4, the mechanical entrainment is responsible for the concentration of the liquid phase in the volatile component in the same level of the thermodynamical (vaporization) entrainment.

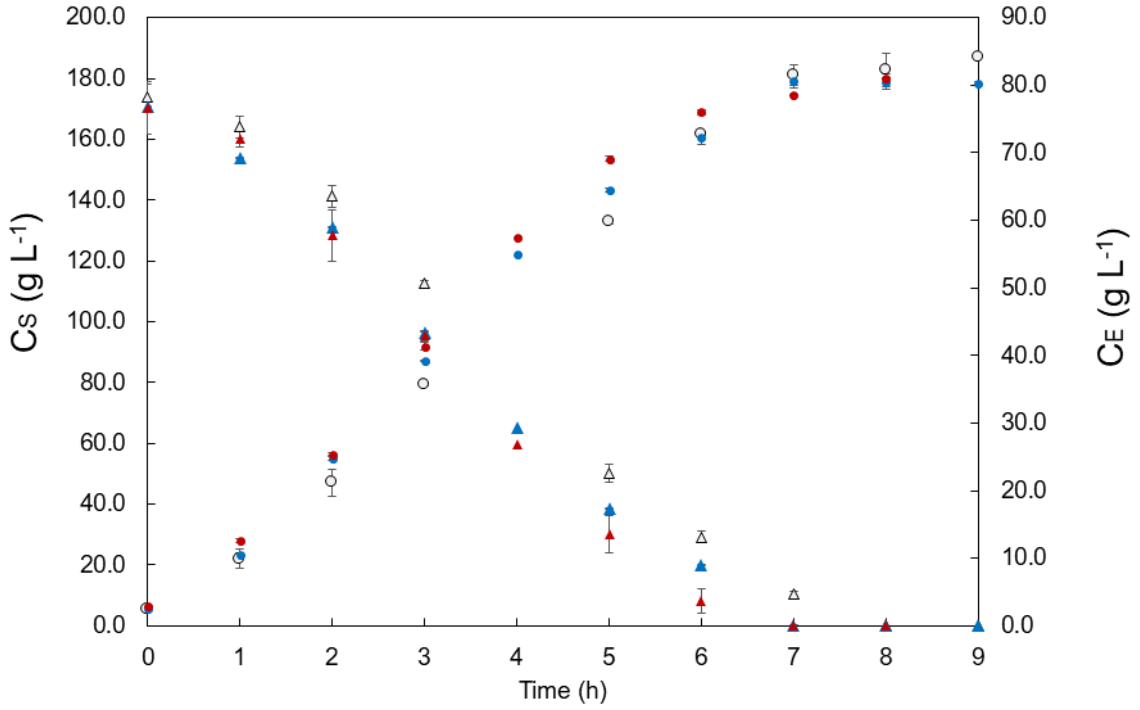

Figure 5.2. C_E and C_S profiles at reactors of 2.0 and 10.0 L. (△) C_S and (○) C_E at CF, (▲) C_S and (●) C_E at EF1, (▲) C_S and (●) C_E at EF2.

The final extractive fermentation experiment conducted was EF3, carried out in a 50 L reactor, utilizing pulsed gas flow generated by the FBG system. The outcomes were then compared with those obtained from the pulsed gas flow in the 10 L reactor (EF2). The findings are depicted in Figure 5.3. Although there is a slight difference in C_E and C_S between the two experiments at hours 5 and 6 of operation, it can be inferred that they fall within the range of experimental error. The concentration profiles between the two experiments are quite similar, indicating that the scale-up performed has proven to be satisfactory.

Table 5.3 depicts the results for each experiment and compare them in terms of maximum estimated ethanol concentration, $Y_{X/S}$ and most important the ethanol productivity, which can be obtained by the ratio of the estimated final C_E and the time for substrate depletion.

It is a fact that all three extractive fermentation experiments showed superiority when compared to the CF experiment in terms of volumetric productivity. However, among the EF experiments, it cannot be definitively stated that EF2 was superior to the others. The observed differences in substrate and ethanol concentrations, especially between the EF1 and EF2

experiments (as shown in Fig 5.2) at hours 5 and 6 of the experiment, could have been caused by analysis deviations, potentially amplified by the use of a low specific gas flow rate.

The achieved results were satisfactory comparing to the study carried out by Sonego et al. (2014) which reached an increase of 25% in ethanol productivity with a specific flow rate of 2.0 vvm. In our case, an increase of around 15% was reached using less than a quarter of the specific gas flow rate of the previous study.

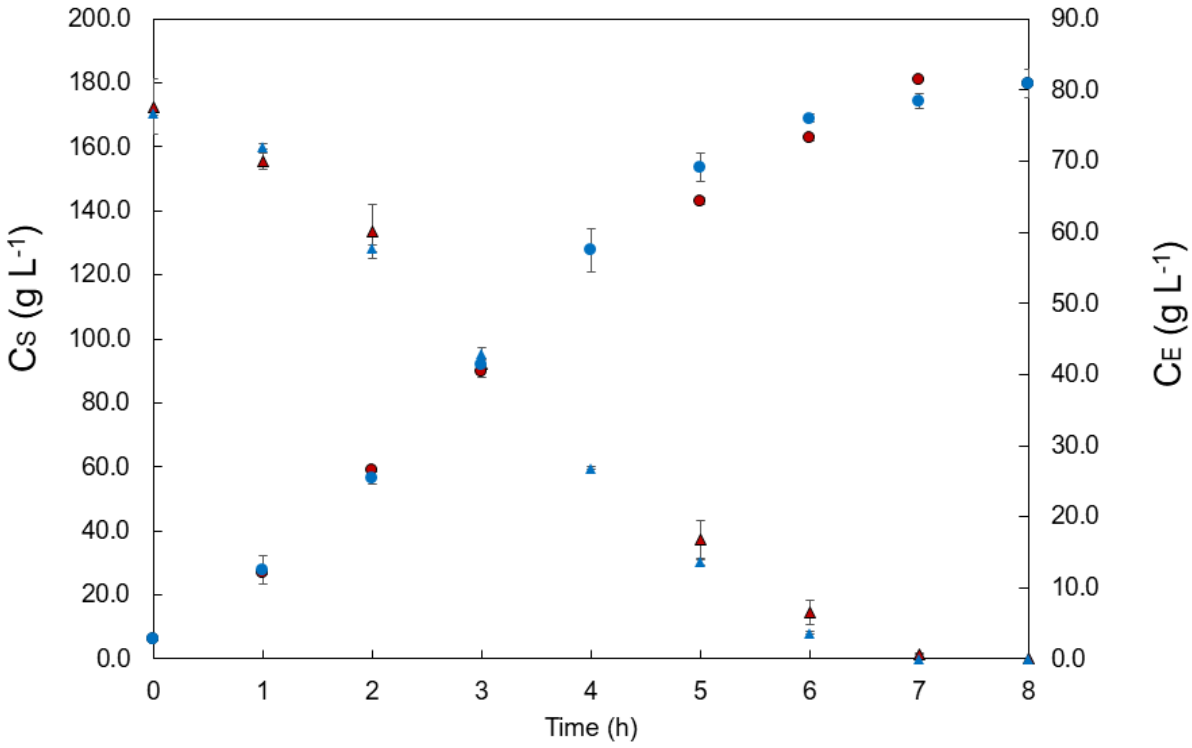

Figure 5.3. C_E and C_S profiles at reactors of 10.0 and 50.0 L. (▲) C_S and (●) C_E at EF2, (▲) C_S and (●) C_E at EF3.

Table 5.3. Performance parameters of operation for the conventional and extractive fermentations.

Variable	Units	CF	EF1	EF2	EF3
C_{S0}	(g L^{-1})	174.1	170.6	170.5	172.5
$Y_{X/S}$	(gx gs^{-1})	0.04	0.05	0.05	0.06
Estimated final C_E	(g L^{-1})	81.83	80.18	80.13	81.07
Time substrate depletion	(h)	8.0	7.0	6.5	6.9
Ethanol volumetric productivity	g L^{-1} h^{-1}	10.2	11.45	12.3	11.7

5.5 Conclusions

The strategy of extractive fermentation operation has proven to be a viable alternative for reducing yeast inhibition caused by the presence of ethanol, resulting in an increase in ethanol productivity. The obtained results from scaling up under the same operational conditions in this study (10.0 and 50.0 L) were satisfactory, as no significant difference in productivity was found among the different scales. Furthermore, another interesting yet anticipated outcome was the absence of significant productivity differences between using conventional bubbles and bubbles 40% smaller, generated by the FBG system. As observed in Chapter 4, variations of around 40% in the diameters of generated fine bubbles do not lead to significant differences in the removal of volatile compounds in stripping processes.

However, an increase of approximately 15% in ethanol productivity compared to the conventional system was achieved with a specific gas flow rate of 0.4 vvm. Previous studies achieved a 25% increase in productivity with a specific flow rate of 2.0 vvm, which is about five times higher. Proportionally, the process at 0.4 vvm proves advantageous, and this positive effect could be attributed to the diameter of the generated bubbles. Even without using pulsed flow, the sparger employed in the extractive fermentations of this study had more holes than those used in previous extractive fermentations. In other words, there might be an advantage in using spargers with more holes, considering the mechanical entrainment in the stripping process, even when operating with continuous gas flow rate.

Chapter 6

Final Considerations and Suggestions for Future Investigations

From the present results, it can be concluded that:

- The system for generating fine bubbles through pulsed gas flow, involving the use of pulsed gas flow generated by a high-frequency solenoid valve and commercial-sized perforated spargers, proved to be effective in generating smaller-sized bubbles. The system was tested at a pilot scale and resulted in a reduction of bubble diameters by approximately 40%;

- Porous spargers already generate fine bubbles on their own, and the use of pulsed gas flow doesn't always contribute to the reduction of the generated bubbles, as it needs to surpass their natural formation frequency;

- In addition to pulsed gas flow, other variables such as gas flow rate, orifice type, liquid medium composition, and sparger material also influence the premature detachment of bubbles and consequently the generation of smaller-sized bubbles;

- For oxygen transfer processes, a substantial improvement in the volumetric oxygen transfer coefficient was achieved through the use of the FBG system. Increases of around 50% were attained in the $k_L a$ value, indicating the potential applicability of the system in biological processes where oxygen or CO_2 transfer serves as a critical step in the process.

- For the stripping processes, it was observed that the bubbles become saturated very quickly, regardless of the operational volume in the reactor or the height of liquid and diameter of the generated bubbles, based on all the experimental cases tested. The bubbles exit saturated irrespective of their diameter because the saturation concentration of volatile compounds in the gas phase is relatively low, and the mass transfer coefficients are relatively high. Additionally, the mass of gas is much lower compared to the mass of liquid.

- The main outcome of the study was the successful modeling and quantification of the contributions of mechanical and thermodynamic entrainment in the ethanol and water stripping process. It was established that mechanical entrainment is also responsible for concentrating the entrained gas phase in terms of the most volatile solvent. This effect of

concentrating the removed phase can even surpass the influence of thermodynamic entrainment, contingent upon the operational conditions employed. Furthermore, the liquid height and terminal velocity of the bubbles appear to play a crucial role in the effects induced by mechanical entrainment.

- The extractive fermentations using pulsed and conventional gas flows did not exhibit any significant difference in terms of process performance parameters. However, the 15% increase in ethanol productivity compared to the conventional process using a specific gas flow rate of 0.4 vvm appears to be an attractive aspect of utilizing the system composed of pulsed gas flow and sparger.

Suggestions for further investigations:

- Studying hydrophilic materials and chemical treatments on conventional materials to enhance their hydrophilicity is an avenue worth exploring. Testing these various materials using the FBG system and analyzing the diameter of the generated bubbles could provide valuable insights.

- Understanding the relationship between mechanical entrainment and process variables such as liquid column height, surface tension of the liquid medium, and terminal velocity of the bubbles is crucial.

6.1 References

Abdulrazzaq, N., Al-Sabbagh, B., Rees, J. M., Zimmerman, W. B. (2016). Separation of azeotropic mixtures using air microbubbles generated by fluidic oscillation. *AIChE Journal*, *62*(4), 1192–1199.

Abdulrazzaq, N. N., Al-Sabbagh, B. H., Rees, J. M., Zimmerman, W. B. (2016). Purification of bioethanol using microbubbles generated by fluidic oscillation: A dynamical evaporation model. *Industrial & Engineering Chemistry Research*, *55*(50), 12909–12918.

Al Taweel, A. M. (2019). Sustainable reaction/separation engineering: A critical tool for the long-term wellbeing of the world. *Journal of King Saud University-Engineering Sciences, 31*(2), 105.

Al Taweel, A. M., Idhbeaa, A. O., Ghanem, A. (2013). Effect of electrolytes on interphase mass transfer in microbubble-sparged airlift reactors. *Chemical Engineering Science*, *100*, 474–485.

Al Taweel, A. M., Luo, J. J., Wang, J. (2003). Dynamic spargers: a novel approach to intensifying gas/liquid contacting operations. *Proceedings of the 5th International Process Intensification Conference*, 91–106.

Alkhalidi, A. A. T., Al Ba'ba'a, H. B., Amano, R. S. (2016). Wave generation in subsurface aeration system: a new approach to enhance mixing in aeration tank in wastewater treatment. *Desalination and Water Treatment*, *57*(56), 27144–27151.

Al-Mashhadani, M. K. H., Bandulasena, H. C. H., Zimmerman, W. B. (2012). CO_2 mass transfer induced through an airlift loop by a microbubble cloud generated by fluidic oscillation. *Industrial and Engineering Chemistry Research*, *51*(4), 1864–1877.

AL-Mashhadani, M. K. H., Wilkinson, S. J., Zimmerman, W. B. (2015). Airlift bioreactor for biological applications with microbubble mediated transport processes. *Chemical Engineering Science*, *137*, 243–253.

Almeida, L. P., Silva, C. R., Martins, T. B., Pereira, R. D., Esperança, M. N., Cruz, A. J. G., Badino, A. C. (2021). Heat transfer evaluation for conventional and extractive ethanol fermentations: Saving cooling water. *Journal of Cleaner Production*, *304*.

Al-yaqoobi, A., Hogg, D., & Zimmerman, W. B. (2016). Microbubble Distillation for Ethanol-Water Separation. *International Journal of Chemical Engineering, 2016*(1), 5210865.

Basha, O. M., Morsi, B. I. (2018). Novel approach and correlation for bubble size distribution in a slurry bubble column reactor operating in the churn–turbulent flow regime. *Industrial & Engineering Chemistry Research*, *57*(16), 5705–5716.

Bredwell, M. D., Worden, R. M. (1998). Mass-transfer properties of microbubbles. 1. Experimental studies. *Biotechnology Progress*, *14*(1), 31–38.

Brittle, S., Desai, P., Ng, W. C., Dunbar, A., Howell, R., Tesař, V., Zimmerman, W. B. (2015). Minimising microbubble size through oscillation frequency control. *Chemical Engineering Research and Design*, *104*, 357–366.

Calverley, J., Zimmerman, W. B., Leak, D. J., Bandulasena, H. C. H. (2020). Hot Microbubble Air Stripping of Dilute Ethanol-Water Mixtures. *Industrial and Engineering Chemistry Research*, *59*(43), 19392–19405.

Calverley, J., Zimmerman, W. B., Leak, D. J., Hemaka Bandulasena, H. C. (2021). Continuous removal of ethanol from dilute ethanol-water mixtures using hot microbubbles. *Chemical Engineering Journal*, *424*.

Cerri, M. O., Baldacin, J. C., Cruz, A. J. G., Hokka, C. O., Badino, A. C. (2010). Prediction of mean bubble size in pneumatic reactors. *Biochemical Engineering Journal*, *53*(1), 12–17.

Cerri, M. O., Nordi Esperança, M., Badino, A. C., Perencin de Arruda Ribeiro, M. (2016). A new approach for kLa determination by gassing-out method in pneumatic bioreactors. *Journal of Chemical Technology and Biotechnology*, *91*(12), 3061–3069.

Chen, Y., Ren, H., Liu, D., Zhao, T., Shi, X., Cheng, H., Zhao, N., Li, Z., Li, B., Niu, H. (2014). Enhancement of n-butanol production by in situ butanol removal using permeating–heating–gas stripping in acetone–butanol–ethanol fermentation. *Bioresource Technology*, *164*, 276–284.

Clift, R. (Roland), Grace, J. R., Weber, M. E. (1978). *Bubbles, drops, and particles*. Academic Press.

Cussler, E. L., (2009). *Diffusion: mass transfer in fluid systems*. Cambridge university press.

Daly, J. G., Patel, S. A., Bukur, D. B. (1992). Measurement of gas holdups and sauter mean bubble diameters in bubble column reactors by dynamics gas disengagement method. *Chemical Engineering Science*, *47*(13–14), 3647–3654.

Dani, A., Guiraud, P., Cockx, A. (2007). Local measurement of oxygen transfer around a single bubble by planar laser-induced fluorescence. *Chemical Engineering Science*, *62*(24), 7245–7252.

Das, A. K., Das, P. K., Saha, P. (2011). Formation of bubbles at submerged orifices–Experimental investigation and theoretical prediction. *Experimental Thermal and Fluid Science*, *35*(4), 618–627.

De Vrije, T., Budde, M., Van der Wal, H., Claassen, P. A. M., López-Contreras, A. M. (2013). “In situ” removal of isopropanol, butanol and ethanol from fermentation broth by gas stripping. *Bioresource Technology*, *137*, 153–159.

Desai, P. D., Hines, M. J., Riaz, Y., Zimmerman, W. B. (2018). Resonant pulsing frequency effect for much smaller bubble formation with fluidic oscillation. *Energies*, *11*(10), 2680.

Desai, P. D., Turley, M., Robinson, R., Zimmerman, W. B. (2021). Hot microbubble injection in thin liquid film layers for ammonia separation from ammonia rich-wastewater. *Chemical Engineering and Processing - Process Intensification*.

De Santana, E. M. (1994). Transferência de calor e massa em processos de borbulhamento (Doctoral dissertation, Unicamp).

Ezeji, T. C., Karcher, P. M., Qureshi, N., Blaschek, H. P. (2005). Improving performance of a gas stripping-based recovery system to remove butanol from Clostridium beijerinckii fermentation. *Bioprocess and Biosystems Engineering*, *27*(3), 207–214.

Ghanami, S., Farhadi, M. (2019). Fluidic Oscillators' Applications, Structures and Mechanisms–A Review. *Transp Phenom Nano Micro Scales*, *7*(1), 9–27.

Griffith, P., Wallis, G. B. (1961). Two-phase slug flow. *Journal of Heat Transfer*, *83*(3).

Hafeez, A., Shamair, Z., Shezad, N., Javed, F., Fazal, T., ur Rehman, S., Bazmi, A. A., Rehman, F. (2020). Solar Powered Decentralized Water Systems: A Cleaner Solution of the Industrial Wastewater Treatment and Clean Drinking Water Supply Challenges. *Journal of Cleaner Production*, 125717.

Hamer, G. (1965). Stripping in sparged fermentation systems. I. Two component model systems. *Biotechnology and Bioengineering*, *7*(2), 199–214.

Hanotu, J., Bandulasena, H. C. H., Chiu, T. Y., Zimmerman, W. B. (2013). Oil emulsion separation with fluidic oscillator generated microbubbles. *International Journal of Multiphase Flow*, *56*, 119–125.

Hanotu, J., Bandulasena, H. C. H., Zimmerman, W. B. (2012). Microflotation performance for algal separation. *Biotechnology and Bioengineering*, *109*(7), 1663–1673.

Hanotu, J., Kong, D., Zimmerman, W. B. (2016). Intensification of yeast production with microbubbles. *Food and Bioproducts Processing*, *100*, 424–431.

Hanotu, J. O., Bandulasena, H., Zimmerman, W. B. (2017). Aerator design for microbubble generation. *Chemical Engineering Research and Design*, *123*, 367–376.

Herrmann-Heber, R., Reinecke, S. F., Hampel, U. (2019). Dynamic aeration for improved oxygen mass transfer in the wastewater treatment process. *Chemical Engineering Journal*, 122068.

Hyde, A. E., Ohshio, M., Nguyen, C. V., Yusa, S. I., Yamada, N. L., and Phan, C. M. (2019). Surface properties of the ethanol/water mixture: Thickness and composition. *Journal of Molecular Liquids*, 290, 111005.

Karamanev, D. G. (1996). Equations for calculation of the terminal velocity and drag coefficient of solid spheres and gas bubbles. *Chemical Engineering Communications*, *147*(1), 75–84.

Kujawska, A., Kujawski, J., Bryjak, M., Kujawski, W. (2015). ABE fermentation products recovery methods—a review. *Renewable and Sustainable Energy Reviews*, *48*, 648–661.

Leng, R., Mazzanti, G., Idhbeaa, A. O., Al Taweel, A. M., Ghanem, A., Donaldson, A., Haelssig, J. (2022). An Enhanced Dgd Approach for Estimating Bubble Size Distributions in Microbubble-Aerated Contaminated Systems. *15th International Conference on Gas-Liquid Gas-Liquid-Solid Reactor Engineering GLS 2022*.

Mahmood, K. H. A. L., Wilkinson, S. J., Zimmerman, W. B. (2015). Airlift bioreactor for biological applications with microbubble mediated transport processes. *Chemical Engineering Science*, *137*, 243–253.

Martins, T. B., Almeida, L. P., Cerri, M. O., Badino, A. C. (2020). Mass Transfer Performance of Ethanol Removal by CO2 Stripping in Different Pneumatic Bioreactors. *Industrial Biotechnology*, *16*(2), 81–90.

Mohagheghian, S., Ghajar, A. J., Elbing, B. R. (2020). Effect of vertical vibration on the mixing time of a passive scalar in a sparged bubble column reactor. *Fluids*, *5*(1).

Mohseni, E., Herrmann-Heber, R., Reinecke, S. F., Hampel, U. (2019). Bubble generation by micro-orifices with application on activated sludge wastewater treatment. *Chemical Engineering and Processing-Process Intensification*, 107511.

Pallapothu, S. K., Al Taweel, A. M. (2012). Effect of contaminants on the gas holdup and mixing in internal airlift reactors equipped with microbubble generator. *International Journal of Chemical Engineering*, *2012*.

Panitz, T., Wasan, D. T. (1972). Flow attachment to solid surfaces: the Coanda effect. *AIChE Journal*, *18*(1), 51–57.

Park, S. H., Park, C., Lee, J. Y., Lee, B. (2017). A Simple Parameterization for the Rising Velocity of Bubbles in a Liquid Pool. *Nuclear Engineering and Technology*, *49*(4), 692–699.

Parmar, R., Majumder, S. K. (2013). Microbubble generation and microbubble-aided transport process intensification—A state-of-the-art report. *Chemical Engineering and Processing: Process Intensification*, *64*, 79–97.

Patel, S. A., Daly, J. G., Bukur, D. B. (1989). Holdup and interfacial area measurements using dynamic gas disengagement. *AIChE Journal*, *35*(6), 931–942.

Ponce, G. H. S. F., Moreira Neto, J., De Jesus, S. S., Miranda, J. C. de C., Maciel Filho, R., de Andrade, R. R., Wolf Maciel, M. R. (2016). Sugarcane molasses fermentation with in situ gas stripping using low and moderate sugar concentrations for ethanol production: Experimental data and modeling. *Biochemical Engineering Journal*, *110*, 152–161.

Ranz, W. E., Marshall, W. R. (1952). Evaporation from drops. *Chem. Eng. Prog*, *48*(3), 141–146.

Rees-Zimmerman, C. R., Chaffin, S. T. (2021). Modelling the effect of bioreactor height on stripping fermentation products from the engineered bacterium Geobacillus thermoglucosidasius. *Biochemical Engineering Journal*, *176*.

Rodrigues, K. C. S., Sonego, J. L. S., Cruz, A. J. G., Bernardo, A., Badino, A. C. (2018). Modeling and simulation of continuous extractive fermentation with CO_2 stripping for bioethanol production. *Chemical Engineering Research and Design*, *132*, 77–88.

Santos, M. V., Rodrigues, K. C. S., Veloso, I. I. K., Badino, A. C., Cruz, A. J. G. (2022). Real-time monitoring of ethanol fermentation using mid-infrared spectroscopy analysis of the gas phase. *Industrial & Engineering Chemistry Research*, 61 7225–7234.

Schumpe, A., Grund, Gjtcj. (1986). The gas disengagement technique for studying gas holdup structure in bubble columns. *The Canadian Journal of Chemical Engineering*, *64*(6), 891–896.

Seidel, S., Maschke, R. W., Werner, S., Jossen, V., Eibl, D. (2020). Oxygen mass transfer in biopharmaceutical processes: numerical and experimental approaches. *Chemie Ingenieur Technik*.

Sharma, M., Roy, P. K., Barman, J., Khare, K. (2019). Mobility of Aqueous and Binary Mixture Drops on Lubricating Fluid-Coated Slippery Surfaces. *Langmuir*, *35*(24), 7672–7679.

Sonego, J. L. S., Lemos, D. A., Pinto, C. E. M., Cruz, A. J. G., Badino, A. C. (2016). Extractive Fed-Batch Ethanol Fermentation with CO2 Stripping in a Bubble Column Bioreactor: Experiment and Modeling. *Energy and Fuels*, *30*(1), 748–757.

Sonego, J. L. S., Lemos, D. A., Rodriguez, G. Y., Cruz, A. J. G., Badino, A. C. (2014). Extractive Batch Fermentation with CO 2 Stripping for Ethanol Production in a Bubble Column Bioreactor: Experimental and Modeling. *Energy & Fuels*, *28*(12), 7552–7559.

Song, A., Ji, Y., Li, C., Cao, Y. (2021). Modeling and validation of the momentum force for bubble formation from submerged orifices with an oscillatory air supply. *Chemical Engineering Science*, 116387.

Sriram, K., & Mann, R. (1977). Dynamic gas disengagement: A new technique for assessing the behaviour of bubble columns. *Chemical Engineering Science, 32*(6), 571-580.

Tanaka, S., Kastens, S., Fujioka, S., Schlüter, M., Terasaka, K. (2019). Mass transfer from freely rising microbubbles in aqueous solutions of surfactant or salt. *Chemical Engineering Journal*.

Terasaka, K., Hirabayashi, A., Nishino, T., Fujioka, S., Kobayashi, D. (2011). Development of microbubble aerator for wastewater treatment using aerobic activated sludge. *Chemical Engineering Science*, *66*(14), 3172–3179.

Tesař, V. (2014). Mechanisms of fluidic microbubble generation Part II: Suppressing the conjunctions. *Chemical Engineering Science*, *116*, 849–856.

Tesař, V. (2017). What can be done with microbubbles generated by a fluidic oscillator? (survey). *EPJ Web of Conferences*, *143*, 02129.

Tesař, V., Hung, C. H., Zimmerman, W. B. (2006). No-moving-part hybrid-synthetic jet actuator. *Sensors and Actuators, A: Physical*, *125*(2), 159–169.

Treybal, R. E. (1980). Mass transfer operations. *New York*, *466*, 493–497.

Truong, K. N., Blackburn, J. W. (1984). The stripping of organic chemicals in biological treatment processes. *Environmental Progress*, *3*(3), 143–152.

Veloso, I. I. K., Rodrigues, K. C. S., Sonego, J. L. S., Cruz, A. J. G., Badino, A. C. (2019). Fed-batch ethanol fermentation at low temperature as a way to obtain highly concentrated alcoholic wines: Modeling and optimization. *Biochemical Engineering Journal*, *141*, 60–70.

Worden, R. M., Bredwell, M. D. (1998). Mass-transfer properties of microbubbles. 2. Analysis using a dynamic model. *Biotechnology Progress*, *14*(1), 39–46.

Xing, W., Yin, M., Lv, Q., Hu, Y., Liu, C., Zhang, J. (2014). Oxygen Solubility, Diffusion Coefficient, and Solution Viscosity. In *Rotating Electrode Methods and Oxygen Reduction Electrocatalysts* (pp. 1–31). Elsevier B.V.

Zimmerman, W. B., Hewakandamby, B. N., Tesař, V., Bandulasena, H. C. H., Omotowa, O. A. (2009). On the design and simulation of an airlift loop bioreactor with microbubble generation by fluidic oscillation. *Food and Bioproducts Processing*, *87*(3), 215–227.

Zimmerman, W. B., Tesař, V., Bandulasena, H. C. H. (2009). Efficiency of an aerator driven by fluidic oscillation. Part 1: Laboratory bench scale studies. *Sheffield University*.

Zimmerman, W. B., Tesar, V., Butler, S., Bandulasena, H. C. H. (2008). Microbubble generation. *Recent Patents on Engineering*, *2*(1), 1–8.

Zimmerman, W. B., Tesař, V., Hemaka Bandulasena, H. C. (2009). Efficiency of an aerator driven by fluidic oscillation. Part I: Laboratory bench scale studies. *1988*, 1–27.

Zimmerman, W. B., Zandi, M., Bandulasena, H. C. H., Tesař, V., Gilmour, D. J., Ying, K. (2011). Design of an airlift loop bioreactor and pilot scales studies with fluidic oscillator induced microbubbles for growth of a microalgae Dunaliella salina. *Applied Energy*, *88*(10), 3357–3369.

Zimmerman, W. B., Zandi, M., Hemaka Bandulasena, H. C., Tesař, V., James Gilmour, D., Ying, K. (2011). Design of an airlift loop bioreactor and pilot scales studies with fluidic oscillator induced microbubbles for growth of a microalgae Dunaliella salina. *Applied Energy*, *88*(10),